Aus dem Max-Planck-Institut für Kolloid- und Grenzflächenforschung

Doppelthydrophile Blockcopolymere als Mineralisationstemplate

Dissertation

Zur Erlangung des akademischen Grades
Doktor der Naturwissenschaften
-Dr. rer. nat.-
in der Wissenschaftsdisziplin Physikalische Chemie

eingereicht an der Mathematisch-Naturwissenschaftlichen Fakultät
der Universität Potsdam

von
Pavla Kašparová
aus Pardubice, Tschechische Republik

Golm, im April 2002

Table of contents

1   Preface

Natural shows extensive examples of specialized inorganic materials. Oyster shells, corals, ivory, sea urchin spines, cuttlefish bone, limpet teeth and magnetic crystals in bacteria are just a few of the vast variety of biological minerals engineered by living creatures (for example see Figure 1-1, Figure 1-2). Many of these biological building materials consist of inorganic minerals intricately combined with organic polymers. Together, these materials are fashioned into a fascinating variety of shapes and forms that serve many different functions. Not only biominerals are highly refined but also the extent of their production is enormous. For example, geological deposits such as the white cliffs in Dover (UK) contain billions of exquisite $CaCO_3$ scales formed within the cells of marine algae. Similarly, large-scale geographic features such as coral reefs are the result of immense biological activity [1].
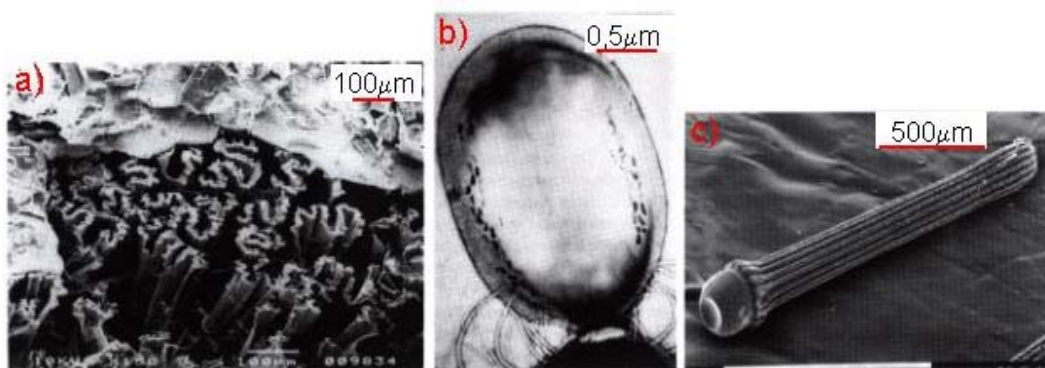
Figure 1-1: a) Scanning electron micrograph of a fractured section of a cuttlefish bone. The cuttlebone is a modified shell that is used as a buoyancy device. It is constructed of calcium carbonate (aragonite) and the polysaccharide, β-chitin. **b)** Transmission electron micrograph of a magnetotactic bacterial cell containing chains of bullet-shaped magnetite (Fe_3O_4) crystals. **c)** Single crystal of biogenic calcite $CaCO_3$. The crystal constitutes a single sea urchin spine [1].

Biomineralization, the controlled formation of inorganic minerals in organisms results in crystalline or amorphous materials of exquisite form, symmetry and ultra structure. Because these bioinorganic solids are precisely replicated throughout evolution, they have already for a long time been the subject of extensive investigations in the fields of biological systematic and paleontology. In contrast, the chemical and biology of biomineralization have only recently been studied in detail.

These studies are leading to new insights in bioinorganic chemistry and are providing novel concepts in crystal engineering and materials science [2].
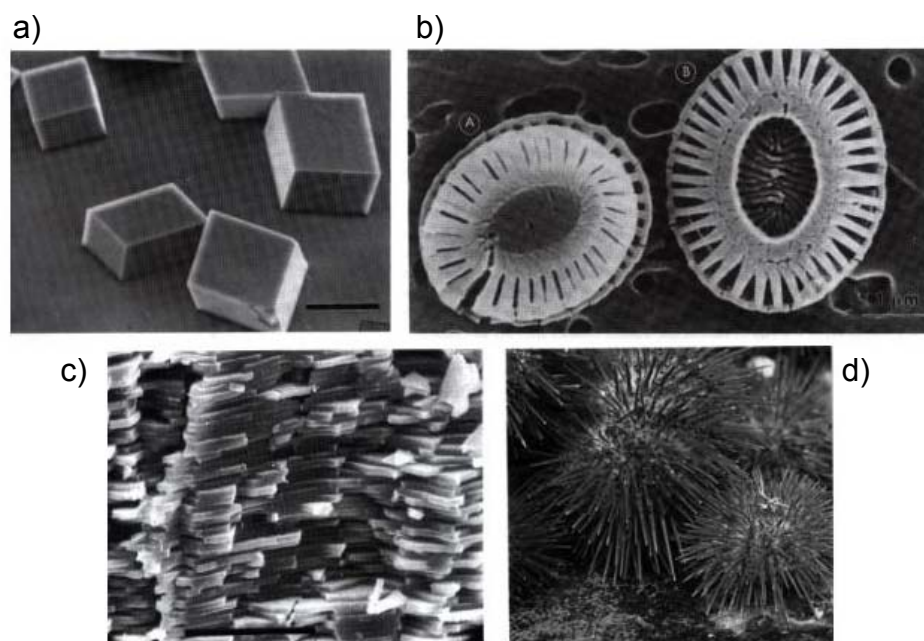
Figure 1-2: Various morphologies and crystal modification of calcium carbonate as synthetic crystal and biomineral **a)** Synthetic calcite [8], **b)** Cocolith (calcite) [8], **c)** mollusc shell (aragonite) [1], **d)** Ascidians (spicules are made from vaterite) [3].

Chemists are interested in the way biominerals are made because the ability to produce well-defined inorganic materials is of great value in fields such as modern materials, catalyses, medicine, electronics, magnetism, pigments, cosmetics and ceramics. For material scientists, biomineralization provides a unique opportunity to study solutions to key problems in materials design. The equilibrium form of crystals can be modified by surface-active additives, but only within limits dictated by the symmetry of the unit cell. In contrast, biological minerals, such as shells, bones and teeth are distinguished by a complexity of form that bears little resemblance to the underlying order of their inorganic crystals. By understanding the constructional processes that give rise to the inorganic structures of life it should be possible to develop a chemistry of form in the laboratory [4]. For example, complex small-scale inorganic architectures can be produced at room temperature by undertaking the precipitation reaction in self-assembled organic media, such as surfactant micelles, block copolymer aggregates and microemulsion droplets. Unusual inorganic forms emerge when these reaction fields are subjected to instability thresholds and

synthesis and self-assembly can be coupled to produce materials with higher-order organization. Like their biological counterparts, these hard inorganic structures represent new forms of organized matter that originate from soft chemistry [5,6].

Clearly, there is much to learn from the mechanical properties of biogenic inorganic materials. In addition, the micro-architecture of these materials depends ultimately on the biological regulation of molecular processes involving the nucleation, crystal growth and organization of mineral structure [1]. The task of this work is to produce synthetic protein mimics as model substances for mineralization. Biopolymers (proteins) in organisms, which control biomineralization, are too complicated, and the function of each part is still not known. Therefore it is advantageous first to simplify them by preparation of a polymer of one amino acid and then to try its activity in mineralization process.

2 Introduction

2.1 Biomineralization

2.1.1 Biominerals

A wide range of biominerals in organisms is known (Table 2-1-1), with most common are the carbonate and phosphate salts of calcium which conjunction with organic polymers such as collagen and chitin and function as structural support to bones and shells. Oxides of silicon and iron are also widespread. Biominerals are formed by normal cellular processes and replicate to produce precisely organized structures in cells ranging from bacteria, algae and protozoa to the osteoblasts of bone. The mineralization take place in membrane bound vesicles, within cells, in the mucilaginous layers of cell walls in bacteria, or impregnated in biopolymers in the extracellular space. In all these structures, the inorganic crystals are arranged in ordered arrays in association with a matrix of organic macromolecules. There is a growing body of information on the structure, composition and on the macromolecular processes that produce minerals of precise form with uniform particle size, novel crystal morphology and specific crystallographic orientation [7].

a)   b)   c)
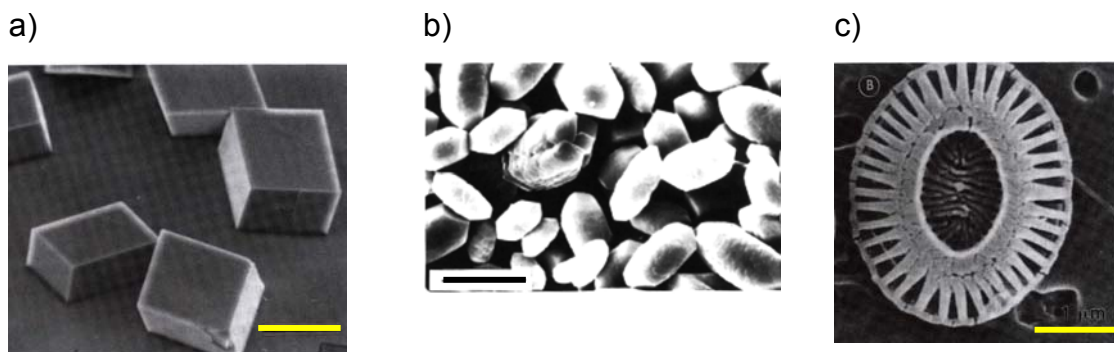
Figure 2.1-1: Example of the calcite modification form of $CaCO_3$, scale bar = 20μm. **a)** Rhombohedral synthetic calcite crystals [8], **b)** The mammalian inner ear calcite crystals (scale bar = 8μm) [1], **c)** Coccolith of *E. huxleyi*, scale bare = 1 μm [8].

In contrast to inorganic crystals, which may exhibit very complicated crystal structures but always have simple and regular geometrical shape as dictated by their

unit cell, biominerals consist of only a few and simple inorganic systems (Table 2.1-1) with simple crystal structures but often a complex form showing hierarchical ordering over several magnitudes of size. Calcium carbonate can be used as an example. The well-known rhombohedral synthetic calcite crystal compared to various macroscopic crystalline calcium carbonate forms in living organisms which also show a control of the crystal modification due to the nucleation and stabilisation of the thermodynamically metastable aragonite and vaterite illustrates the fidelity of morphogenesis in biomineralization processes (Figure 2.1-1).

Table 2.1-1: The types and functions of the main inorganic solids found in biological systems [8].

Mineral	Form	Formula	Organism/function
Calcium carbonate	Calcite	$CaCO_3$*	Algae/exoskeletons Trilobites/eye lens
	Aragonite	$CaCO_3$	Fish/gravity device Molluscs/exoskeleton
	Vaterite	$CaCO_3$	Ascidans/spicules
	Amorphous	$CaCO_3 . nH_2O$	Plants/Ca store
Calcium phosphate	Hydroxyapatite	$Ca_{10}(PO_4)_6(OH)_2$	Vertebrates/endoskeletons, teeth, Ca store
	Octa-calcium phosphate	$Ca_8H_2(PO_4)_6$	Vertebrates/precursor phase in bone
	Amorphous	?	Mussels/Ca store Vertebrates/precursor phase in bone
Calcium oxalate	Whewellite	$CaC_2O_4.H_2O$	Plants/Ca store
	Weddellite	$CaC_2O_4.2H_2O$	Plants/Ca store
Group IIA metal sulphates	Gypsum	$CaSO_4$	Jellyfish larve/gravity device
	Barite	$BaSO_4$	Algae/gravity device
	Celestite	$SrSO_4$	Acantharia/cellular support
Silicon dioxide	Silica	$SiO_2.nH_2O$	Algae/exoskeletons
Iron oxide	Magnetite	Fe_3O_4	Bacteria/magnetotaxis Chitons/teeth
	Geothite	α-FeOOH	Limpets/teeth
	Lepidocrocite	γ-FeOOH	Chitons (Mollusca) teeth
	Ferrihydrate	$5Fe_2O_3.9H_2O$	Animals and plants/Fe storage proteins

Calcite is the thermodynamic stable modification of calcium carbonate (Figure 2.1-1). For example, inside the inner ear there are hundreds of small calcite crystals that act as an inertial mass for the detection of changes in linear acceleration. These gravity devices function in a similar way as the fluid in the semicircular channels. The crystals are located on a membrane under which sensory cells are located. During a change in linear acceleration, the movement of the crystal mass relative to the delicate hair-like extensions of the cells results in the electrical signalling of the applied force to the brain. As a further example, hexagonally packed calcite single

crystals were used in the compound eyes of trilobites (eye lens) or individual coccolith scales of *E. Huxleyi* are formed with radial arrangement of oriented single crystals of calcite with hammer-headed morphology [9].

a)   b)   c)
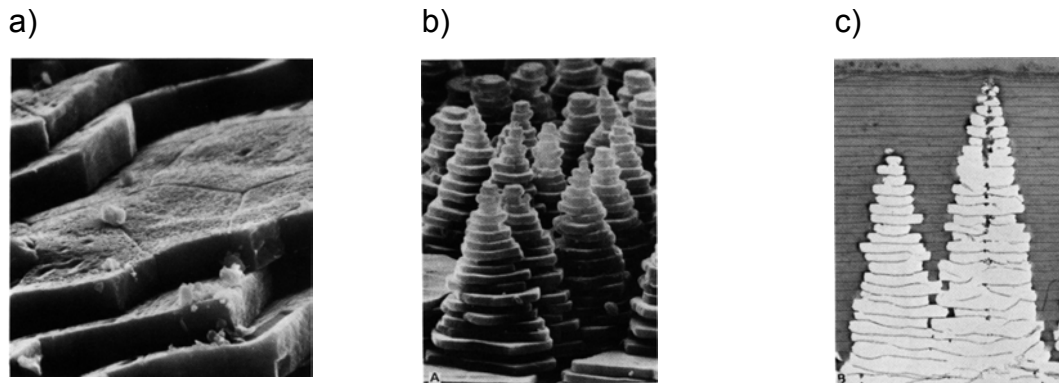
Figure 2.1-2: a) and b) SEM image of a mollusc shell showing multiple tiling of ≈ 200-500 nm thick aragonite crystals. **c)** TEM of the mollusc shell showing organic material in between of aragonite crystals [7].

Aragonite is a thermodynamically metastable form of calcium carbonate. In organisms it is stabilized through the adsorption of biological macromolecules such as polysaccharides at the solid surface. Figures 2.1-2a-b show scanning electron micrographs of the growth surface of the nacreous layer from the mollusc shell showing the stacked arrangement of the aragonite crystals. The Figure 2.1-2c shows the transmission electron micrograph of a growing stack within sheets of organic material periodically interspaced between the aragonite crystals.

Although most of the calcium carbonates formed in biological systems have structures of calcite or aragonite, some organisms deposit vaterite. This form is the least thermodynamically stable of the three non-hydrated crystalline polymorphs and rapidly transforms to calcite (Figure 2.1-3) or aragonite in aqueous solution. It occurs as spicules in a few marine sponges [10] (the majority of calcareous sponges have magnesium-rich calcite spines), where it possibly acts as a structural support or as a deterrent against predators.

Amorphous calcium carbonate is deposited in the leaves of many plants where it acts as a calcium store [11]. Although this material is exceedingly unstable in inorganic systems due to rapid phase transformation in aqueous solution, the

biogenic mineral appears to be stabilized through the adsorption of biological macromolecules.

a)
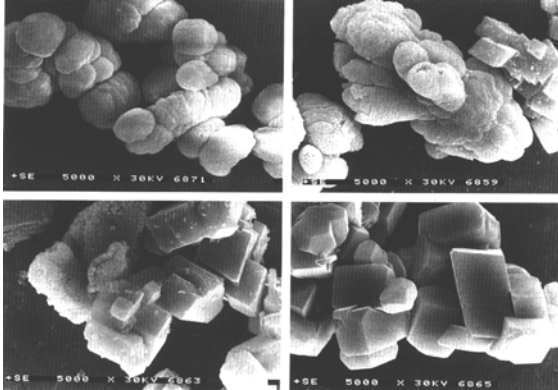
b)
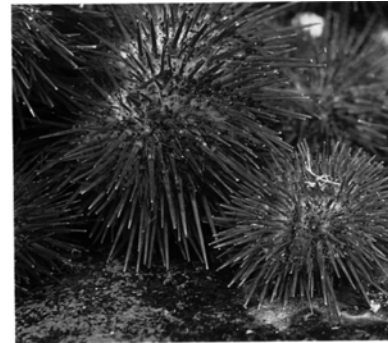
Figure 2.1-3: **a)** Transformation of vaterite to calcite [97], **b)** Ascidians. The spicules are made from vaterite [3].

At the nanoscale level, biomineralization involves the molecular construction of discrete, self-assembled, organic supramolecular systems (micelles, vesicles, etc.) that serve as reorganized environments for controlling the formation of finely divided inorganic materials, $\approx$ 1-100 nm in size. The fabrication of consolidated biominerals, such as bone or teeth, also involves the construction of reorganized frameworks, but the length scale is greater (micrometers) and the matrix is often polymeric (collagen, enamel tubules, etc.). The building if discrete or extended architectures in biomineralization often involves hierarchical processing in which the molecular-based construction of organic assemblies is used to provide frameworks for the synthesis of organized materials, which in turn are exploited as prefabricated units in the production of higher order complex microstructures.

The formation of calcified scales (coccoliths) in the marine *E. Huxleyi* (Figures 2.1-1c and 2.1-4) illustrates this process. The constructional problem is to build individual scales consisting of 30-40 calcite crystals arranged within an oval-shapes unit. The deposition of each crystal takes place at specific intracellular sites is requiring, and this is achieved by constructing discrete building plots around the inner ring. Thus, the first stage of organized assembly is the production of a series of membrane-bound vesicles that act as delineated reaction volumes for subsequent inorganic crystallization. The second stage of construction involves the oriented

nucleation of calcite crystals within these spatially discrete sites. Electron diffraction studies indicate that the crystallographic *c* axis of each crystal is aligned radially, suggesting that a molecular blueprint is encoded within each building site. Although the details are not fully known, it is probable that an organic matrix present within the vesicles is responsible for the templating of the crystal unit cell. The third stage of coccolith construction involves the vectorial crystal growth of the oriented calcite crystals such that the crystals adopt a complex architecture that includes a hammer-shaped extension.
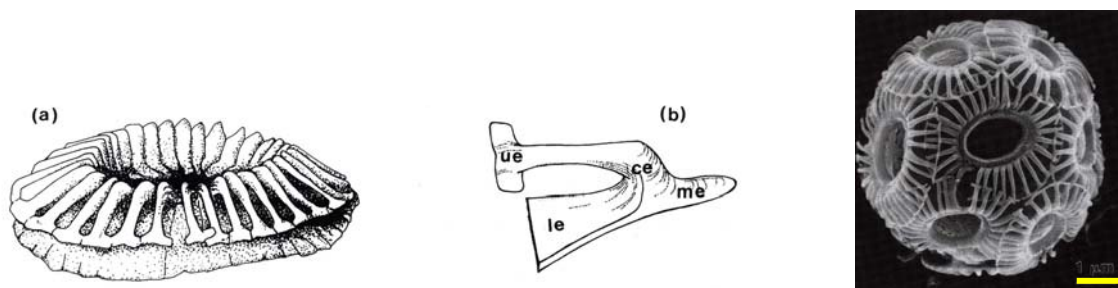
Figure 2.1-4: Intact coccosphere of *E. huxleyi* showing the assembly of coccoliths against the cell wall, scale bar = 1 μm [1].

2.1.2 Crystal engineering

It is clear that the distinction between synthetic minerals and biominerals lies in the extent of crystal chemical specificity exhibited by these materials. Although biominerals have relatively simple inorganic structures compared with those frequently obtained in synthetic solid-state chemistry, the level of engineering of the solid phase is often extremely high. For example, Figure 2.1-1a shows a single crystal of inorganic calcite ($CaCO_3$) formed in the laboratory. The crystal habit reflects the rhombohedral symmetry of the unit cell.

In contrast, Figure 2.1-5 shows a single crystal of biogenic calcite that constitutes the individual spine of an adult sea urchin. The spine shows none of the underlying crystallographic symmetry although the *c*-axis is aligned parallel to the morphological long axis. Recent chemical analyses of sea urchin spine indicate that the crystals contain only 0,02 wt% protein, which is one molecule per 10^5 unit cell [12]. This is sufficient to explain the conchoidal fracture of the biomineral and

associated mechanical properties. How these intracrystalline proteins are incorporated into the crystal structure whilst maintaining the high degree of long-range order is unknown.
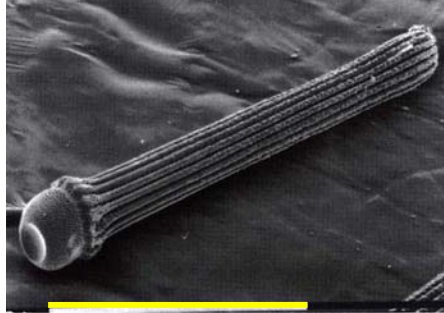
Figure 2.1-5: Single crystal of biogenic calcite (single sea urchin spine), scale bar = 1 mm [1].

The interplay between the precision of crystallochemical properties such as size, structure, composition, morphology and orientation, and the evolutionary requirements of organisms as expressed through functional properties is relevant within a technological context.

2.1.3 Controlled crystallization

The formation of a complex material such a sea urchin spine involves many features of control at the site of mineralization. The site must be delineated from the surrounding biological environments, activated at specific times in the life of the organism, constrained in size and shape and highly regulated with respect to the chemistry of the mineralization process. The principal processes to be controlled are nucleation and crystal growth both of which are critically dependent on the ionic composition (supersaturation) of the medium and the nature of interfaces (mineral matrix and mineral environment). Figure 2.1-6 present graphic representations of the different strategies for controlling supersaturation in biomineralization.

In general, the chemical processes are regulated by transport and / or reaction-mediated mechanisms. The delineation of the mineralization site by a surrounding organic membrane enables the supersaturation levels to be precisely regulated through facilitated ion-flux, complexation / decomplexation switches, local

redox and pH modifications or changes in local ion activities, the kinetics of surface-mediated processes such as cluster formation in nucleation, expression of crystal habit and phase transformations and aggregation in crystal growth [1].
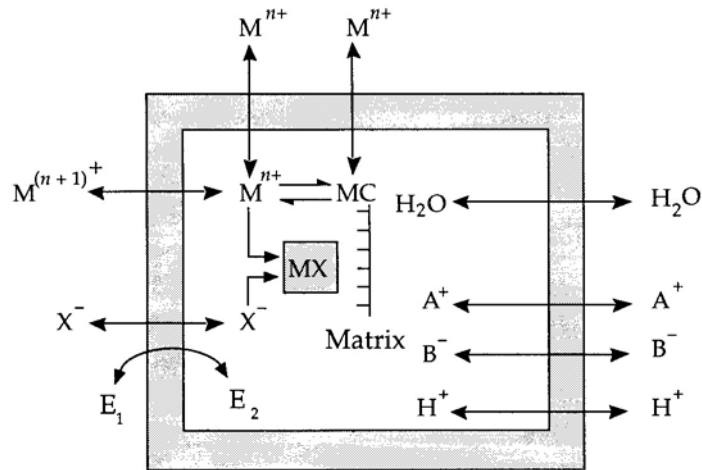
Figure 2.1-6: Generalised strategies for controlling supersaturation in biomineralization. M^{n+} = metal cations; X^- = anions; MC = cation complex; E_1E_2 = enzymes; MX = biomineral; A^+, B^- = extraneous ions [1].

The presence of macromolecular substrates is a key feature in many biomineralization processes and many systems are characterised as being "organic-matrix-mediated". The nucleation of an inorganic mineral at the surface of an organic matrix can be considered as a phase transformation reaction involving surface and bulk processes. There are two key structural factors in the use of organic matrices in controlled nucleation. Firstly, the matrix is preorganised with respect to nucleation through processes such as self-assembly, aggregation, membrane vesiculation and controlled polymerisation that impart spatial regulation of functional groups. Secondly, nucleation at the matrix surface is regiospecific with a limited number of sites being confined to discrete location. The role of an organic surface involved in inorganic crystallization is primaly to lower the activation energy of nucleation ($\Delta G^{\#}$). For the simplest case the activation energy of nucleation can be described by the following equation [8],

$$\Delta G^{\#} = \frac{B\sigma^3 \upsilon^2}{(kT\ln S)^2} \qquad\qquad (2.1\text{-}1)$$

where B is a constant ($16\pi/3$ for a spherical nucleus), σ is the interfacial energy, υ is the molecular volume, k is Boltzmann's constant, T is the absolute temperature and S the supersaturation.
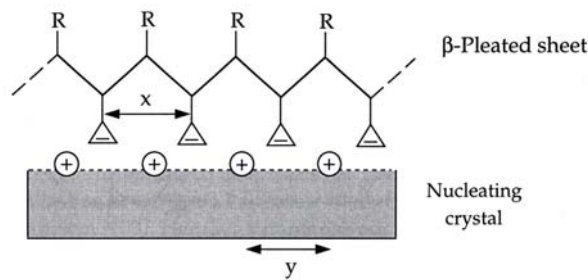
Figure 2.1-7: Geometric matching in biomineralization. Cation – cation distances in one specific crystal face are commensurate with the spacing of periodic binding sites on an organic surface [1].
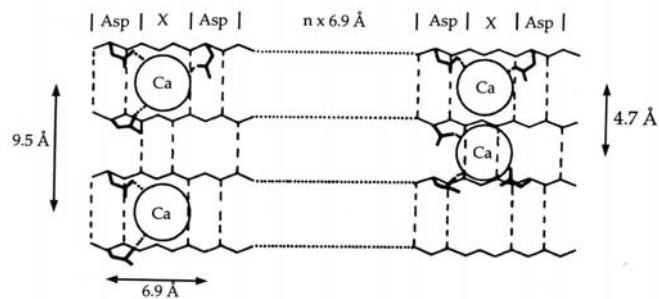
Figure 2.1-8: Proposed molecular correspondence at the inorganic-organic interface in the nacreous shell layer. There is a close match between the Ca-Ca distance along the aragonite *a*-axis and periodic spacing in the b-pleated sheet of protein. Sequences of Asp-X-Asp or polyAsp residues along the sheet provide the appropriate binding sites for orientated nucleation [1].

This specific lowering of the activation energy of nucleation reflects a requirement for structural and stereochemical complementarity between the inorganic and organic surface. Coordination environments in the mineral phase can be simulated by metal-ion binding to appropriate ligands exposed at the organic surface. Carbonate and phosphate biominerals tend to be associated with carboxylate-rich

(aspartate, glutamate) and phosphorylated (phosphoserine) proteins, respectively [13]. For example, the distance between aspartic acid residues deployed along a β-pleated sheet are similar to that of Ca-Ca distances in the nucleated aragonite (001) face observed in the mollusc shell (Figures 2.1-7 and 2.1-8) [14]

2.1.4 Biomimetic mineralization

There are a lot of examples of biomimetic morphosyntheses of inorganic structures. Low molecular weight additives that have molecular structures with variable conformational states interact with inorganic crystal surfaces principally through electrostatic and stereochemical processes. For example, α-ω-dicarboxylic acids $[(CH_2)_n(CO_2H)_2]$ are effective in stabilizing faces essentially parallel to the $\{1\bar{1},0\}$ surface of calcite provided that both carboxylate groups are ionised and $n < 3$ (Figure 2.1-9) [15]. These faces contain both Ca^{2+} and CO_3^{2-} ions with the latter oriented such that the plane of the triangular anion is perpendicular to the surface. Thus incorporation of carbonate anions into the $\{1\bar{1},0\}$ face during growth occurs through bidentate binding of two of the three oxygen atoms to Ca^{2+} ions on the surface. This stereochemical arrangement can also be adopted by binding of the dicarboxylate to the crystal surface (Figure 2.1-10) [6]. Moreover, both carboxylates in the additive molecule can bind simultaneously to two different calcium ions if the spacing between CO_2^- groups is close to 0,4 nm. This selective growth inhibition is the simplest form of morphosynthesis and leads to significantly different crystal morphologies (Figure 2.1-1a for the default calcite morphology).

Another example of controlled mineralization is transient foams produced by spreading a thin film of a supersaturated $CaCO_3$ microemulsion onto a metal substrate and partially removing the oil phase by washing with hot hexane. This destabilizes the microemulsion film and causes microphase separation of the remaining oil and supersaturated aqueous solution into a self-organized foam-like array of submicrometer-sized oil droplets surrounded by supersaturated aqueous fluid. Growth of the inorganic crystal then occurs in the interstitial spaces and boundary edges between the oil droplets to produce a mineralised imprint of the

cellular structure. This approach has been used to prepare disordered frameworks of CaCO$_3$ (Figure 2.1-11) [16].
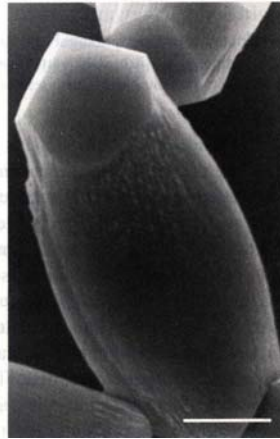
Figure 2.1-9: SEM micrograph of a spindle-shaped calcite crystal grown from supersaturated calcium bicarbonate solution in the presence of malonate at [Ca^{2+}] : [malonate] = 3,16.Crystal faces approximately parallel to the *c* axis are severely inhibited by the additive. Scale bar = 5 μm [4].
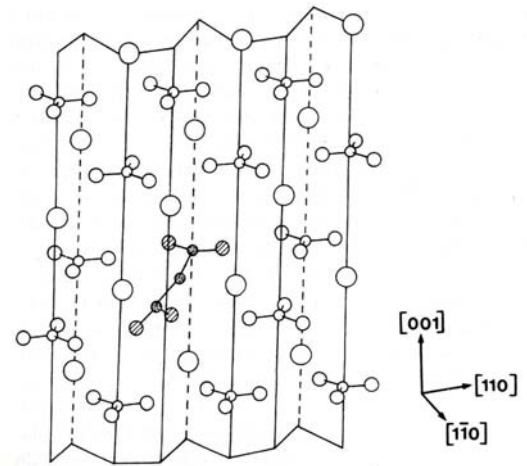
Figure 2.1-10: Perspective drawing of the calcite $\{1\bar{1},0\}$ face showing a possible binding site for malonate anoin [4].
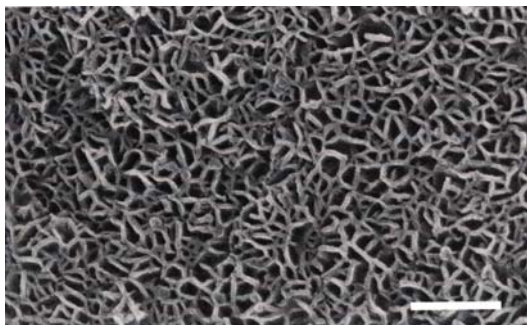
Figure 2.1-11: SEM image of a cellular film of CaCO$_3$ (aragonite) synthesized by reaction field replication in transitory oil droplet biliquid foam. Scale bar = 1 μm [4].
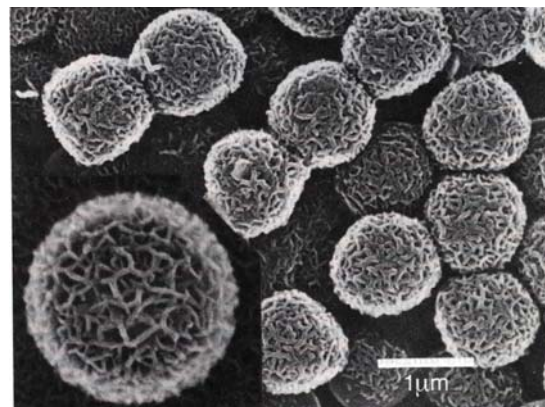
Figure 2.1-12: SEM image of intact hollow shells of mesoporous aragonite. Inset shows a high-magnification SEM image of an intact shell with well-defined cellular substructure. Scale bar = 1 μm [4].

Sculpting these cellular films into closed microshells produces a structure that can be loosely described as biomimetic coccoliths (Figure 2.1-12) [16]. This is achieved by spreading the microemulsion film over micrometer-sized polystyrene beads and subsequent washing with hot hexane. Hexane is a suitable solvent because it does not dissolve the polymer template but induces demixing and mineralization of the transient cellular structure. The beads are then dissolved in chloroform or destroyed by heating to give a porous hollow shell of cellular calcium carbonate [6].

a)

b)
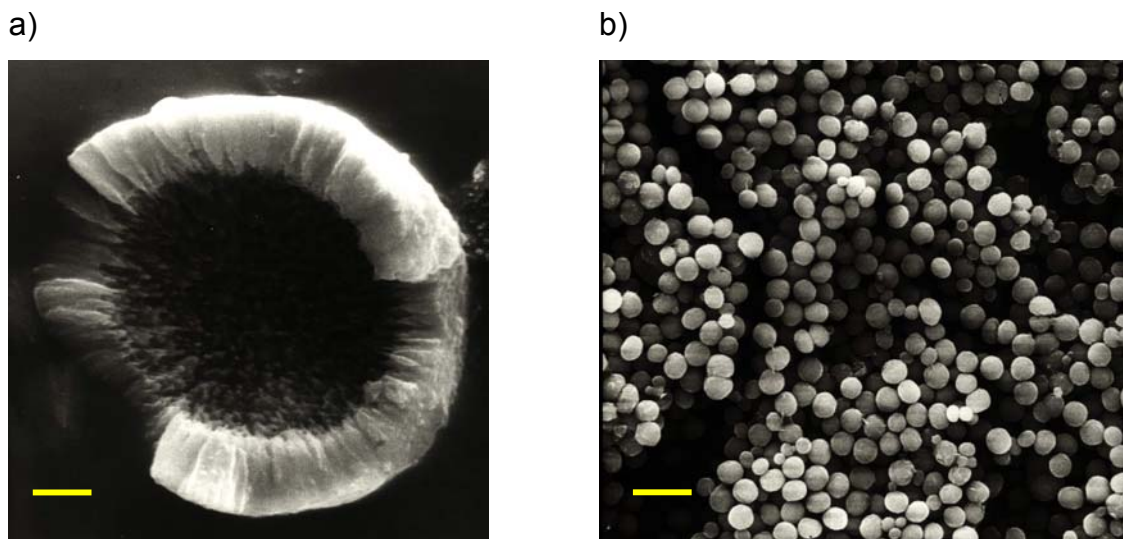
Figure 2.1-13: Observed morphologies for $CaCO_3$ in presence of double hydrophilic block copolymers, a) PEG-*b*-PMAA-PO$_3$H$_2$, scale bar 2 μm, b) PEG-*b*-PEDTA, scale bar 5 μm [92].

This higher order assembly is applied in biomineralization as it allows adding curvature to crystalline systems by building structures through aggregation of nanocrystals often in a shaped confined reaction volume and it is known from classical colloid chemistry. For example, spherical $CaCO_3$ microparticles are considered which represent superstructures of nanocrystals building units (Figure 2.1-13) [17 - 20].

2.2   Concept of double hydrophilic block copolymers

Amphiphilic block copolymers which turned out to be advantageous for the stabilisation of colloids or for the formation of a rich variety of polymeric superstructures as each block can be designed in an optimum way for the desired use so that different functions are separated within one molecule [21].

Amphiphilic block copolymers usually consist of a hydrophilic and hydrophobic block so that they can be considered as polymeric surfactants. Indeed, they show the same behaviour as low molecular mass surfactants with the difference of a lower critical micelle concentration (cmc) and slower exchange dynamics. Consequently, as in the case of low molecular mass surfactants, the formed superstructure can already be predicted from the block lengths and simple geometric considerations [22]. However, the term amphiphilicity could be generalised in a way that a molecule has an affinity to two different substrates regardless the nature of these substrates. One very important substrate is the surface of an inorganic crystal that can be extensively modified by additives. This purpose can be achieved advantageously with so called double hydrophilic block copolymers (DHBC) [23].

Figure 2.2-1: DHBCs and their superstructure formation in a presence of a substrate.

A double hydrophilic block copolymer is a block copolymer that consists of two water-soluble blocks of different chemical nature. These polymers are typically rather

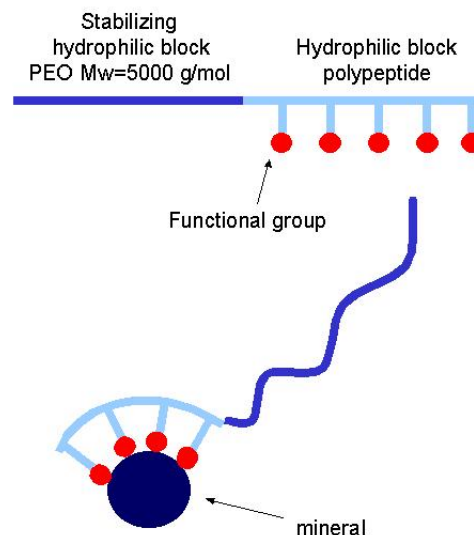small with block lengths between 10^3 - 10^4 g/mol. In many cases, one block just promotes dissolution whereas the other interacts with a substrate (Figure 2.2-1).

In solution, DHBC's behave like normal polymers, resp. polyelectrolytes and show no characteristics of amphiphiles such as micelle formation or lowered surface tensions of their solution. The amphiphilicity is induced as soon as the molecules come into contact with a substrate, for example a mineral surface, leading to an interaction with the substrate resulting in complex or superstructure formation. Alternatively, temperature, ionic strength or pH variation as well as a complexation reaction can completely reverse the hydrophilicity of one block into hydrophobicity. In this case, DHBC's represent reversibly switchable amphiphiles with new applications. Special cases of DHBC's are polyampholytes consisting of a polycation and polyanion block [24], being able to act as a substrate itself. Thus, these polymers show pH dependent complex formation.

DHBC's are a promising copolymer class for the biomimetic synthesis of model hybrid colloids with complex form starting from small building units which are initially stabilised by the block copolymer as indicated in Figure 2.3-1. Defined fictionalisation patterns can be generated on the sticker block to vary the interaction strength with the mineral. On the other hand, the block length of the solvating block can be adjusted in a way that a loss of electrostatic particle stabilisation results in a slow particle aggregation process or a still remaining steric stabilisation. These new polymer class could direct new potential applications such as for the preparation of environmentally friendly particle stabilisation, and many other technically applications.

Double hydrophilic block copolymer are model polymers to mimic proteins as they combine their hydrophilic moieties with their charged moieties so that the complicated protein interactions with crystals can be much simplified.

2.3   Ring opening polymerisation of N-carboxyanhydrides

The ring opening polymerisation of α-aminoacid-*N*-carboxyanhydride (NCA) is currently the most common technique used for large-scale preparation of polypeptides. However, these materials are almost exclusively homopolymers, random copolymers, or graft copolymers, which lack the sequence specificity and

monodispersity of natural proteins [25]. It is noteworthy that α-amino acid NCAs are also useful for the synthesis of oligo- and polypeptides with well-defined sequences of various amino acids. The preparation of the enzyme ribonuclease-S may be mentioned in this connection.
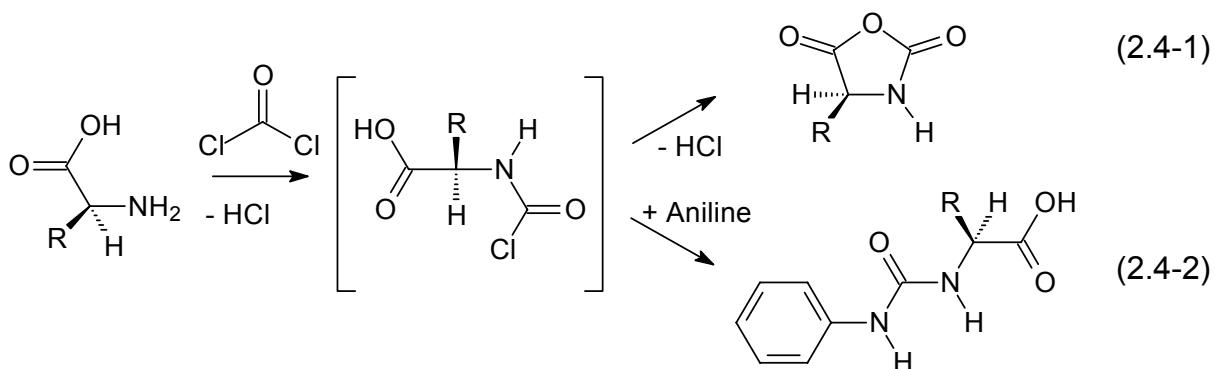
Scheme 2.3-1: Preparation of α-aminoacid-*N*-carboxyanhydride by reaction of amino acid with phosgene.

In 1906, Herman Leuchs presented his first report [26] on the synthesis and polymerisation of an α-aminoacid-*N*-carboxyanhydride (oxazolidine-2,5-dione). This historic report, along with two later papers [27, 28] is of particular interest, because it described the synthesis of a polymer at a time when polymer science did not yet exist. Leuchs prepared *N*-ethoxycarbonyl and *N*-methoxycarbonyl amino acid chlorides for the purpose of stepwise peptide synthesis. Upon heating in vacuum, cyclization was observed, instead of distillation, yielding NCAs along with alkylchlorides. The main shortcomings of the original Leuchs method are the relatively high cyclization temperatures, which come close to the point where several NCAs begin to decompose.

The simplest and most widely used method for the preparation of α-aminoacid-*N*-carboxyanhydride is the direct reaction of the free amino acid with phosgene [29-35]. This procedure is called the *Fuchs-Farthing method*, after its inventors. The reaction mechanism involves the intermediate formation of *N*-chloro-formyl amino acids (Equation 2.4-1), because addition of aniline yields 5-phenyl hydantoic acid [32,36] (Equation 2.4-2). In general inert, low-boiling-point solvents are suitable reaction media (most widely used solvents are Tetrahydrofuran and dioxane). Larger quantities of NCAs are best prepared in a boiling mixture of THF (or

dioxane) and methylenechloride (1 : 1) because hydrochloric acid is less soluble under these conditions than in pure ethers. The concentration of hydrochloric acid is important, because HCl can cleave the NCA ring, whereby amino acid chloride hydrochlorides are formed as first reaction products. Their phosgenation finally yields α-isocyanato acid chlorides (Equation 2.4-3). The main disadvantage of *Fuchs-Farthing method* is the need to work with phosgene gas that is highly toxic. Triphosgene could be used as a phosgene substitute, which is easier to handle and give comparable yields in reasonable reaction times. First Daly and Poché used it for preparation of NCAs [37]. Triphosgene, prepared by exhaustive chlorination of dimethyl carbonate, is a crystalline solid, which can be safely handled and stored; no catalyst is required to deliver three equivalents of phosgene *in situ*. Removal of any residual triphosgene from the NCA is accomplished by recrystallization of the product. Triphosgene undergoes nucleophilic attack at the carbonyl carbons; the trichloromethoxy leaving group dissociates to a chloride anion and a molecule of phosgene, which reacts immediately [38].

$$\text{HCl . } H_2N\!-\!CHR\!-\!COCl \xrightarrow[-3\ HCl]{COCl_2} O\!=\!C\!=\!N\!-\!CHR\!-\!COCl$$
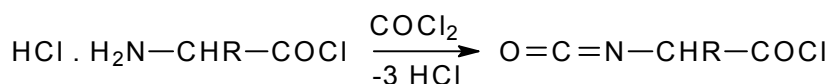
Scheme 2.3-2: Reaction of amino acid chloride hydrochlorides with phosgene.

The stepwise synthesis of oligopeptides and the preparation of high molecular weight polypeptides required NCAs of high purity in order to be successful. The method of synthesis of NCAs determines the contaminants to be expected. Because most NCAs are easily crystallisable compounds in contrast to the contaminants, a series of two or three recrystallization from suitable mixtures of solvents and nonsolvents is the standard purification procedure.

α-aminoacid-*N*-carboxyanhydride possesses four reactive sites (two electrophilic and two nucleophilic centers), and this multiple reactivity, in combination with the ability to polymerise, is responsible for the relatively complex chemistry of NCAs. The two electrophilic centers are the carbomoyl group (C-2) and the carbonyl group (C-5). The two nucleophilic sites are the NH and the α-CH groups, which after deprotonation yield highly nucleophilic amide anions and carbanions, respectively.

The reaction pathways of NCAs largely depend on the nature of the initiator. It is well known that neither radicals, nor cations, nor acids initiate the polymerisation of NCAs. Nonetheless, in addition to heat, the four most important classes of initiators are protic nucleophiles, aprotic nucleophiles, aprotic bases, and organomethalic compounds.

2.3.1 Primary amines as initiators
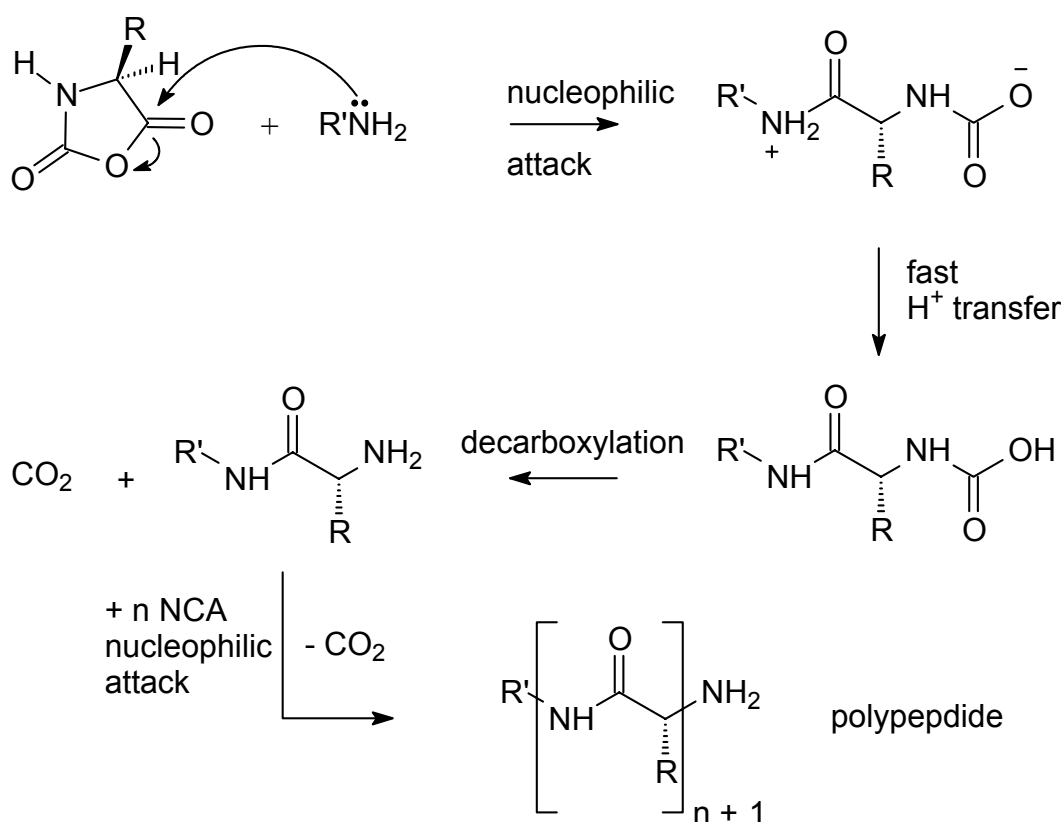
Scheme 2.3-3: Mechanism for polymerisation of NCAs initiated by primary amine.

Primary amines, which are more nucleophilic than basic, are good general initiators. In the presence of primary amines, NCAs polymerise according to the so-called normal mechanism (Figure 2.3-3) The reaction is a simple nucleophilic attack of the NCA ring at the carbonyl C-5 with opening chain growth process where the polymer grows linearly with monomer conversion in the absence of a side reaction. The reaction is followed by decarboxylation. Each initiator molecule originates one

polymer chain, and the number-average degree of polymerisation ($\overline{DP}_n$) is given by the molar ratio of monomer to initiator (A : I) as typical for a living polymerisation.

Polymerisation initiated by a primary amine gives block copolymers of α-amino acids as a preformed sequence of a given residue, carrying a terminal free-amino group used to initiate the polymerisation of the NCA of a different residue. The length of the added block depends on the molar ratio between the initiator and the second monomer [39]. For double hydrophilic block copolymers with poly (ethylene oxide) as a first block and polypeptide as a second block α-methoxy-ω-amino[poly(ethylene oxide)] could be used as a macroinitiator.

3   Characterization methods

3.1   Characterization of polymers

3.1.1 Gel permeation chromatography (GPC)

Gel permeation chromatography (GPC) [40], also known as size exclusion chromatography (SEC), is a standard technique frequently used to determine the molar mass distribution (MMD) of polymers and thus the corresponding number, weight, and *z* averages, M_n, M_w, and M_z.

In GPC separation is an accomplished with respect to the hydrodynamic volume of the macromolecules. The stationary phase is a swollen gel with a characteristic pore size distribution, and depending on the size of the macromolecules a larger or smaller fraction of the pores is accessible to the macromolecules (Figure 3.1-2).

In *ideal* GPC, separation is exclusively achieved due to the hydrodynamic volume of the macromolecules without any interaction of the polymers with the column material and therefore the enthalpy change ΔH for ideal system is zero, thus

$$K_d = K_{SEC} = \exp\left(\Delta S \middle/ R\right)$$
(3.1-1)

where K_d is the distribution coefficient, K_{SEC} the distribution coefficient for GPC, ΔS is change of entropy, due to the inside pores, which have limited dimensions as the macromolecule cannot occupy all possible conformations.

Since the conformational entropy decreases $\left(\Delta S < 0\right)$, the distribution coefficient of ideal GPC is $K_{SEC} < 1$. The maximum value, $K_{SEC} = 1$, is related a constant conformational entropy, i.e. to a situation where the complete pore volume is accessible to the macromolecules (separation threshold). At $K_{SEC} = 0$, the analysed molecules are too large to penetrate into the pores (exclusion limit). Accordingly, the separation range is $0 > K_{SEC} < 1$.

The retention volume for ideal GPC is

$$V_R = V_i + V_p K_d = V_i + V_p K_{SEC} \tag{3.1-2}$$

where V_R is the retention volume, V_i is interstitial volume and V_p is the entire pore volume.

If enthalpic effects, due to electrostatic interactions between macromolecules and the pore walls, have to be taken into account, the distribution coefficient K_d of real GPC is as follows:

$$\Delta G = \Delta H - T\Delta S = -RT \ln K_d \tag{3.1-3}$$

$$\begin{aligned} K_d &= \exp\left(\frac{\Delta S}{R} - \frac{\Delta H}{RT}\right) \\ &= \exp\left(\frac{\Delta S}{R}\right)\exp\left(-\frac{\Delta H}{RT}\right) = K_{SEC} K_{LAC} \end{aligned} \tag{3.1-4}$$

where R is the gas constant and T is the absolute temperature. ΔH is the change in enthalpy and ΔS is the change in conformational entropy when 1 mol of solute is transferred from the interstitial volume into the pores of the column material under standard conditions. In this case, the retention volume is a function of K_{SEC} and K_{LAC} (coefficient of liquid adsorption chromatography). If electrostatic interactions occur at the outer surface of the stationary phase as well, an additional term $V_{Stat} K_{LAC}$ has to be accounted for.
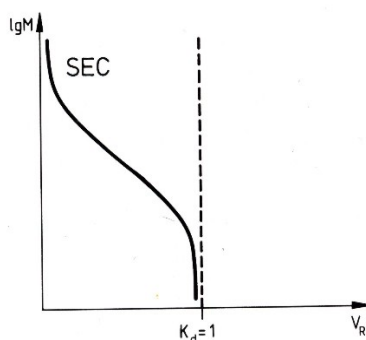

Figure 3.1-1: Chromatographic behaviour molar mass vs. retention volume in the size exclusion mode.
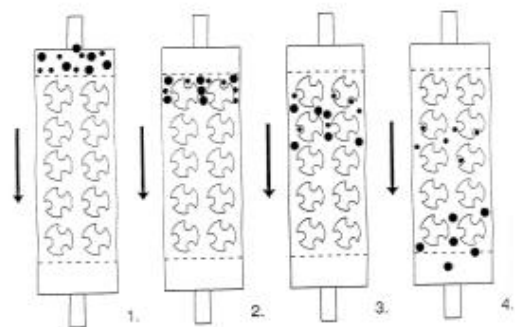
Figure 3.1-2: GPC Separation of two different macromolecules according to their size.

The molar mass vs. retention volume behaviour in the size exclusion mode is given in Figure 3.1-1. The smaller the macromolecules the more pore volume they can penetrate and, accordingly, the longer they are retained in the stationary phase. Therefore, first the large macromolecules are eluted followed by macromolecules of smaller size (Figure 3.1-2).

The principle of GPC is explained best by a schematic representation (Figure 3.1-3), which shows the first part of an analysis by GPC: from the sample to a chromatogram.
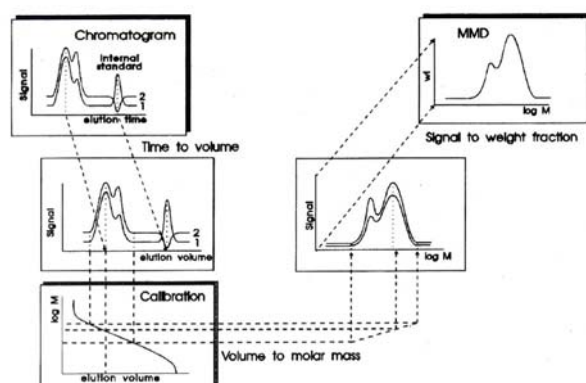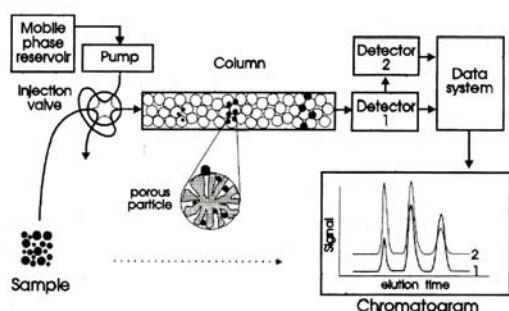
Figure 3.1-3: Principle of size exclusion chromatography [40].

Figure 3.1-4: Basic steps in obtaining a molar mass distribution from a chromatogram [40].

When the separated polymer molecules leave the column, they have to be detected by one or more detectors. The signal has to represent the concentration of the polymer with good accuracy. In the analysis of polymers by GPC, only a limited number of the numerous HPLC detectors can reasonably be applied (Table 3.1-1).

Table 3.1-1: View of detectors for GPC.

Concentration sensitive detectors		Molar mass sensitive detectors
Selective detectors	Universal detectors	
UV detector	RI detector	Single capillary viscometer
IR detector	Conductivity detector	Differential viscometer
Fluorescence detector	Density detector	LALLS, MALLS, TALLS, RALLS
Electrochemical detector	Evaporative light scattering detector	

GPC is only a relative technique. Making a calibration with polymer standards of the same polymer is necessary. Especially copolymers analysis is difficult (no standards) and often, an interaction with the column material can occur (HPLC mode) especially for water soluble polyelectrolytes, so that no molar mass distribution can be obtained anymore.

Synthetic copolymers have both, molecular weight and chemical composition distributions. Copolymer molecules of the same molecular size, which are eluted at the same retention volume in SEC, may have different molecular weight in addition to different compositions. This is because separation in SEC is achieved according to the size of the molecules in solution, not to their molecular weights. Therefore, determination of accurate values of molecular weight averages and a molecular weight distribution for a copolymer is limited to cases where the copolymer has a homogeneous composition across the whole range of molecular weights [41].

3.1.2 MALDI-TOF spectroscopy

Matrix Assisted Laser Desorption/ionisation-Time of Flight-Mass Spectroscopy (MALDI-TOF) was developed in 1988 by Hillenkamp and Karas for the analysis of large biomolecules [42, 43], but it was not demonstrated until 1992 that also synthetic polymers can be analysed with a molecular weight above 100 000 Da. There are two main reasons for this delay: 1) the methods of sample preparation for biopolymers with water-based solvents were not applicable to most synthetic polymers and 2) synthetic polymers are always polydisperse. Thus, the technique had to be further developed for synthetic polymers.

MALDI-TOF works similarly to the laser desorption (LD) method developed earlier [44], It is a "soft" ionisation technique for transferring large molecular ions into a mass-spectrometer without fragmentation. The matrix isolates the sample molecules from each other, absorbs most of the laser energy, and assists in the formation of protonated or methylated ions. In principle, the sample to be investigated is mixed in such a ratio that matrix separation of the sample molecules is achieved. Such a ratio ranges from 500:1 to 10 000:1 (matrix : sample). After drying, a laser pulse is directed onto the solid matrix to photoexcite the matrix material. This excitation

causes the matrix to decompose explosively, resulting in the expulsion and soft ionisation of the sample molecules. The matrix strongly absorbs the radiation to enhance the rate of heating [45]. Only one charge is induced per polymer chain in contrast to the multiple changes in electrospray mass spectrometry of polymers.

The matrix has to have high electronic absorption at the employed laser wavelength (λ = 337 nm of a nitrogen laser), good vacuum stability, good solubility in organic solvents (used for dissolving the analyte), and good miscibility with the analyte in the solid state. In the analysis of biopolymers, where the ionisation usually takes place via proton transfer, the matrix also plays the role of the proton source, whereas in the analysis of synthetic polymers, ionisation is usually achieved by cation attachment, which is a matrix-independent process. Some commonly used matrices for synthetic polymers are dithranol (1,8,9-trihydroxyanthracene), DHB (2,5-dihydroxybenzoic acid), IAA (3-β-indoleacrylic acid), sinapinic acid (3,5-dimethoxy-4-hydroxy cinnamic acid) and 5-chlorosalicylic acid. There is no general rule how to select the ideal matrix for a given polymer. The selection of a good matrix is still a trial and error process and has to be worked out each time a new polymer class is under investigation.

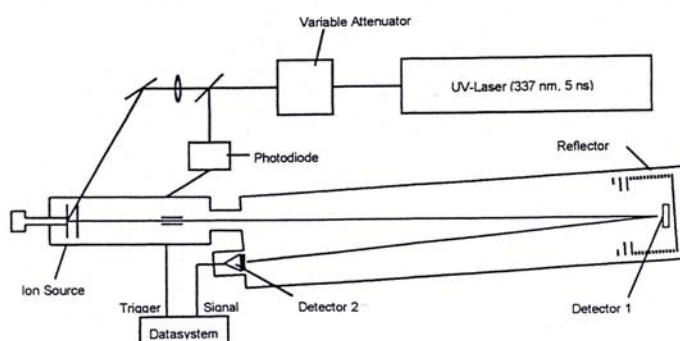**Figure 3.1-5:** Reflection time-of-flight mass spectrometer [46].

The MALDI method is ideally combined with a time-of-flight (TOF) mass spectrometer. Figure 3.1-5 shows a typical set-up of an instrument equipped with a matrix assisted laser Desorption ion source.

The ions are produced in most commercial instruments by irradiation of the sample with a pulsed nitrogen laser. The intensity of the laser beam can be adjusted

by a variable attenuator to a value slightly above the threshold for ion production. The laser beam is focused on the sample surface in the ion source. Once the ions are formed after a laser pulse, they are accelerated simultaneously by a static electric field (of up to 35 kV). Depending on their mass-to-charge ratio, they have different velocities when they leave the acceleration zone and pass the following field-free drift tube with different flight times. The time-of-flight for each ion is then measured by the time difference between the start signal, given by the laser pulse and the stop signal, caused by the ions impinging on the detector.

According to the Equation 3.1-7, the square of the flight time is proportional to the mass-to-charge ratio.

$$\frac{m}{z} = \frac{2Ut^2}{s^2} \qquad\qquad (3.1\text{-}7)$$

where m is the mass of the ion, z is the number of charges, U is the accelerating voltage, t is the ion flight time and s the flight distance. Since the accelerating voltage and the length of the drift tube are known, the mass-to-charge ratio can be calculated. In practice, more exact values for the mass scale can be obtained from the empirical equation 3.1-8 because of uncertainties in the determination of the flight time. This uncertainty is due to a short delay in ion formation after the laser pulse, so that the real starting time of the ions is not identical to the time of the laser pulse, which provides the starting signal for the measurement of flight time.

$$\frac{m}{z} = at^2 + b \qquad\qquad (3.1\text{-}8)$$

where m is the mass of the ion, z is the number of charges, t is the ion flight time and a,b are constants. The constants a,b are measured by the flight times of two ions with known masses, which are used for calibration.

3.2   Circular Dichroism (CD)

Circular Dichroism (CD) and the optical rotatory dispersion (ORD) are special variations of absorption spectroscopy in the UV and VIS region of the spectrum [47]. The basic principle of the two methods is the interaction of polarized light with optically active substances. If a linearly polarized light wave passes through an optically active substance, the direction of the polarization will change, which is wavelength dependent. This phenomenon is called optical rotatory dispersion (ORD). Linearly polarized light waves can be described as a superposition of two circularly polarized light waves. If a substance absorbs these two circularly polarized components to a different extent, i.e. if the absorption coefficient for the right circularly polarized component of the polarized light is different from the absorption of the left circularly polarized light; this difference is described as circular dichroism (CD).

In 1848 Louis Pasteur observed that sodium ammonium tartarate from wine crystallizes in two forms that can be separated and that are optically active and rotate polarized light with the same angle into opposite directions (left and right). Such optically active substances are called chiral. Only chiral substances can be optically active.

If linearly polarized light passes through an optically active substance, it is possible that not only the speeds, $c_L \neq c_R$, of the two circularly polarized components are different, which leads to different wavelengths $\lambda_L \neq \lambda_R$, but also the absorption coefficients, $\varepsilon_L \neq \varepsilon_R$. The difference in the absorption coefficient is determined. Since the absorptions of the left circularly polarized light and the right circularly polarized light are different, elliptically polarized light emerges from the sample. In practice of CD spectroscopy the ellipticity Θ (in degree) is determined from the difference of the absorption coefficients

$$\Theta_\lambda = const(\varepsilon_L - \varepsilon_R) \cdot c \cdot d \qquad const = \frac{180}{4\pi} \ln(10) \approx 33 \qquad (3.2\text{-}1)$$

where c is the concentration of the sample and d is the thickness of the measuring cell. The molar ellipticity is then given by

$$[\Theta]_\lambda = \frac{M_r \Theta_\lambda}{10 \cdot d \cdot c} \qquad \text{(Grad.cm}^2\text{/mol)} \qquad (3.2\text{-}2)$$

where M_r is the molar mass. The CD-spectrum has the form of an absorption band and a positive and a negative circular dichroism is observed as a function of the wavelength, depending which of the two circularly polarized components is absorbed stronger.
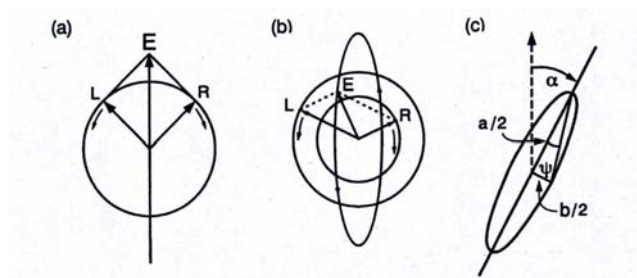

Figure 3.2-1: a) Plane-polarized light resolved into two circularly polarized components, R and L. As long as intensities and phases of the two circularly polarized components remain the same, their resultant will lie in a plane and oscillate in magnitude. **b)** If the right circularly polarized component is less intense (absorbed more) than the left circularly polarized component, the electric vector of the light follows an elliptically path, as shown, corresponding to elliptically polarized light. **c)** The semi major and semi minor axes of the ellipse from a triangle and the angle opposite the semi minor axis is the angle, ψ, the ellipticity. This major axis of the ellipse has been rotated through the angle α, corresponding to the optical rotation [47].

The optical rotation can be positive (right rotating) or negative (left rotating). Direction and angle depend on the wavelength. A chromophor with a positive Cotton effect causes a right rotation at low frequency and a left rotation at higher frequencies. A chromophor with a negative Cotton effect causes a left rotation at low frequencies and a right rotation at the higher frequencies (Figure 3.2-2).
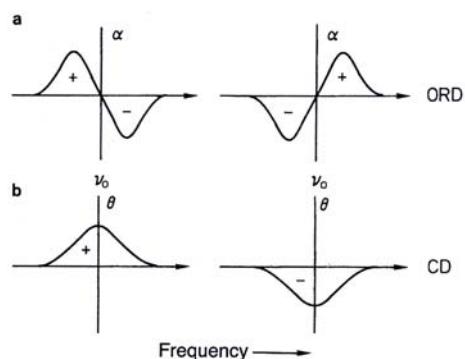
Figure 3.2-2: Positive and negative Cotton effect of an absorption band. **a)** In the ORD spectrum, **b)** In the CD spectrum [47].

CD is a widely used technique for studying the secondary structure of biopolymers, polypeptides and proteins as well as DNA and RNA. Protein chains are coiled or folded in an ordered way largely dependent on a maximization of hydrogen bonding between amino acid residues. Proteins having more than one polypeptide chain also pack these together in an ordered way (i.e. DNA double helix). Three types of conformations are commonly seen: an α-helix, a β-sheet (β-strand) and the irregular conformations of globular proteins (random-coil) (Figure 3.2-3).

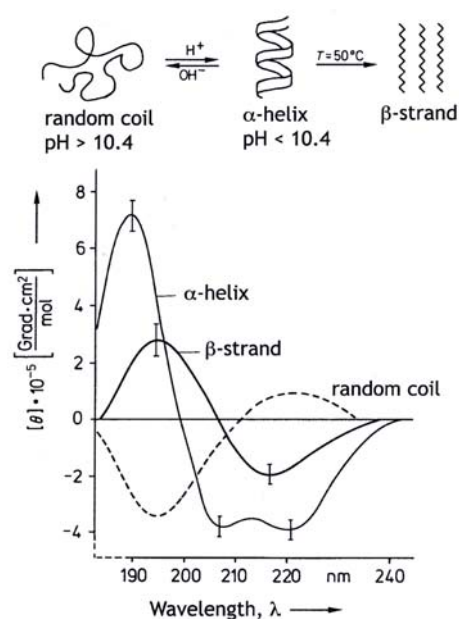**Figure 3.2-3:** Conformational changes and CD-spectra of poly-*L*-lysine in aqueous solution.

The CD-spectra are different for each secondary structure due to the difference between two electronic transitions, which have been characterized in condensed-phase spectra between 180 and 250 nm. These are an $n - \pi^*$ transition at $210 - 230$ nm and a $\pi - \pi^*$ transition at $180 - 200$ nm.

In the CD-spectrum of an α-helix polypeptide, the negative 222 nm band is due to the peptide $n - \pi^*$ transition, while the negative 208 nm and positive 192 nm bands result from exciton splitting of the peptide $\pi - \pi^*$ transition.

The characteristic CD features of the β-sheet are a negative band at ca 216 nm ($n - \pi^*$ transition) and a positive band of comparable magnitude near 195 nm ($\pi - \pi^*$ transition). The CD of β-sheet polypeptides shows much more pronounced variations with solvent and side chain than it is the case with the α-helix.

A positive band near 218 nm ($n - \pi^*$ transition) and a strong negative band just below 200 nm ($\pi - \pi^*$ transition) characterize the CD of random coil.

3.3   Electron microscopy

Electron microscopy [48-50] uses a beam of highly energetic electrons to examine objects on a very fine scale. This examination can yield the following information: Topography, Morphology, Composition and Crystallographic information. Electron microscopes were developed due to the limitation of light microscopes that are limited by the physics of light to 500× or 1000× magnification and a resolution of up to 0,2 μm.

Electron microscopes (EMs) work similar as their optical counterparts except that they use a focused beam of electrons instead of light to "image" the specimen and gain information as to its structure and composition.
The basic steps involved in all EMs are:

1.   A beam of electrons is formed by the electron source and accelerated towards the specimen using a positive electrical potential.
2.   This bream is confined and focused using metal apertures and magnetic lenses into a thin, focused, monochromatic beam.
3.   This beam is focused onto the sample using a magnetic lens.
4.   Interactions occur inside the irradiated sample, affecting the electron beam.

There are two types of EM: the so-called scanning electron microscopy (SEM) for surface observation using secondary electrons emitted from the specimen surface; and transmission electron microscopy (TEM) using electrons transmitted through thin specimens.

In TEM, electrons are emitted by the cathode (with wavelength 0,005-0,002 nm) and are accelerated by a high voltage (60–200 kV) due to the difference of the cathode and the anode potential. Then, they pass through two condenser lenses, which reduce the minimum cross section of the beam and focus it onto the object. In the small space inside the objective, miniature specimen holders are introduced having a goniometric head that enables movement and orientation of the specimen as needed, including tilting up to 60°. The specimen is placed either directly on a special microgrid or on a grid coated with a supporting film. Passing through the object, the electrons are scattered within some fixed angle. The objective aperture restricts this angle. The intermediate lenses and the projecting lens magnify the object image formed by the objective lens. The image is visualized on a screen or the EM picture is projected on a display and recorded photographically. The resolution in TEM is about 2-5 nm.

In SEM, electrons from a thermionic or field emission cathode are accelerated (by a voltage of 1-50 kV) between the cathode and the anode. A condenser system focuses a very fine electron beam on a small area – a "point" of the specimen surface. A special deflecting system scans the surface of the specimen with an electron beam. Thus, by successive recording of its different areas, the image is formed. The "response" with any kind of radiation from a given microregion of the specimen is recorded, and the response from a "point" is presented in the corresponding point of the image. The resolution depends on the diameter of the beam. In the best commercial, reflecting SEM apparatus it is 5-30 nm. SEM is the most efficient instrument for investigating the morphology and microrelief of a bulk material.

EM may suffer from drying artifacts, so that it is very valuable to combine the high resolution information from EM with light microscopy in solution as long as the sample is large enough (> 1 μm).

3.4   Wide angle X-Ray scattering (WAXS)

X-ray scattering is a powerful technique for the study of crystal and liquid crystal structure. When a monochromatic X-ray beam hits on a crystal, the scattered electromagnetic waves from the regularly placed atoms interfere with each other, giving strong diffraction signals in particular directions, since the interatomic distances are of the same order as the X-ray wavelength (typically ~ 0,05 – 0,2 nm). The often used Cu-K$_\alpha$ radiation has the wavelength of 0,154 nm = 1,542 Å.

For diffraction the path difference between waves scattered from successive planes of atoms in the crystal must equal an integral number of the wavelength, $n \, (n = 1,2,3...)$ (Figure 3.4-1). This condition is expressed by the Bragg equation (3.4-1) [48,49]

$$n\lambda = 2d \sin \Theta \qquad (3.4\text{-}1)$$

where d is the distance separating successive planes in the crystal and Θ is the angle of the incident beam with the planes.
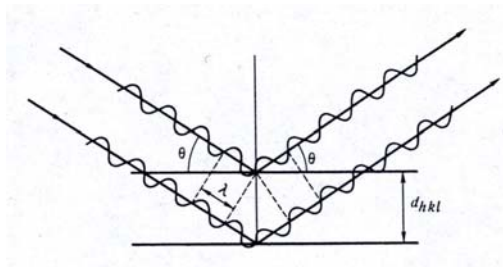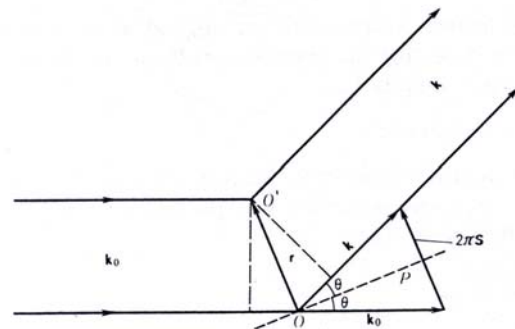

Figure 3.4-1: Bragg reflection [49].

Figure 3.4-2: Scattering by two point centres [49].

A useful construction for helping in the interpretation of X-ray diffraction patterns is equation 3.4-2, which introduces the scattering vector $|S|$

$$|S| = \frac{2 \sin \Theta}{\lambda} = \frac{1}{d} \qquad (3.4\text{-}2)$$

perpendicular to plane *P* in Figure 3.4-2.

X-ray scattering techniques are usually categorized into wide-angle X-ray scattering (WAXS) and small-angle X-ray scattering (SAXS). In the former, the desired information on the inorganic material is contained in the intensities at large scattering angles 5° - 180°, in an atomic scale of 1 nm or smaller ($\sim 10^{-2}$ nm). The information on the structure of colloid or polymer systems is contained in the intensities at small scattering angles 0° - 5°, scale 1 - 2000 nm.

3.5   Mineralization techniques

In order to study the influence of various molecules on crystal growth ($CaCO_3$ and $BaSO_4$), it was first necessary to consider suitable methods of crystallization. An ideal system would reproducibly grow the crystals, in high yield with well-defined equilibrium morphologies and a homogeneous size distribution. In this work, the Kitano- and Double-Jet method were used.

3.5.1 Kitano method

The *Kitano method* [51] is a method for slow crystallization and it is used for the growth of crystals of calcium carbonate. The crystals are nucleated at the air / water interface and are close to the equilibrium morphology. With no additives well-defined and reproducible rhombohedral crystals characteristic of calcite were produced.

$$K = \frac{\left[Ca^{2+}\right]\left[HCO_3^-\right]^2}{p_{CO_2}} \tag{3.5-1}$$

At a given temperature, the solubility of calcium carbonate in pure water is highly dependent on the pH that is directly linked to the carbon dioxide CO_2 content. When a suspension of calcium carbonate in water (bidest.) (pH = 8,0 - 8,4) is

saturated with carbon dioxide CO_2, the equilibrium $CaCO_3$ / HCO_3^- is shifted to the right (equation 3.5-1 and Scheme 3.5-1).

$$CaCO_3 + CO_2(g) + H_2O(l) \leftrightarrow Ca^{2+}(aq) + HCO_3(aq)$$
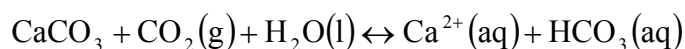
Scheme 3.5-1: The equilibrium of $CaCO_3$ / HCO_3^- .

Thus, at normal atmospheric pressure, $p_{CO_2} = 0,0003\,\text{atm}$, the pH is about 8,1 and the total calcium concentration 0,5 mM. Whilst at $p_{CO_2} = 1\,\text{atm}$ partial pressure, pH=6, the concentration of calcium ~ 10 mM. Bubbling CO_2 through a saturated solution dissolves $CaCO_3$ until a new equilibrium is established. The rest of $CaCO_3$ is then filtered to produce a clear, supersaturated solution of calcium bicarbonate (pH = 5,8 - 6,0). The subsequent lowering of p_{CO_2} in the solution (due to out gassing of CO_2) will lead to precipitation as the reaction shifts back to the left.

The CO_2 content and hence the solubility of calcite in natural water can be quite variable. For example, rainwater often becomes enriched in calcium as it percolates through soil with a higher than atmospheric carbon dioxide content. $CaCO_3$ may then crystallize when this solution is re-exposed to atmospheric conditions. Stalactites in subterranean caves are formed under these circumstances. Hydrothermal waters, under great pressure in the earth's crust, carry significant quantities of dissolved calcium due to similar reasons. Another important phenomenon involving this system is the biological-induced deposits. Photosynthetic activity by aquatic organisms often results in localized regions of water being undersaturated with CO_2. Consequently, minerals accumulate at these specific sites that may be in the immediate vicinity of the organism or actually on the cell surface itself.

3.5.2 Double-Jet method (DJ)

To test the crystallization control efficiency of the various synthesized block copolymers for $CaCO_3$ or $BaSO_4$, a double jet set-up can be used (Figure 3.5-1). This method is a fast crystallization method producing nanocrystals uniform in size and

shape. This technique was used for the first time for the production of various inorganic particles of uniform size, especially in the photographic industry for making silver halide of desired well-developed habits [52].
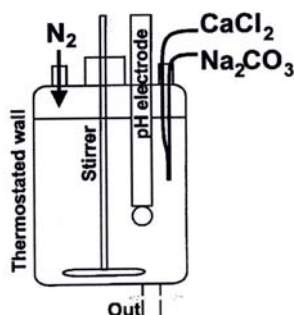

Figure 3.5-1: Double-Jet reactor [53]

The main idea behind this technique is to maintain a rapid nucleation of a constant particle number to enable growth of monodisperse particles. The two reactants are continuously injected via capillaries into the reaction vessel under vigorous stirring to prevent heterogeneous nucleation on the glass walls at controlled flow rates under precisely defined conditions (temperature, time, pH, etc.). The two capillaries ends are joined together at their ends so that a high local reactant concentration and thus extreme supersaturation is achieved at the moment when the two reactants leave the capillaries. This provides an immediate nucleation of $CaCO_3$ (or $BaSO_4$) according to the LaMer model [54]. The nuclei are then immediately transported to regions of lower $CaCO_3$ (or $BaSO_4$) concentration and can grow further, be stabilized or dissolved again at the beginning of the experiment. The $CaCO_3$ / $BaSO_4$ crystal formation occurring after excess addition of reactants is easily observed as a sudden increase in the turbidity of the solution. This time is recorded as an onset of crystallization. The time when macroscopic crystals could be observed in the withdrawn samples is defined as the time of completed crystallization.

The crystallization control efficiency of different block copolymers can be defined by Equation (3.5-2). The mass ratio s_m directly defines the mass of polymer which can keep a defined mass of $CaCO_3$ / $BaSO_4$ in colloidal solution [53].

$$s_m = \frac{m_{pol}}{m_{CaCO_3}} \tag{3.5-2}$$

A lower ratio indicates a better $CaCO_3$ / $BaSO_4$ stabilization on a colloidal scale, i.e., molecular binding, respectively.
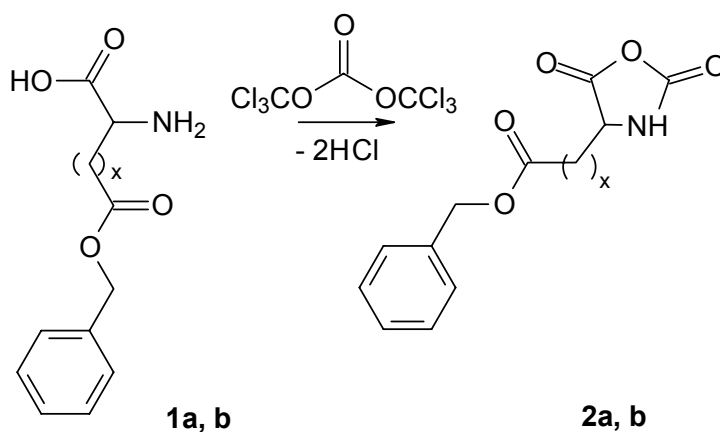
4   Synthesis and characterization of polypeptide-block copolymers

4.1   Synthesis of *N*-carboxyanhydrides (NCA's)

4.1.1   *N-carboxyanhydride of L-aspartic acid 4-benzyl ester (2a) and L-glutamic acid 5-benzyl ester (2b)*

Classical *N*-carboxyanhydride (NCA) synthesis applies the gaseous phosgene [30 - 35], which is highly toxic (10 times than chlorine gas) and furthermore, it is difficult to add in the proper stoichiometric balance, for more details see chapter 2.3.

Nowadays, NCA's are mostly prepared by reaction with bis(trichloromethyl) carbonate (triphosgene) [37], which is a crystalline solid and can be safely handled and stored. Its decomposition without any catalyst yields three equivalents of phosgene *in situ* and it is very well soluble in typical solvents for NCA's for example tetrahydrofuran (THF) and hexane.

Scheme 4.1-1: NCA of *L*-aspartic acid 4-benzyl ester (**2a**) (x=1) and *L*-glutamic acid 5-benzyl ester (**2b**) (x=2).

For the NCA synthesis of aspartic acid (**2a**) and glutamic acid (**2b**) (Scheme 4.1-1) THF is used as a solvent [55]. Those two amino acids are not soluble in THF, on the other hand NCA's of both amino acids are soluble, so it is easy to recognize the end of the reaction. The treatment of an amino acid suspension in anhydrous

THF with 1/3 eq. of triphosgene at 40 - 50 °C leads to a completely homogeneous solution of the corresponding NCA within 1 - 3 hours. It is very important to work under anhydrous conditions during the entire reaction, because the anhydride is very reactive and reacts even with atmospheric moisture or water that is inadvertently introduced into the monomer during its production or isolation. The partial NCA hydrolysis would change the monomer / initiator ratio and thus the peptide block length.

The probably most ubiquitous impurities found after synthesis of an NCA are HCl and the HCl salt of the starting amino acid. When the convenient phosgenating reagent, triphosgene, is used, it can also severely limit polymerisation of the NCA if residual triphosgene persists in the monomer. These impurities can react instead to prematurely terminate the chain growth. All amino initiators of polymerisation are effectively "killed" by the presence of HCl. Finally, the residual Cl⁻ ions are known to be an effective initiator in solvents such as DMF and can therefore introduce unpredictable changes in the molar mass and molar mass distribution of the resulting polymer.
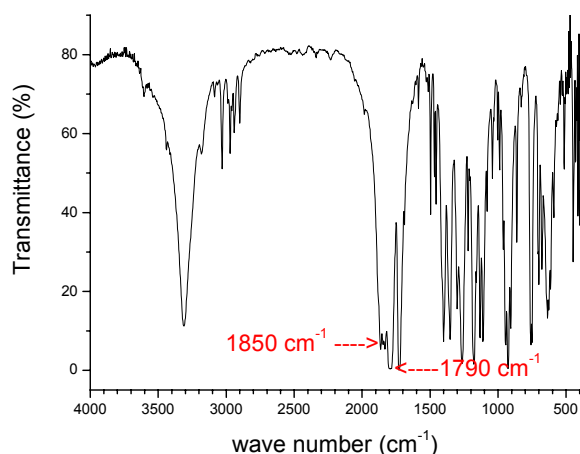
Figure 4.1-1: IR spectrum of the NCA of *L*-aspartic acid 4-benzyl ester (**2a**).

Most often, the NCA derivatives are purified by repeated crystallization from a THF / petrol ether mixture (both previously dried) after thoroughly sparking the reaction mixture with nitrogen, to remove the excess quantities of triphosgene. Another method of the NCA purification is very fast washing with cold water and cold 0,5% solution of sodium bicarbonate. In this case ethyl acetate has to be used as a solvent due to its insolubility in water. It is advantageous to chill the reaction prior to washing to prevent decomposition of the NCA during the contact with water and to reduce the

mutual solubility of the two phases. In all cases it is found that the bicarbonate solution wash is neutral to slightly basic after contact with the reaction mixture. The advantage of this method is that both HCl and the HCl salt of the amino acid remaining after the reaction can be washed into the water layer.

The composition of the resulting NCA can be confirmed by IR spectroscopy. The bands indicating NCA ring formation are at approximately 1850 cm^{-1} and 1790 cm^{-1} (Figure 4.1-1). Other methods are the melting point measurement and the elemental analysis.

4.1.2 NCA of O-benzyl-L-serine (7)

For the NCA syntheses of O-benzyl-L-serine (7) [55, 56] the triphosgene method was used and the product was washed and recrystallized as described for the NCA of L-aspartic acid 4-benzyl ester (2a) and L-glutamic acid 5-benzyl ester (2b).

In the synthesis of the serine NCA is important to protect the functional group of the side chain (-OH) in order to avoid side reactions. Therefore, a further difficulty in the preparation of polyamino acids from serine is the removal of the protecting groups from the masked polypeptide. In case of glutamic and aspartic acid it is easy, as the carboxyl group is a functional group of the side chain. Thus, this group could be protected via an ester bond, for example L-aspartic acid 4-benzyl ester (1a). The benzyl group is a good leaving group, thus deprotection does not need any drastic conditions and can be achieved. In case of serine, there are some difficulties, a widely used protecting group for -OH is benzyl connected via an ether bond. For the removal of this protecting group, an autoclave has to be used (see chapter 4.3).

The synthesis of the NCA of L-serine (4) (without any protection of –OH function group) was tried as well (Scheme 4.1-2) [57]. This reaction depends on the solvent. When dioxane is used, and the reaction is carried out at room temperature, L-serine-N-carboxyanhydride (4) is obtained within 2 - 3 hours but with a very low yield (around 20%). Continuation of the reaction for 32 hours leads mainly to the formation of O-chlorocarbonyl-L-serine-N-carboxyanhydride (5). When tetrahydrofuran is used, O-chlorocarbonyl-L-serine-N-carboxyanhydride (5) is already

formed after two hours of reaction. Both compounds were identified by elementary analyses [58].
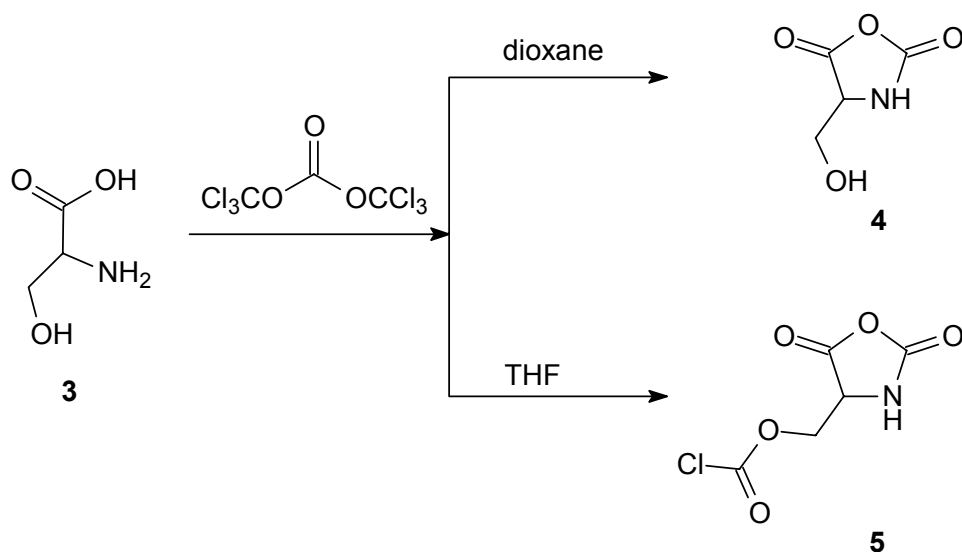
Scheme 4.1-2: NCA of *L*-serine (**5**).

These results show that it is better to use protecting groups for the -OH functional group. The reaction of *O*-benzyl-*L*-serine (**7**) with triphosgene (Scheme 4.1-3) was carried out using dioxane as a solvent and 20% excess of triphosgene with respect to the stoichiometric balance. If this 20% excess is not sufficient (the reaction mixture is still in suspension after 2 hours) higher excess could be used, or the rest of *O*-benzyl-*L*-serine (**6**), which did not react, could be filtered off. This reaction gives yields around 90%.
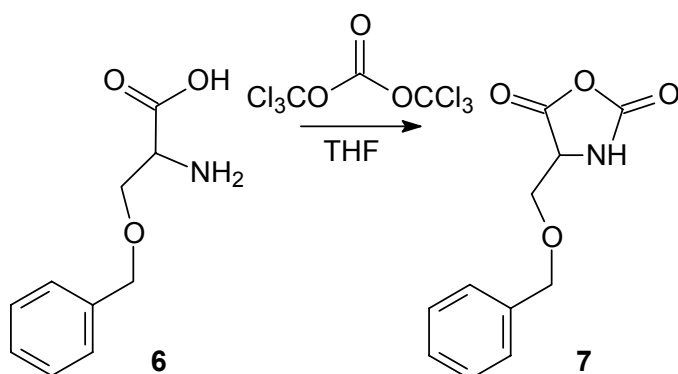
Scheme 4.1-3: NCA of *O*-benzyl-*L*-serine (**7**).

Figure 4.1-2: NCA of *O*-benzyl- *L*-serine (**7**).
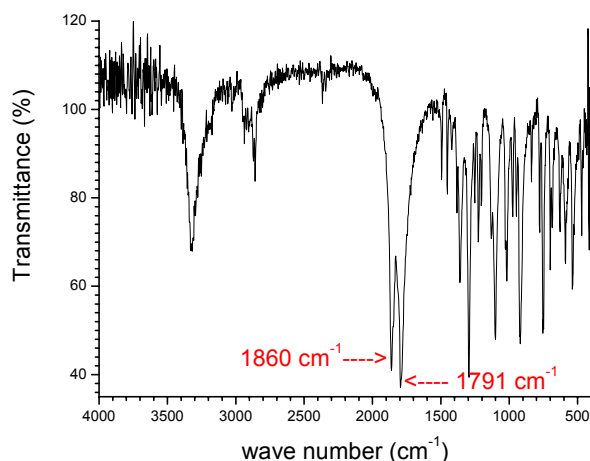
The composition of resulting the NCA can be confirmed by IR spectroscopy, melting point measurement and elemental analysis. The bands in IR spectrum indicating NCA ring formation are at approximately 1860 cm^{-1} and 1791 cm^{-1} (C=O bond vibration of cyclic anhydride) (Figure 4.1-2).
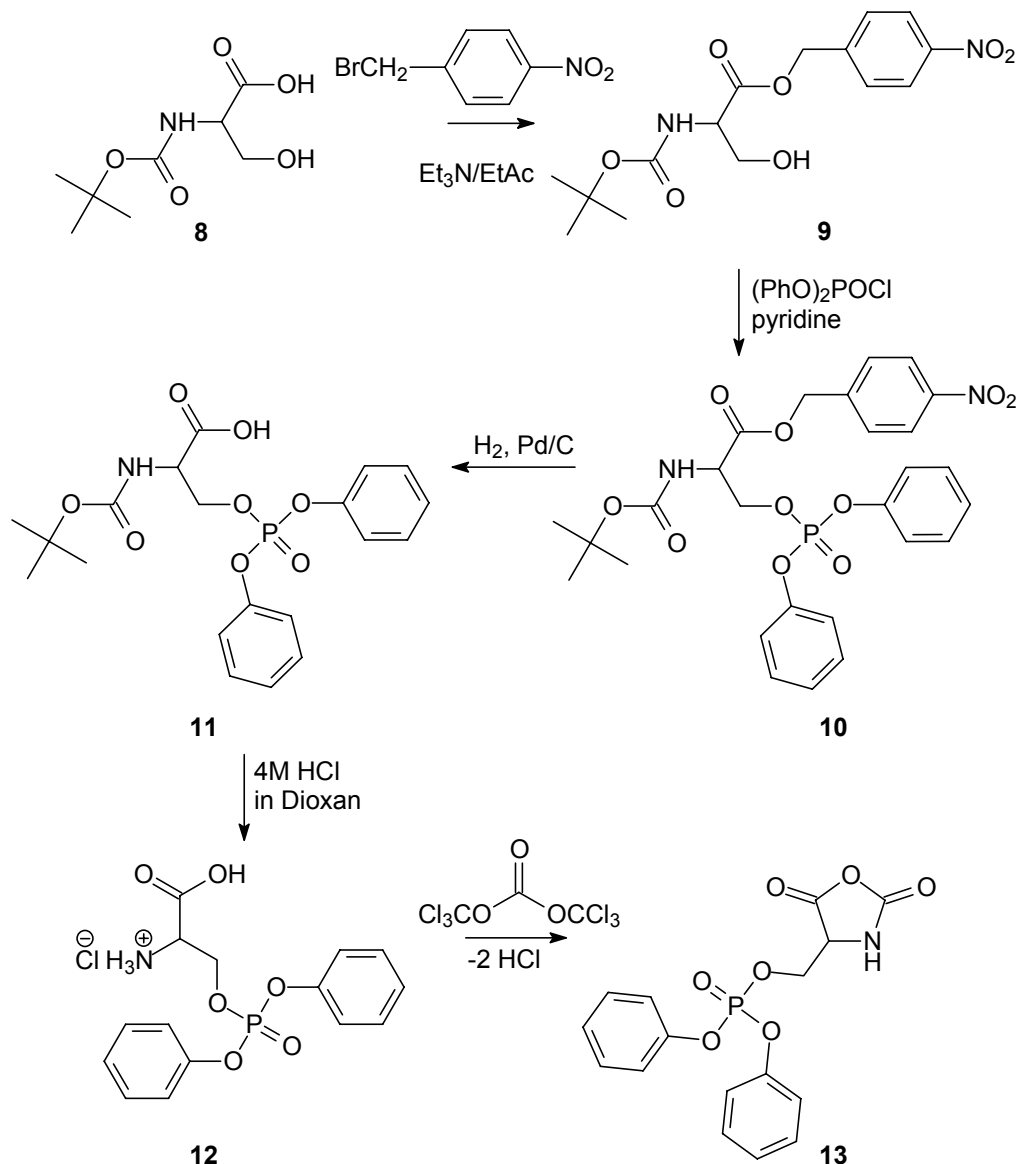
4.1.3 NCA of O-diphenylphospho-L-serine (13)

In the previous chapter the synthesis of NCA of *O*-benzyl-*L*-serine (**7**) is described. This NCA is then used for the ring opening polymerisation with α-methoxy-ω-amino[poly(ethylene glycol)] (**14**) as a macroinitiator, followed by deprotection of the -OH functional group of the side chain and subsequent phosphorylation of the -OH group. This is one way how to obtain a phosphorylated block copolymer, another method is first to phosphorylate *L*-serine (**3**) and then use this compound for the NCA preparation (Scheme 4.1-4).

The preparation of the *O*-diphenylphospho-*L*-serine NCA (**13**) is accomplished by a five-step synthetic procedure [59]. The first step is the 4-nitrobenzyl protection of the carboxyl group of N^α-*tert*-butoxycarbonyl-*L*-serine (**8**) with high yields around 93%. The presence of a nitrobenzyl group in a molecule of N^α-*tert*-butoxycarbonyl-*L*-serine 4-nitrobenzyl ester (**9**) [60] can be proven by a UV-VIS spectrum, which shows a maximum at λ = 270 nm, by elemental analyses (presence of two N atoms in one molecule), and by ^{1}H NMR spectra. Furthermore, ^{13}C NMR spectra show signals in the aromatic region. This reaction takes exclusively place on the COOH group,

because of the difference between acidity of the COOH and the OH groups (the COOH group is approximately 10^{10} times acidic than the OH group, thus COO$^-$ group is better nucleophile than -OH).

Scheme 4.1-4: Synthesis of the NCA of *O*-diphenylphospho-*L*-serine (**13**).

This step is followed by phosphorylation of the free OH groups. As a phosphorylation reagent diphenyl chlorophosphate is used and the whole reaction is performed under argon protective gas. This step gives N^{α}-*tert*-butoxycarbonyl-*O*-diphenylphospho-*L*-serine 4-nitrobenzyl ester (**10**) [61] also in a high yield around 93% and the degree of phosphorylation is 98% (checked by ^{31}P NMR spectroscopy), that means the

phosphorylation is quantitative and resulting polymer has 98% degree of phosphorylation.

The next step is the deprotection of the carboxyl group by hydrogenation with palladium on active charcoal as a catalyst. Purification of N^{α}-*tert*-butoxycarbonyl-*O*-diphenylphospho-*L*-serine (**11**) requires a long washing procedure (see experimental details), which results in a considerable reduction of the yield (59%). The structure of this intermediate product was proved by the melting point measurement, the elemental analysis, UV-VIS, ^{1}H NMR spectroscopy and ^{13}C NMR spectroscopy (no signal in aromatic region).

The fourth step is the cleavage of the *tert*-butoxycarbonyl group by hydrolyses with 4N HCl in dry dioxane under argon protective gas. The yield is around 92%. The product of this step, *O*-diphenylphospho-*L*-serine hydrochloride (**12**), can be characterized by the melting point, the elemental analyses, ^{1}H NMR, ^{13}C NMR.
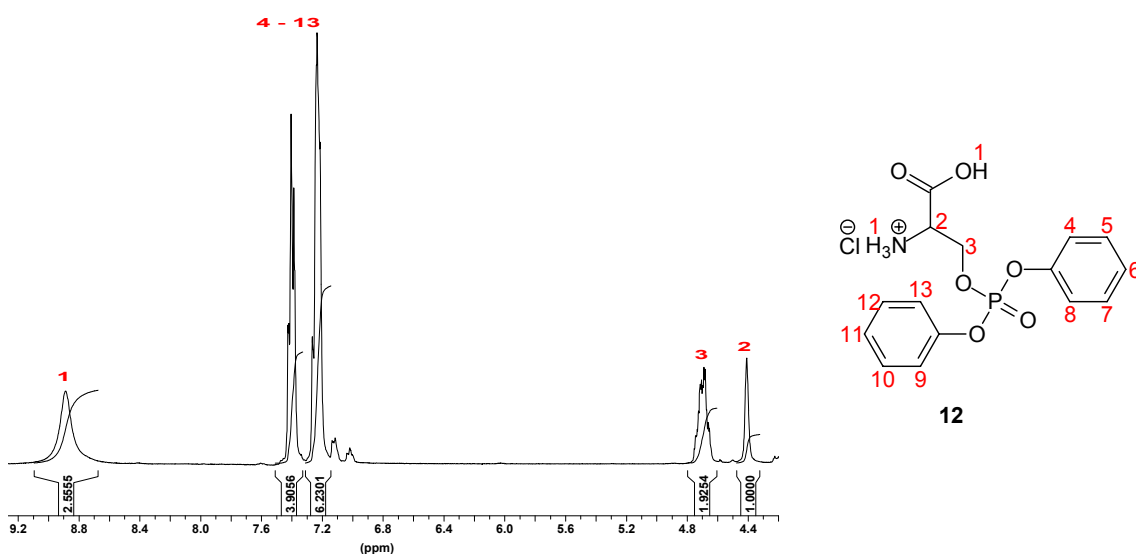
Figure 4.1-3: ^{1}H NMR spectrum the of the *O*-diphenylphospho-*L*-serine hydrochloride (**12**).

Figure 4.1-3 shows ^{1}H NMR spectrum of *O*-diphenylphospho-*L*-serine hydrochloride (**12**), there are two signals in the aliphatic region, the first one at δ = 4,40 ppm correspond to the hydrogen of α-CH group and the other one at δ = 4,69 ppm) to the two hydrogens of CH$_2$ group. The signals in the aromatic region at δ = 7,23 – 7,40 ppm correspond to ten hydrogens of phenyl groups and the last signal at δ = 8,89 ppm is for the hydrogens of the amino and the carboxyl groups.
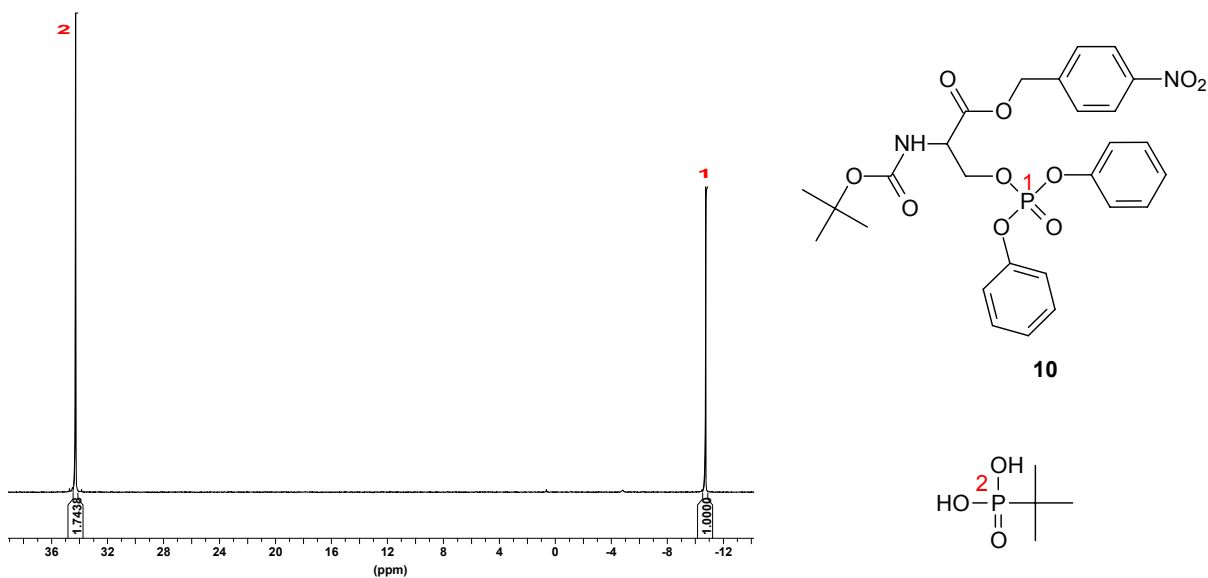
Figure 4.1-4: ^{31}P NMR spectrum of the N^{α}-*tert*-butoxycarbonyl-*O*-diphenylphospho-*L*-serine (**10**) and the external standard *tert*-buthylphosphonic acid.

Figure 4.1-4 shows ^{31}P NMR spectrum of Figure 4.1-5: ^{31}P NMR spectrum of the N^{α}-*tert*-butoxycarbonyl-*O*-diphenylphospho-*L*-serine (**11**). There are two signals, the *tert*-buthylphosphonic acid signal is at δ = 34 ppm and the sample signal is at δ = - 10,23 ppm. The external standard was used for the quantitative analysis of the phosphorylation degree.

Figure 4.1-6: IR of *O*-diphenylphospho-*L*-serine NCA (**13**).

For the preparation of the *O*-diphenylphospho-*L*-serine NCA (**13**) the analogue method as for the NCA of *L*-aspartic acid 4-benzyl ester (**2a**) and *L*-glutamic acid 5-benzyl ester (**2b**) was used. As a difference, dry dioxane was used as a solvent and

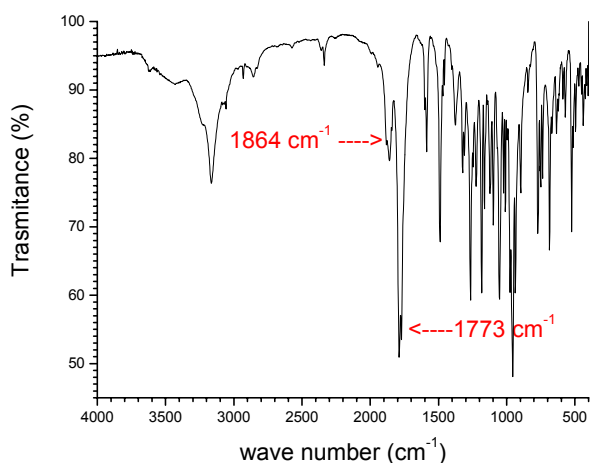triphosgene was used in 50% excess in comparison to the stoichiometric balance. The reaction time is approximately 2 hours and at the end of this time the rest of *O*-diphenylphospho-*L*-serine hydrochloride (**12**), which did not react, was filtered off. To get the pure *O*-diphenylphospho-*L*-serine NCA (**13**) three fold recrystallization was used. The composition of resulting NCA can be confirmed by IR spectroscopy, the melting point measurement and the elemental analysis. The bands in IR spectrum indicating NCA ring formation are at approximately 1864 cm^{-1} and 1773 cm^{-1} (C=O bond vibration of cyclic anhydride) (Figure 4.1-5).

4.2   Synthesis of PEG-*b*-polypeptide block copolymers

4.2.1 PEG-b-poly(L-aspartic acid 4-benzyl esters) (15a, b) and PEG-b-poly(L-glutamic acid 5-benzyl esters) (15c - g)
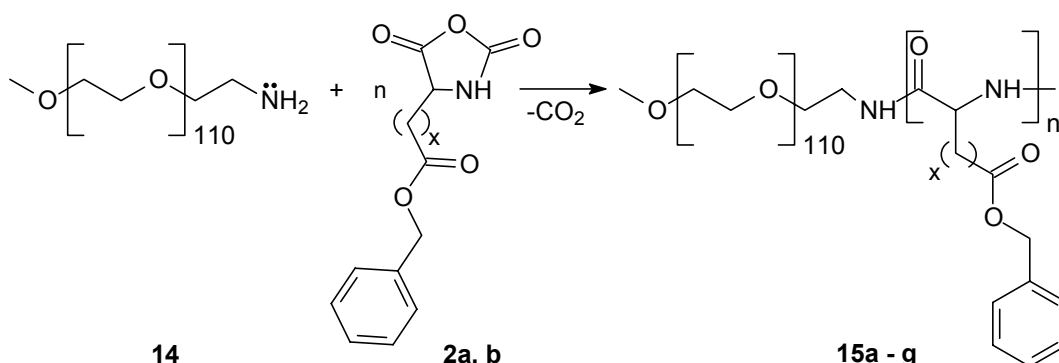
Scheme 4.2-1: Synthesis of the PEG-*b*-poly(*L*-aspartic acid 4-benzyl esters) (**15a**, **b**; for x = 1 and n = 10, 16) and PEG-*b*-poly(*L*-glutamic acid 5-benzyl ester) (**15c** – **g**; for x = 2 and n = 6, 10, 16, 20, 25).

The synthesis of the PEG-*b*-poly(*L*-aspartic acid 4-benzyl esters) (**15a, b**) and PEG-*b*-poly(*L*-glutamic acid 5-benzyl esters) (**15c** - **g**) block copolymers is based on the polymerisation of the NCA's of *L*-aspartic acid 4-benzyl ester (**2a**) and *L*-glutamic acid 5-benzyl ester (**2b**) by α-methoxy-ω-amino[poly(ethylene glycol)] (PEG-NH$_2$) (**14**) as a macroinitiator in DMF as a solvent (Scheme 4.2-1) [62 - 73]. The primary amine at the chain end of PEG attacks exclusively the carbonyl carbon (C-5) of the NCA ring to initiate the polymerisation. As primary aliphatic amines are more nucleophilic than

the active chain ends, initiation is faster than propagation. Consequently, all initiator molecules (PEG-NH$_2$) should be incorporated into the growing peptide chain to obtain a block copolymer of PEG and protected poly(amino acid). The whole reaction has to be done under argon protective gas, because of the sensitivity of the NCA to atmospheric moisture or water that is inadvertently introduced into the monomer during the reaction.
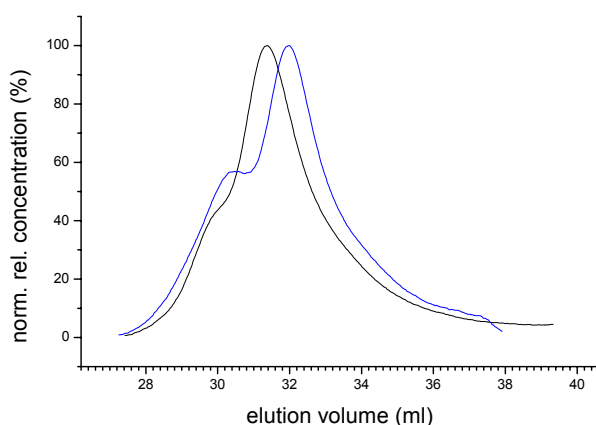

Figure 4.2-1: ⎯ GPC spectra of PEG-*b*-poly(*L*-aspartic acid 4-benzyl ester) (**15a**) RI detector; ⎯ PEG-NH$_2$ M$_n$ = 5000 g/mol.
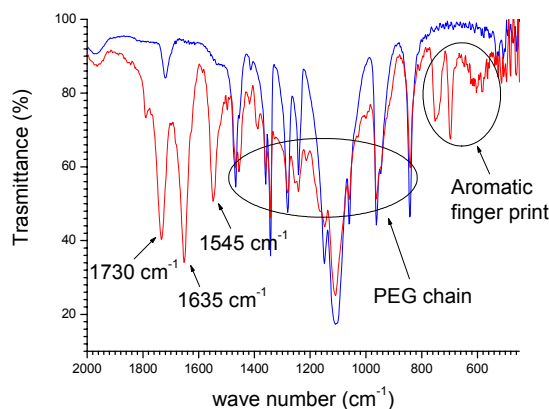
Figure 4.2-2: ⎯ IR spectrum of PEG-*b*-poly(*L*-glutamic acid 5-benzyl ester) (**15d**), ⎯ PEG-NH$_2$ M$_n$ = 5000 g/mol.

The crude block copolymers were analysed by gel-permeation chromatography (GPC) in DMA using RI detector. Figure 4.2-1 shows an example of a GPC chromatogram of the PEG-*b*-poly(*L*-aspartic acid 4-benzyl ester) (**15a**). There is a shift to the higher molecular weight compared to the GPC chromatogram of the PEG-NH$_2$ macroinitiator, which was used for that reaction, indicating the formation of the polypeptide block. The PEG-NH$_2$ elugram has a shoulder, which indicates some impurity (2,1% according to the Gaussian fit). The PEG-NH$_2$ is the commercially available polymer. The most probable way of the polymer formation is by the synthesis of the α-methoxy[poly(ethylene glycol)] with the thionyl bromide in the presence of the triethyl amine (TEA). Subsequently, the intermediate product α-methoxy-ω-bromo[poly(ethylene glycol)] is treated with the ammonia solution in the methanol (Scheme 4.2-2) [74]. The first step has to be done under moisture-free conditions, because thionyl bromide can react with water and hydrolyses to the HBr and SO$_2$. It is well known that HBr can cleave an ether bond. Thus it is possible

shorter poly(ethylene glycol) chains are in the reaction mixture, which are more reactive and can react in the second step with the longer chain to produce a secondary amine with a higher molar mass than the primary amine. This side product does not react with the NCA and cannot be removed by recrystallization. This is a possible explanation of the shoulder on the PEG-NH$_2$ GPC elugram. The same shoulder is seen on the block copolymer GPC elugram with the same elution volume meaning its molar mass has not changed during the polymerisation. The amount of an impurity is constant around 2% according to the Gaussian fit, thus its influence on a subsequent mineralization process is constant but not strong because there are no reactive groups in the impurity molecule.
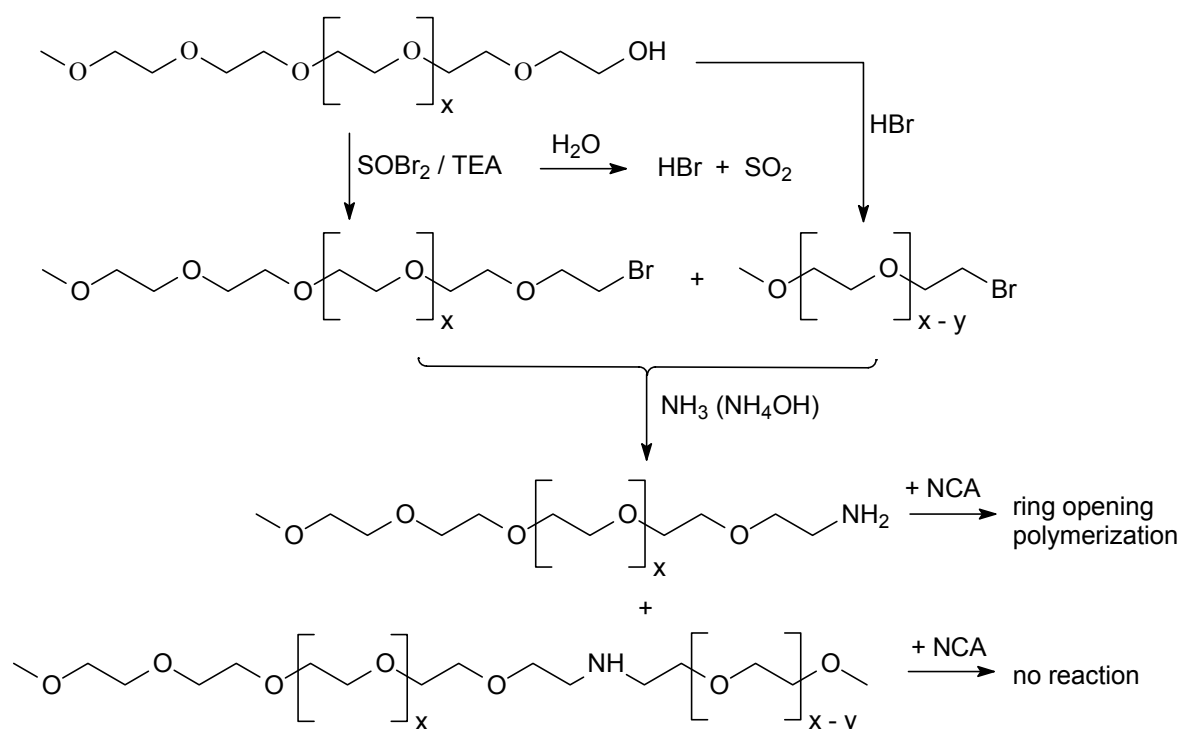
Scheme 4.2-2: The preparation of the PEG-NH$_2$ (**14**).

By IR spectroscopy the amide bond could be identified by two bands, amide I at 1653 cm^{-1} (C=O vibration) and amide II at 1549 cm^{-1} (N-H and C-N vibration). In Figure 4.2-2 the IR spectrum of the PEG-*b*-poly(*L*-glutamic acid 5-benzyl ester) (**15d**) and the PEG-NH$_2$ (**14**), which was used as a macroinitiator, are shown. There are bands at 1730 cm^{-1} (C=O of an ester bond from an amino acid), 1635 cm^{-1} (amide I), 1545 cm^{-1} (amide II), 1470 – 850 cm^{-1} (PEG chain, both spectra are same in this region) and 750 – 580 cm^{-1} (benzyl group from an amino acid, "finger print"). However, the

amide bond is identified, the IR spectrum does not verify if the prepared compound is a block copolymer or just a mixture of two homopolymers. The lacking signal for the macroinitiator in the GPC elugrams of the block copolymers, however, shows indeed a block copolymer was synthesized.
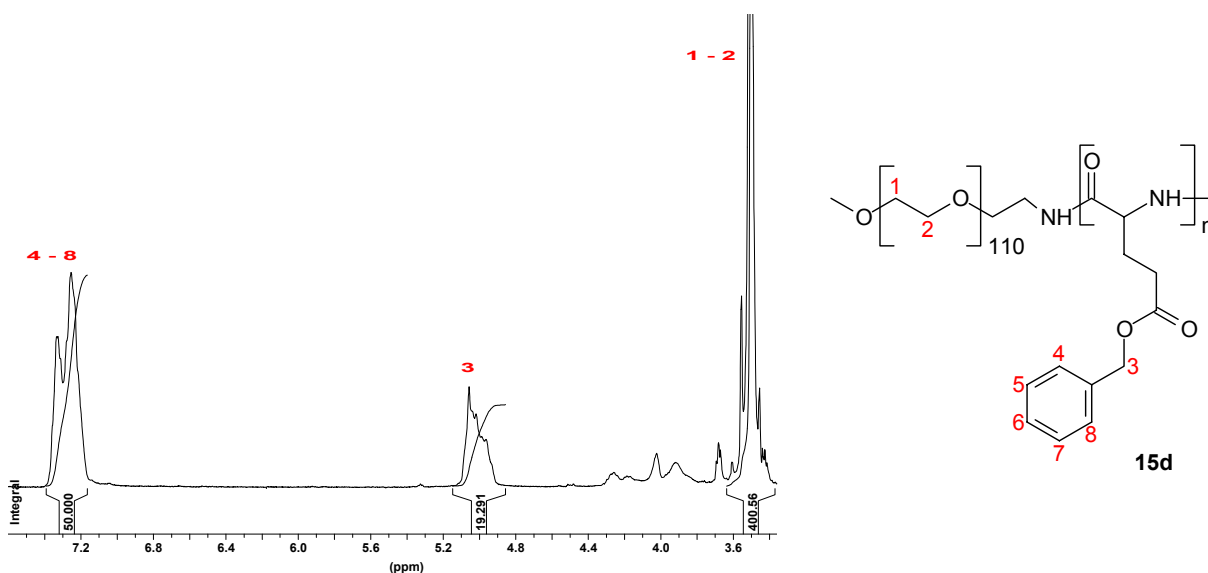

Figure 4.2-3: ^{1}H NMR of PEG-*b*-poly(*L*-glutamic acid 5-benzyl ester) (**15d**)

Figure 4.2-3 shows ^{1}H NMR spectrum of PEG-*b*-poly(*L*-glutamic acid 5-benzyl ester) (**15d**). There is a peak of PEG chain at δ = 3,5 ppm and two peaks of benzyl group at δ = 5,1 ppm (hydrogens from CH_2 group of the benzyl group) and δ = 7,3 ppm (aromatic hydrogens). From the integrals ration between PEG and benzyl group the number of the amino acid units can be calculated.

Table 4.2-1 shows the synthesized polymers. The numbers of the amino acid units in a block of poly(amino acid) were calculated from the signal intensity ratio of the PEG methylene protons (OCH_2CH_2; δ = 3,5 ppm) and benzyl protons of the protecting group ($C_6\underline{H}_5$-CH_2; δ = 7,3 ppm and C_6H_5-$C\underline{H}_2$; δ = 5,05 ppm) in the ^{1}H NMR spectrum in DMSO – d_6. The results from ^{1}H NMR spectroscopy correspond to the macroinitiator / monomer ration and it can be used for the calculation of the peptide block molar mass. Other method for a molar mass measurement is GPC. There are differences in the molar masses measured by ^{1}H NMR and GPC; this could be due to the sample column interactions. The shorter peptide blocks interact less and their molar masses are close to the calculated one from ^{1}H NMR, with increasing the block

length the difference is higher. The PEG standards calibration cannot be used because of the sample column interaction [53, 75], thus the GPC method is used to detect the shift in elution volumes between macroinitiator and block copolymers and to check other impurities (as a homopolymers). The polymers prepared by a living polymerisation should not be very polydispersed (polydispersity $PD = \overline{M}_w/\overline{M}_n$), for an example Kataoka et al [69] in their work have polymers with PD around 1,09. In case of these polymers in Table 4.2-1 the polydispersity from GPC is quite high, because of the already polydisperse macroinitiator PEG-NH$_2$.

Table 4.2-1: List of prepared polymers and results of GPC measurement.

15	x	n[a]	PD[b]	PD[c]	$M_{n(block\ PAA)}$[d]	$M_{n(block\ PAA)}$[e]
a	1	10	1,40	1,45	1960	2050
b	1	16	1,50	1,60	2900	3280
c	2	6	1,60	1,65	1280	1314
d	2	10	1,45	1,50	1890	2190
e	2	16	1,70	1,80	2800	3504
f	2	20	1,60	1,67	3620	4380
g	2	25	1,70	1,80	4230	5475

a   from ^{1}H NMR
b   of macroinitiator PEG-NH$_2$ (GPC in DMA)
c   of block copolymer polymer (GPC in DMA)
d   from GPC in DMA
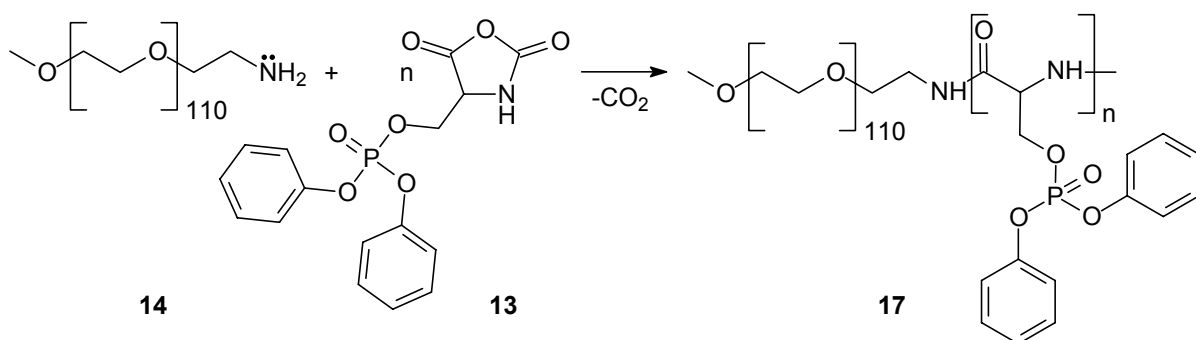e   from ^{1}H NMR

4.2.2 Synthesis of PEG-b-poly(O-benzyl-L-serine) (*16*) and PEG-b-poly(O-diphenylphospho-L-serine) (*17*)
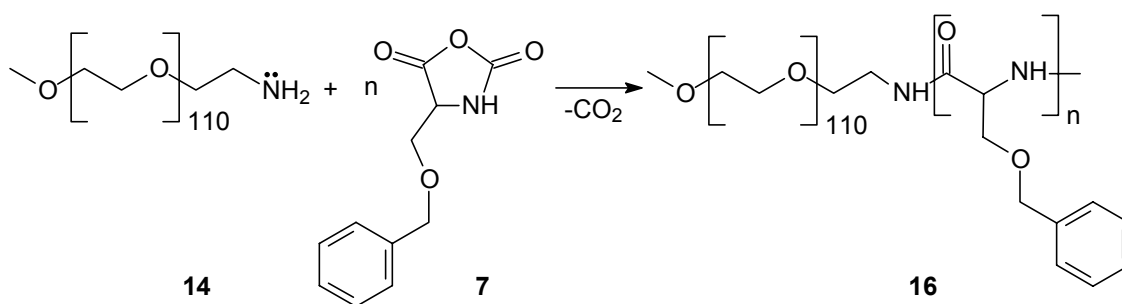
Scheme 4.2-3: Synthesis of PEG-*b*-poly(*O*-benzyl-*L*-serine) (**16**).

The synthesis of the PEG-*b*-poly(*O*-benzyl-*L*-serine) (**16**) (Scheme 4.2-3) and PEG-*b*-poly(*O*-diphenylphospho-*L*-serine) (**17**) (Scheme 4.2-4) were carried out in analogy to the synthesis of PEG-*b*-poly(*L*-aspartic acid 4-benzyl esters) (**15a, b**) and PEG-*b*-poly(*L*-glutamic acid 5-benzyl esters) (**15c** - **g**). It is based on polymerisation of the NCA of *O*-benzyl-*L*-serine and NCA (**7**) of *O*-diphenylphospho-*L*-serine (**13**) by the α-methoxy-ω-amino[poly(ethylene glycol)] (PEG-NH$_2$) (**14**) chain as macroinitiator in dry dioxane as a solvent (Scheme 4.2-4). The primary amine at the chain end of the PEG-NH$_2$ (**14**) attacks exclusively the carbonyl carbon (C-5) of the NCA ring to initiate the polymerisation. The whole reaction has to be done under argon protective gas, because of the sensitivity of the NCA to atmospheric moisture or water that is inadvertently introduced into the monomer during the reaction.

Scheme 4.2-4: Synthesis of PEG-*b*-poly(*O*-diphenylphospho-*L*-serine) (**17**).

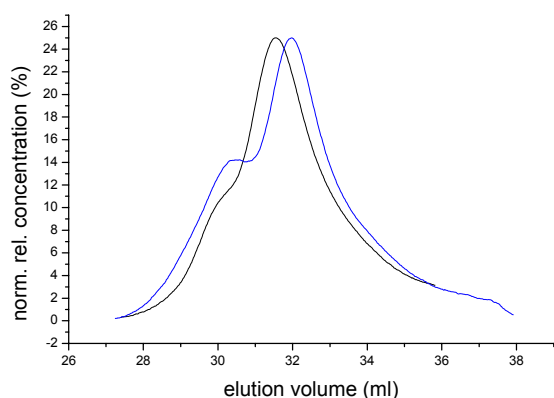**Figure 4.2-4:** ⎯ GPC elugram of PEG-*b*-poly(*O*-diphenylphospho-L-serine) (**17**) RI detector; ⎯ PEG-NH$_2$ M$_w$ = 5000 g/mol.

Figure 4.2-5: ⎯ GPC elugram of PEG-*b*-poly(*O*-Benzyl-L-serine) (**16**) RI detector; ⎯ PEG-NH$_2$ M$_w$ = 5000 g/mol.

The block copolymers were analysed by gel-permeation chromatography (GPC) in DMA. Figures 4.2-4 and 4.2-5 show examples of the GPC elugrams of the PEG-*b*-poly(*O*-benzyl-*L*-serine) (**16**) and the PEG-*b*-poly(*O*-diphenylphospho-*L*-serine) (**17**), there is a shift to higher molecular weight compared to the GPC elugram of the PEG-NH$_2$ (**14**) macroinitiator, which was used for that reaction. In both cases the elugrams have shoulders at the same elution volume, meaning the PEG-NH$_2$ macroinitiator contains the unreactive impurity (around 2 % according to the Gaussian fit) as it is described in the previous chapter 4.2-1.

By the IR spectroscopy could be an amide bond identified, in case of the PEG-*b*-poly(*O*-benzyl-*L*-serine) (**16**) there are two bands; amide I at 1632 cm^{-1} and amide II at 1530 cm^{-1} and in case of the PEG-*b*-poly(*O*-diphenylphospho-*L*-serine) (**17**) there are two bands; amide I at 1667 cm^{-1} and amide II at 1542 cm^{-1}.
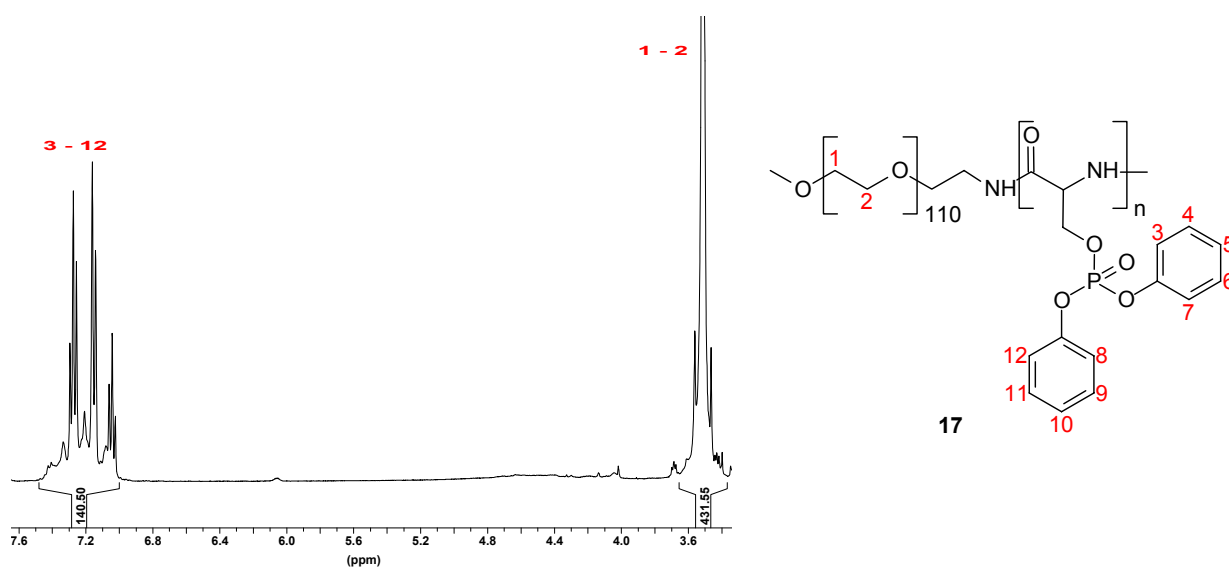
Figure 4.2-6: ^{1}H NMR PEG-*b*-poly(*O*-diphenylphospho-*L*-serine) (**17**).

Table 4.2-2 shows the polymers that were synthesized. The numbers of amino acid units in a poly(amino acid) block were calculated from the signal intensity ratio of methylene protons of the PEG (OCH$_2$CH$_2$; δ = 3,5 ppm) and benzyl protons of the protecting group (C$_6$H$_5$-CH$_2$; δ = 7,25 ppm and C$_6$H$_5$-CH$_2$; δ = 4,40 ppm) or phenyl protecting group (C$_6$H$_5$; δ = 7,04 - 7,33 ppm), respectively. In Figure 4.2-6 an example of the ^{1}H NMR of the PEG-*b*-poly(*O*-diphenylphospho-*L*-serine) (**17**) is

shown. The numbers of amino acids units calculated from the ^{1}H NMR correspond to the used ration macroinitiator / monomer. The molar mass of PEG-*b*-poly(*O*-benzyl-*L*-serine) (**16**) calculated from ^{1}H NMR is close (slightly higher) to the one obtained from the GPC measurement (the sample column interactions are not so strong). In contrast to it, there is a difference between the molar masses of the PEG-*b*-poly(*O*-diphenylphospho-*L*-serine) (**17**) obtained from the ^{1}H NMR and the GPC measurements. The analysis of the molar mass distribution of double hydrophilic block copolymers by GPC is very difficult as already indicated in ref. [53, 75]. Interaction of the functional polymer groups with the column material leads to a retardation of the polymer with respect to its corresponding hydrodynamic volume and thus to apparently too low molar mass. This tendency correlated with the number of functional groups as in case of the previously described poly(ethylene glycol)-*b*-poly(ethyleneimine) modified by COOH, PO_3H_2 or SO_3H functional groups [53, 75]. Further complications arise from the introduction of hydrophobic moieties (benzyl or phenyl protecting groups) into the double hydrophilic block copolymer, which also can interact with the column material. Furthermore, the requirements include that the polymers must be molecularly soluble. Facing these difficulties it is not surprising that a successful characterization of the synthesized block copolymers by GPC could not be achieved in this study. In the very few cases where a realistic molar mass based on calibration with PEG standards could be obtained, a laborious optimisation of the set-up for every single block copolymer was necessary.

The polydispersity from GPC is quite high, because of the already polydisperse macroinitiator PEG-NH_2 (**14**).

Table 4.2-2: List of prepared polymers and results of GPC measurement.

	n^a	PD^b	PD^c	$M_{n(block\ PAA)}{}^d$	$M_{n(block\ PAA)}{}^e$
16	10	1,40	1,50	1700	1770
17	14	1,60	1,70	3500	4452

a   from ^{1}H NMR
b   of macroinitiator PEG-NH_2 (GPC in DMA)
c   of block copolymer polymer (GPC in DMA)
d   g/mol from GPC in DMA
e   g/mol from ^{1}H NMR

4.3   Deprotection of the functional group

The last step of the whole synthesis procedure is the cleavage of the protecting group to get the active block copolymer for the mineralization experiments. A benzyl group (ester bond) in case of the PEG-*b*-poly(*L*-aspartic acid 4-benzyl ester) (**15a**, **b**) and the PEG-*b*-poly(*L*-glutamic acid 5-benzyl ester) (**15c** - **g**), a benzyl (ether bond) in case of PEG-*b*-poly(*O*-benzyl-*L*-serine) (**16**) and a phenyl group (ester bond) in case of PEG-*b*-poly(*O*-diphenylphospho-*L*-serine) (**17**) were used as protecting groups.

There are several possibilities for the deprotection of the functional group, for example hydrolysis or hydrogenation on different catalysts [76,77].

4.3.1 *PEG-b-poly(L-aspartic acids) (18a, b) and PEG-b-poly(L-glutamic acids) (18c - g)*
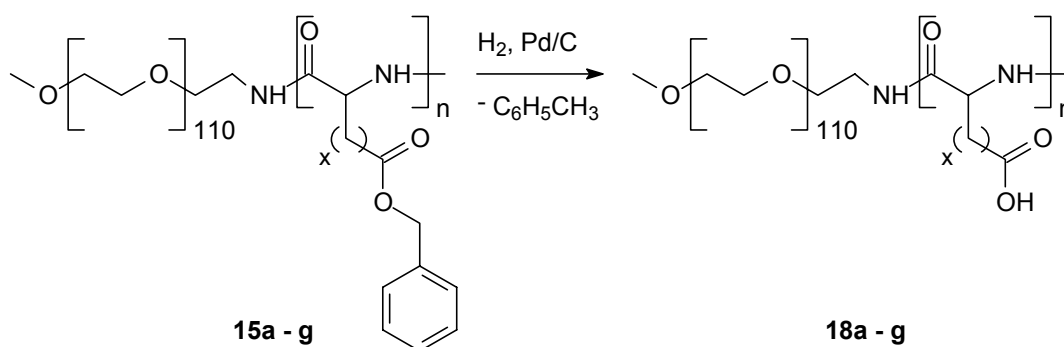
Scheme 4.3-1: Deprotection reaction of the benzyl group in PEG-*b*-poly(*L*-aspartic acid 4-benzyl esters) (**15a, b**; x = 1 and n = 10, 16) and PEG-*b*-poly(*L*-glutamic acid 5-benzyl esters) (**15c** – **g**; x = 2 and n = 6, 10, 16, 20, 25).

Alkaline hydrolyses can be done by NaOH or KOH solution in a mixture of water : methanol : propan-2-ol (1 : 2 : 2 by volume) at approximately 0 °C. The disadvantage of this method is a possible racemization as well as intramolecular isomerization of the amino acid units of the aspartic and the glutamic acid. A better method is hydrogenation (Scheme 4.3-1), which is carried out in a mixture of THF and methanol (1:1 by volume) in the presence of palladium on activated carbon (10%

Pd) as a catalyst at room temperature. Hydrogen gas is introduced and maintained in the system by means of a balloon reservoir. The completion of the hydrogenation could be confirmed by ^{1}H NMR spectroscopy. The signals of the benzyl group at $\approx$ 7,30 ppm and 5,05 ppm in the ^{1}H NMR spectrum disappear, indicating a quantitative deprotection reaction. This could be confirmed by IR spectroscopy. No adsorption of the benzyl group in the finger print area was found anymore.
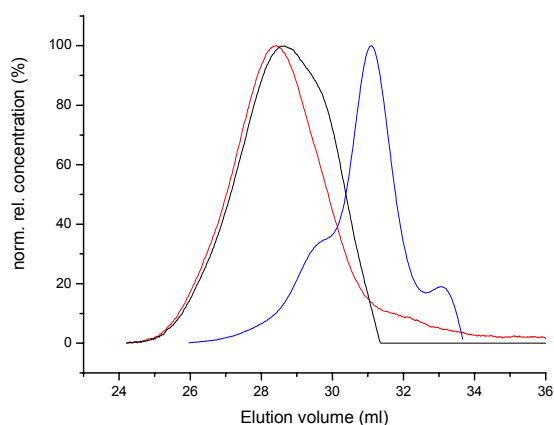

Figure 4.3-1: —— GPC spectra of PEG-*b*-poly(*L*-glutamic acid) (**18f**) RI detector; —— UV-VIS detector λ = 210 nm; —— PEG-NH$_2$ M$_n$ = 5000 g/mol.

Figure 4.3-1 shows the GPC elugram of PEG-*b*-poly(*L*-glutamic acid) (**18f**) measured in acetate puffer pH =7. The elugram of the macroinitiator has shoulder, which is due to the impurity (for more details see chapter 4.2-1). For polymer sample two types of detectors were used. The first RI detector shows shoulder by the same elution volume as in case of the macroinitiator impurity. The second UV-VIS detector at λ = 210 nm shows only polymer which contains a peptide bond, meaning the block copolymer.

Table 4.3-1 shows, M$_n$ of the polypeptide block and the polydispersity (PD). Both numbers are from GPC measurements in acetate puffer pH = 7. The molar mass is not correct because of the sample column interaction, thus the PEG standard calibration cannot be used [53, 75]. At least the GPC measurement proves if the sample contains homo- or block copolymer. The ^{1}H NMR spectroscopy is used to calculate the number of the amino acid units and correct peptide block molar mass. There is difference between the polydispersity of the macroinitiator and the block copolymer. The macroinitiator contains some impurity with higher molecular weight and it is quite polydisperse. The polydispersity of the block copolymer is lower because of the purification by dialyses (MWCO 1000) and consequent lyophilisation.

Table 4.3-1: List of prepared polymers and results of GPC measurement.

18	x	n^a	PD^b	PD^c	$M_{n(block\ PAA)}{}^d$	$M_{n(block\ PAA)}{}^e$
a	1	10	1,40	1,30	1000	1160
b	1	16	1,45	1,40	1490	1856
c	2	6	1,55	1,40	700	774
d	2	10	1,45	1,35	1050	1290
e	2	16	1,65	1,45	1680	2064
f	2	20	1,50	1,40	2010	2580
g	2	25	1,60	1,40	2600	3225

a   from ^{1}H NMR
b   of macroinitiator PEG-NH$_2$ (GPC in acetate puffer pH = 7)
c   of block copolymer polymer (GPC in acetate puffer pH = 7)
d   g/mol from GPC in acetate puffer pH = 7
e   g/mol from ^{1}H NMR
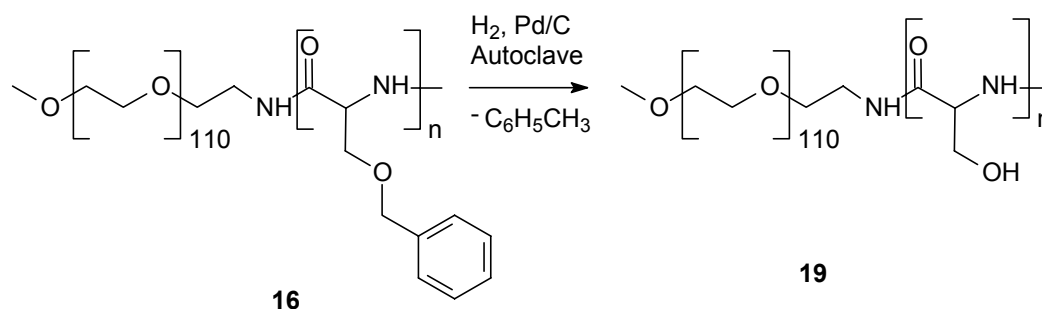
4.3.2 PEG-b-poly(L-serine) (19) and PEG-b-poly(O-phospho-L-serine) (20)

The cleavage of the benzyl group in case of the PEG-*b*-poly(*O*-benzyl-*L*-serine) (**16**) is slightly more complicated, than in case of the PEG-*b*-poly(*L*-aspartic acids) (**18a**, **b**) and PEG-*b*-poly(*L*-glutamic acids) (**18c** - **g**), because of the ether bond between serine and the protecting group. If a hydrogenation is applied as in case of the glutamic and the aspartic acid, there are still some benzyl groups left in the block copolymer after that reaction, as the ether bond is stronger than the ester bond.

Therefore, more harsh conditions like hydrolysis have to be applied. The hydrolysis is carried out in cold dioxane previously saturated with dry bromine-free hydrogen bromide at 2 - 4 °C overnight [56]. This debenzylation procedure, however, caused a slight degradation of the polypeptide backbone as traced by NMR spectroscopy. This degradation is not acceptable; therefore hydrogenation at high pressure was tried in a mixture of THF and methanol as a solvent and palladium on activated carbon as a catalyst. The whole reaction (Scheme 4.3-2) is carried out in an autoclave at high hydrogen pressure p = 3.10^6 Pa (30 bar) and at 55 °C. Higher temperatures lead to degradation of the polyserine, which is not thermodynamically stable [78]. Quantitative debenzylation by the above procedure could be proven by the absence

of benzyl groups in the ^{1}H NMR spectrum (no signal at 7,25 ppm and 4,04 ppm) and by IR spectroscopy.

Scheme 4.3-2: Deprotection reaction of the benzyl group in PEG-*b*-poly(*O*-benzyl-*L*-serine) (**16**).
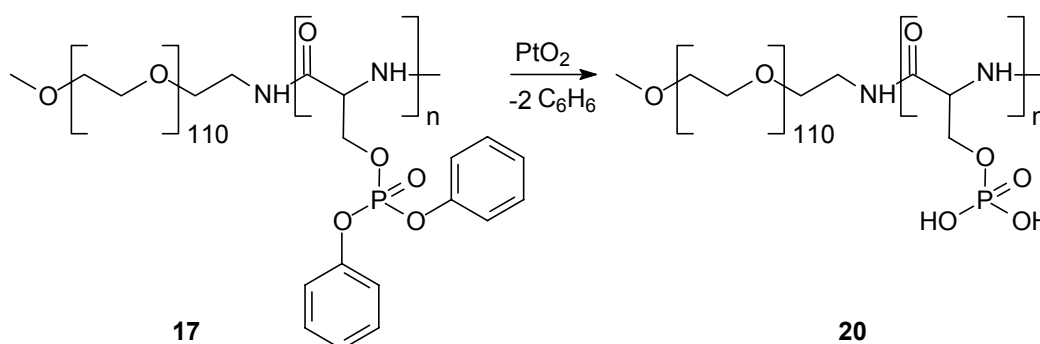
Scheme 4.3-3: Deprotection reaction of the phenyl groups in the PEG-*b*-poly(*O*-diphenylphospho-*L*-serine) (**17**) to PEG-*b*-poly(*O*-phospho-*L*-serine) (**20**).

The deprotection of the two phenyl groups in the PEG-*b*-poly(*O*-diphenylphospho-*L*-serine) (**17**) can be done by a hydrogenation reaction on platinum oxide (IV) in a mixture of trifluoroacetic acid and acetic acid (1:1 by volume) at room temperature (Scheme 4.3-3). The complete removal of the phosphate protecting phenyl groups from the side chain can be proven by the ^{1}H NMR spectroscopy, or by UV-VIS spectroscopy, or by IR spectroscopy. There are no aromatic signals at 7,04 - 7,33 ppm in ^{1}H NMR, no UV absorption at 260 nm and no absorption of phenyl groups in the finger print area. The degree of phosphorylation corresponds to the monomer degree 98%. There are already some works done on the polymer phosphorylation, but it is not easy to quantitatively phosphorylated polymers, normally the degree is max. 50% [79 - 81]. Thus, it is a good way, first to prepare 100% phosphorylated monomer and consequently it polymerises.
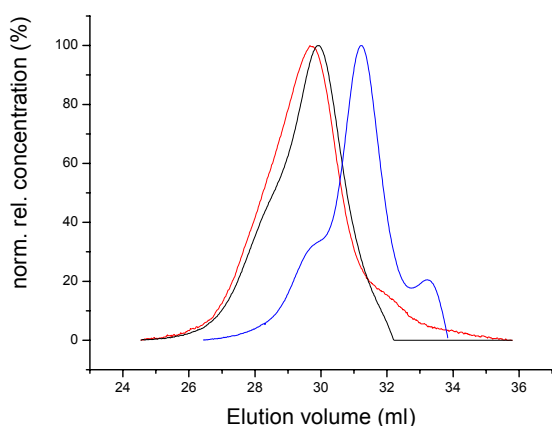
Figure 4.3-2: ⎯ GPC spectra of PEG-*b*-poly(*O*-phosphoserine) (**20**) RI detector; ⎯ UV-VIS detector at λ = 210 nm; ⎯ PEG-NH$_2$ M$_n$ = 5000 g/mol.

Figure 4.3-2 shows the GPC elugrams of PEG-*b*-poly(*O*-phosphoserine) (**20**) and the macroinitiator measured in acetate puffer pH =7. The macroinitiator elugram has the shoulder as in the previous cases (for more details see chapter 4.2-1). For polymer sample two types of detectors were used, the RI detector and the UV-VIS detector at λ = 210 nm, which shows only polymer which contains a peptide bond, meaning the block copolymer.

Table 4.3-2: List of prepared polymers.

	n[a]	PD[b]	PD[c]	M$_{n(block\ PAA)}$[d]	M$_{n(block\ PAA)}$[e]
19	10	1,40	1,35	750	870
20	14	1,50	1,40	1500	2324

a   from ^{1}H NMR spectroscopy
b   of macroinitiator PEG-NH$_2$ (GPC in acetate puffer pH = 7)
c   of block copolymer polymer (GPC in acetate puffer pH = 7)
d   g/mol from GPC in acetate puffer pH = 7
e   g/mol from ^{1}H NMR

Table 4.3-2 shows M$_n$ and PD of the prepared block copolymers. GPC is done in acetate puffer pH = 7. The molar mass is not correct because of the sample column interaction [53, 75]. The ^{1}H NMR spectroscopy is used to calculate the number of the amino acid units and correct peptide block molar mass. There is a difference between the polydispersity of the macroinitiator and the block copolymer. The macroinitiator contains some impurity with higher molecular weight and it is quite polydisperse. The polydispersity of the block copolymer is lower because of the purification by dialyses (MWCO 1000) and consecutive lyophilisation.

4.4   Secondary structure of block copolymer

The secondary structures of the prepared block copolymers PEG-*b*-poly(*L*-aspartic acid) (**18a**, **b**) and PEG-*b*-poly(*L*-glutamic acid) (**18c** - **g**) were examined in aqueous solutions by circular dichroism (CD) spectroscopy [82, 83]. There are three known main types of secondary structures: α-helix, β-sheet and random coil. The occurrence of all of them depends on the used measurement conditions (pH, temperature).

First of all, the polypeptide block length is important for the secondary structure. A peptide chain at least containing 10 amino acids is necessary to exhibit a secondary structure in the CD spectrum. The block copolymers PEG-*b*-poly(*L*-glutamic acid) (**18d** - **g**) with a longer amino acid block show a spectrum of an α-helix (95% of an α-helix and 5% of random coil, due to the polydispersity of block copolymer, calculated according to the literature [98]) at room temperature and at pH $\approx$ 4 with two minima at λ = 209 nm and λ = 222 nm (Figure 4.4-1). Copolymers PEG-*b*-poly(*L*-aspartic acid) (**18a**, **b**) show most probably a mixture of random coil structures (80%) and an α-helix (20%, calculated according to the literature [98]) at pH = 4, the curve has a minimum at λ = 219 nm and at λ = 197 (Figure 4.4-2). It is described in literature [84] that polyglutamic acid (n = 32) monolayers exhibit in CD spectrum partly the β-sheet structure with a minimum at λ = 220 nm at the same conditions.
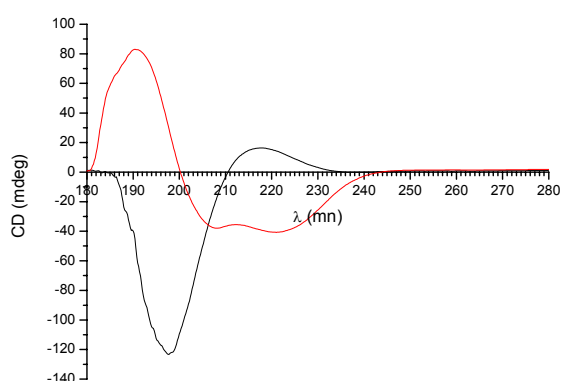

Figure 4.4-1: CD spectrum of the PEG-*b*-poly(*L*-glutamic acid) (**18e**), — at pH = 4 and — at pH = 8.
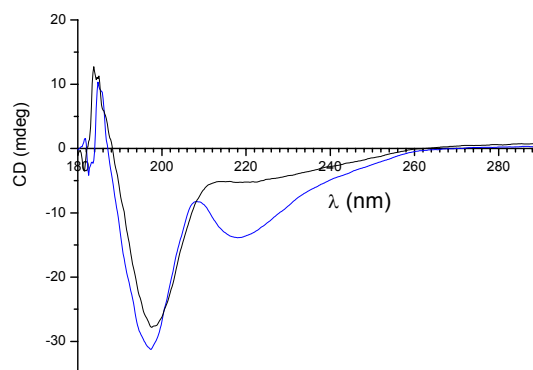
Figure 4.4-2: CD spectrum of the PEG-*b*-poly(*L*-aspartic acid) (**18b**), — at pH = 4 and — at pH = 8.

Other series of measurement were done at different pH condition at room temperature. For each block copolymer a number of samples was prepared at different pH, and the CD spectra were measured. For example, in Figure 4.4-1, PEG-*b*-poly(*L*-glutamic acid) (**18d** - **g**) form an α-helix (90 - 95% of an α-helix and 5 - 10% of random coil, calculated according to the literature [98]) at pH ≈ 4 and a random coil (100%) at pH ≈ 8. In between, a mixture of both structures was found.
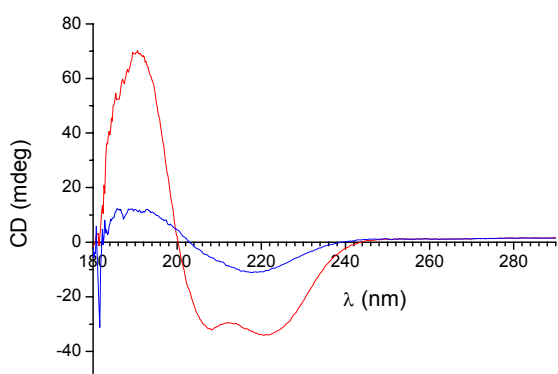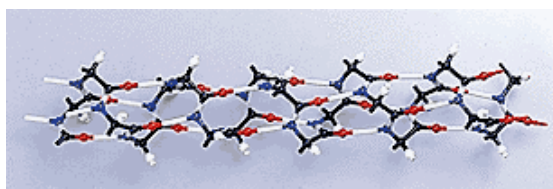

Figure 4.4-3: CD spectra of PEG-*b*-poly(*L*-glutamic acid) (**18e**) at pH = 4; — T = 25 °C and — T = 60 °C.
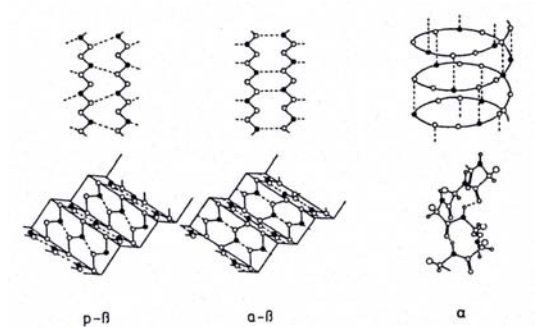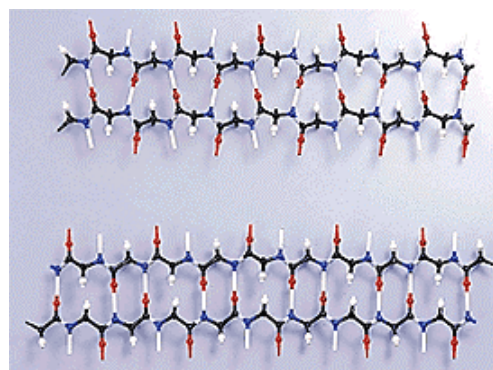
a)

b)

Figure 4.4-4: a) Model of α-helix (20amino acid backbone), **b)** Models of *p*-β-sheets = parallel and *a*-β-sheets = anti-parallel (10 amino acid backbone).

61

Figure 4.4-4a shows a model of an α-helix secondary structures, which is created by intramolecular hydrogen bonds. The pleated β-sheet structure, parallel and anti-parallel, in Figure 4.4-4b, may be intermolecular between two chains as well as intramolecular between segments of the same chain.

Another measurement was carried out at different temperature and at pH 4. A sample of PEG-*b*-poly(*L*-glutamic acid) (**18e**) with 15 units of amino acid was measured at room temperature and subsequently the same sample at 60°C (Figure 4.5-3). There are some differences in both spectra. At room temperature the block copolymer has the structure of an α-helix (95% of an α-helix and 5% of random coil, calculated according to the literature [98]), the spectrum has two minima at λ = 209 nm and λ = 222 nm, but at 60°C a β-sheet structure is indicated (95% of an α-helix and 5% of random coil, calculated according to the literature [98]), the spectrum has one minimum at λ = 219 nm. A reference measurement with a polyglutamic acid homopolymers (of the same block length) was done, but yielded an α-helix at both temperatures. Most probably the PEG chain has influence on a structure of the block copolymer. In a literature [85] an example of PEG influence on a secondary structure of polylysine block is known. The differences between the CD spectrum of PEG-*b*-poly(*L*-lysine) (n = 19) and the spectrum of homopoly(*L*-lysine) with the same block length as the polylysine block in the block copolymer is significant. The block copolymer CD spectrum shows an α-helix at pH > 11 and a random coil at pH < 5,3. In between it shows a mixture of both structures. But homopolymers having a molecular weight similar to that of the block copolymer form no α-helix structure, but its structure remains a random coil over the measured pH range, indicating the essential role of the poly(ethylene glycol) conjugation for the induction of a helix – coil transition. At a higher pH the α-helix structure is stabilized via hydrogen bonds, the polylysine block has -NH$_2$ functional group in a side chain. The -NH$_2$ functional group is not protonated at higher pH and can form intramolecular hydrogen bonds as in case of polyglutamic acid at lower pH ~ 4. With decreasing pH to 5 the -NH$_2$ functional group is protonated (-NH$_3^+$) and the block copolymer changes its secondary structure. This corresponds to the polyglutamic acid at higher pH ~ 8 (Figure 4.4-5).
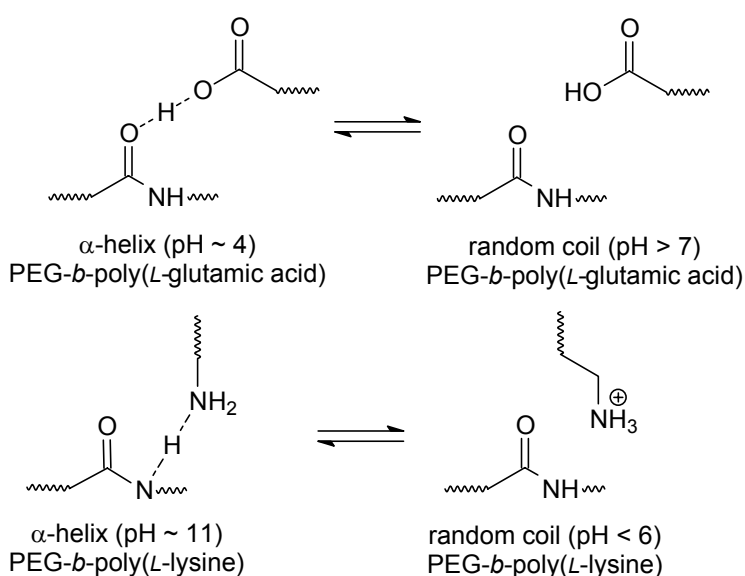
Figure 4.4-5: Intramolecular hydrogen bonds formation at different pH in the polylysine and the polyglutamic acid chains.

α-helix (pH ~ 4)
PEG-*b*-poly(*L*-glutamic acid)

random coil (pH > 7)
PEG-*b*-poly(*L*-glutamic acid)

α-helix (pH ~ 11)
PEG-*b*-poly(*L*-lysine)

random coil (pH < 6)
PEG-*b*-poly(*L*-lysine)
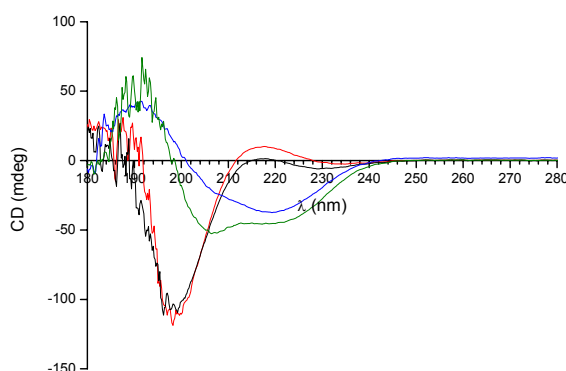
Figure 4.4-6: CD spectra of PEG-*b*-poly(*L*-glutamic acid) (**18e**) in the presence of Ca^{2+} ions at different pH. — at pH = 3,70; — at pH = 4,26; — at pH= 4,57; — at pH = 5,05.
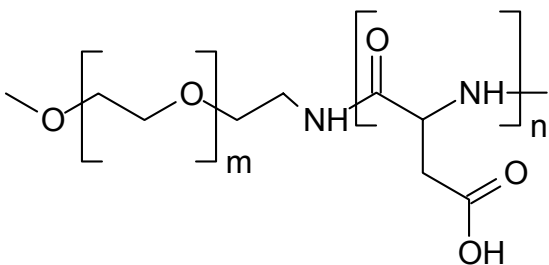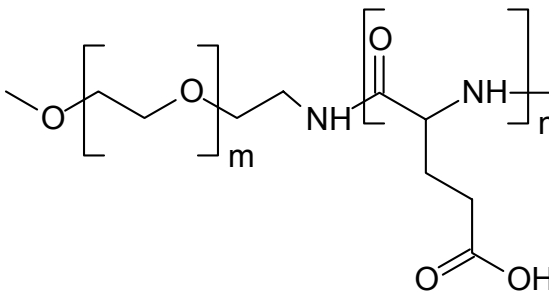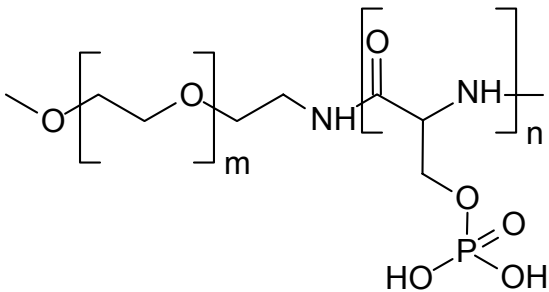
The last step was to prove if Ca^{2+} ions would change the secondary structure of the block copolymer during the mineralization process. A number of samples were prepared at different pH in presence of Ca^{2+} ions (to simulate the mineralization conditions) and the CD spectra were measured. Figure 4.5-6 shows no influence of Ca^{2+} on the secondary structure. The spectra at different pH are the same as those measured at the different pH without Ca^{2+} present, thus the pH has a higher influence on the secondary structures than ions have. This is interesting, because it was reported that ions affect the secondary structure. For example in ref. [86, 82] is presented that sequential oligo- and polypeptides based on glutamic and leucine

residues exhibit a random coil conformation in pure water. Addition of very small amounts of divalent metallic cations induces the formation of ordered structure in the peptides, which remain in solution. Higher salt concentrations precipitate the peptides. Polypeptides with alternating glutamic acid and leucine residues undergo a coil to β-sheet transition in the presence of Ca^{2+}, Ba^{2+}, Mn^{2+}, Co^{2+}, Zn^{2+} and Hg^{2+}. Addition of Cu^{2+} or Fe^{3+} induces the formation of an α-helix.

5   Mineralization with double hydrophilic block copolymers

Double hydrophilic block copolymers are very active in the control of crystal morphologies of calcium carbonate [17, 18, 87], barium sulfate [19, 20], ZnO [88], barium chromate [89], ice [90] and even organic crystals [91]. Those polymers are designed as "molecular tools", where one block interacts strongly with the mineral surface and the other block keeps the "construction site" in solution. In Table 5-1 shows the range of polymers that were used in the mineralization experiments.

Table 5-1: List of prepared polymers

Polymer structure	Name of polymer	Nr of polymer
PEG(m)-*b*-pAsp(n)	PEG(110)-*b*-pAsp(10) PEG(110)-*b*-pAsp(16)	**18a** **18b**
PEG(m)-*b*-pGlu(n)	PEG(110)-*b*-pGlu(6) PEG(110)-*b*-pGlu(10) PEG(110)-*b*-pGlu(16) PEG(110)-*b*-pGlu(20) PEG(110)-*b*-pGlu(25)	**18c** **18d** **18e** **18f** **18g**
PEG(m)-*b*-p(PSer)(n) 98%	PEG(110)-*b*-p(PSer)(14)	**20**

5.1   CaCO$_3$ mineralization

The fast *Double-Jet* and the slow *Kitano* methods were used for the preparation of CaCO$_3$ particles. All polymers mentioned in Table 5-1 were used to modify the morphology and the modification of CaCO$_3$ crystals, depending on the experimental conditions, for example influence of block length, concentration of polymer, time dependence, or different functional groups of the active peptide chain were investigated. Instead of the typical rhombohedral calcite single crystals, vaterite spheres were predominantly obtained. These spheres were superstructures of vaterite nanocrystals (size 10 – 30 nm from WAXS measurement), corresponding to literature results [17, 18, 75]. In case of PEG-*b*-p(PSer) (**20**), dumbbell-like particle were obtained. The resulting CaCO$_3$ particles were characterised by light microscopy in solution and by scanning electron microscopy (SEM) and partly by transmission electron microscopy (TEM), thus allowing the precise characterisation of size and shape. In almost every case, the crystal sizes and shapes observed with optical microscopy (crystals in solution) correspond to those which were observed using SEM. Thus, drying artefacts during sample preparation can be excluded, unless explicitly stated. Wide angle X-ray scattering (WAXS) measurements were used to prove the modification of the CaCO$_3$ particles and the size of the nanoparticles.

5.1.1 Influence of the peptide block length

A polymer PEG-*b*-pGlu (**18c** - **g**) was prepared with different block lengths (Table 5-1). All of them were used for mineralization of CaCO$_3$ by the *Double Jet* and *Kitano* method, and the concentration of polymer in the solution was set to 1g/l. Crystals were checked by light microscopy and SEM.

Figure 5.1-2 shows pictures made by scanning electron microscopy (SEM). It is obvious that the shorter block does not have a strong influence on the mineralization, as the result is a mixture of different particle shapes and the crystals partly show calcite faces. There are obviously not enough functional groups in each template for an efficient interaction with CaCO$_3$. According to the WAXS measurement the crystals consist of calcite and vaterite. After 2 months standing in

their mother solution, pure calcite was found. Hence, the block copolymer did not stabilise vaterite sufficiently, and it transformed to the more stable calcite form. These results correspond to the literature finding [17]. There, the mineralization of $CaCO_3$ was carried out in presence of PEG polymers, which contained only one terminal functional unit (COOH, Asp, EDTA). The crystal size as well as the shape was not well defined. In all cases, bigger crystals and aggregated crystals exceeding 20 mm were obtained. Those crystals were synthetic calcite as shown by WAXS. The vaterite-calcite transformation also agrees with Richter et al reference [97], where vaterite transforms into calcite within 8 h (see Figure 2.1-3a, in chapter 2.1.1).
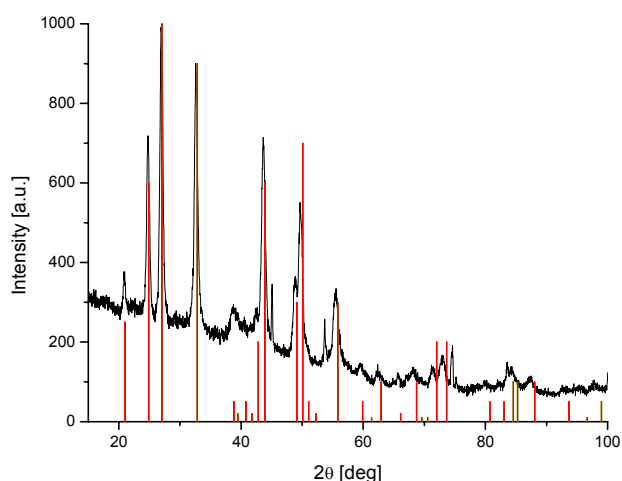
Figure 5.1-1: ⎯⎯ WAXS of $CaCO_3$ in presence of PEG-*b*-pGlu (**18e**, n = 16) after one year time and ⎯⎯ vaterite.

Polymers with a longer peptide block (n > 6) exhibit a trend towards spherical superstructure of vaterite nanocrystals (Figures 5.1-2 b - e). They show a better control of the crystal modification and stabilise the vaterite modification for more than one year (Figure 5.1-1, WAXS measurement). The obtained crystals are spherical and composed of 15 - 20 nm nanoparticles. There is no big influence of the double hydrophilic block copolymers on the nanocrystals size (Table 5.1-1).

a)
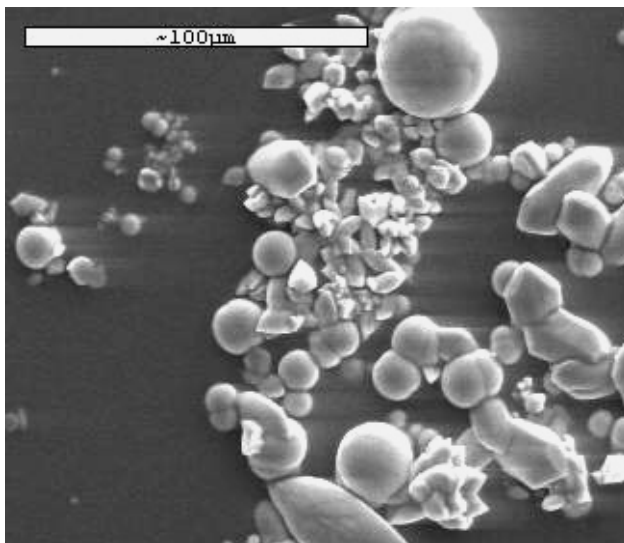
b)
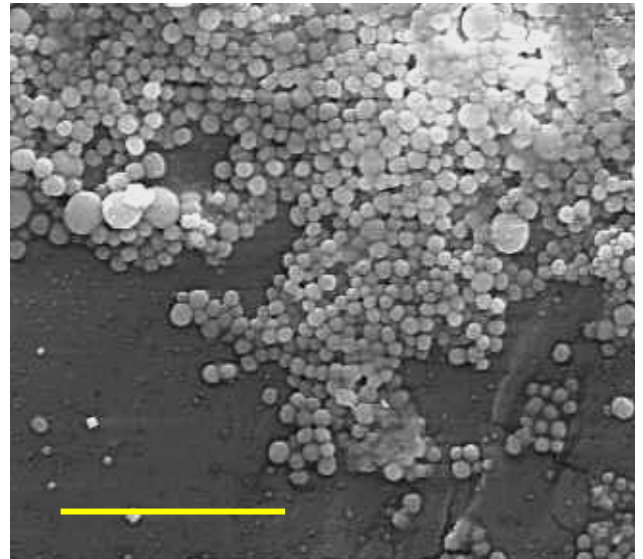
c)
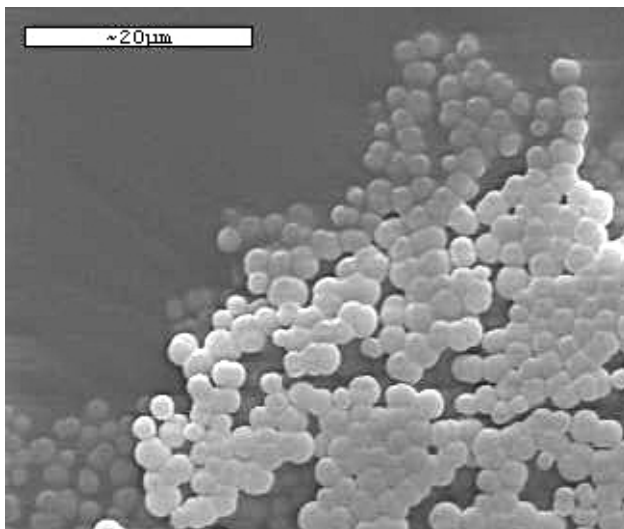
d)
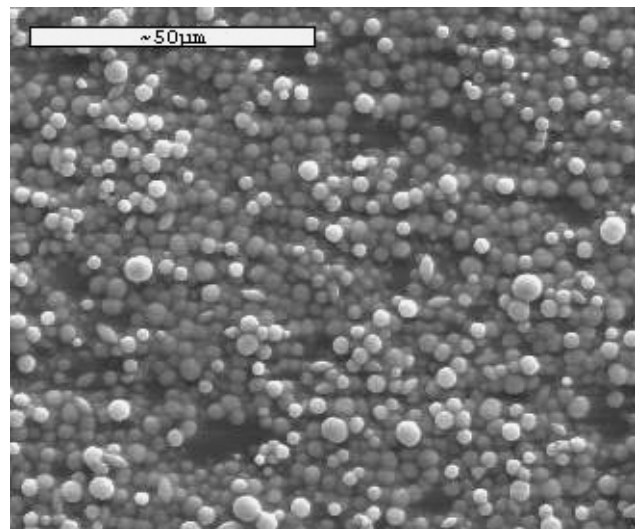
e)
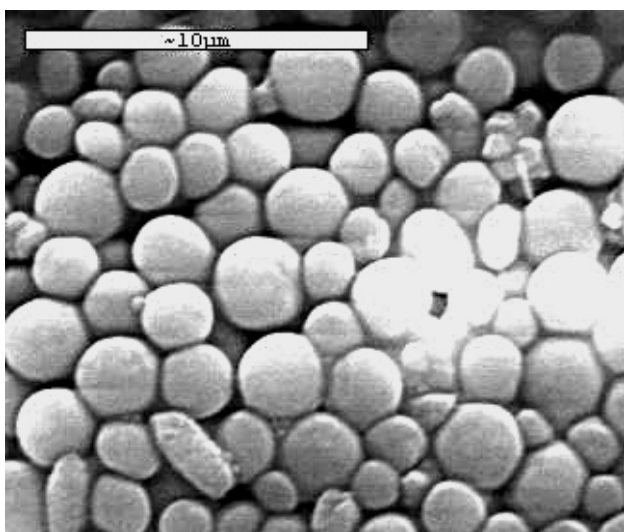
Figure 5.1-2: SEM pictures of $CaCO_3$ in presence of PEG-*b*-pGlu (**18c** - **g**) with different block length, **a)** n = 6, **b)** n = 10, scale bar 20 μm, **c)** n = 16, **d)** n = 20, **e)** n = 25.

A reason for the stabilisation of metastable vaterite by double hydrophilic block copolymer shown in Table 5-1 for more than one year is the high functional group density along the functional block, which ensures a maximum interaction of the functional groups with the crystal surface. This has important consequences for the stabilisation of the metastable crystal modification as shown in Figure 5.1-3 for the aragonite - calcite transformation and this agrees with results in literature [17].

Aragonite differs from calcite in its crystal structure and symmetry: the latter has all CO_3^{2-} in one plane whereas these anions alternate in the aragonite structure. During a solvent mediated transformation of a metastable crystal modification, the restructuring into the stable modification thermodynamically is usually favoured due to a gain in crystal lattice energy.

With an adsorbed polymer on the crystal surface and a pattern partially resembling that of the Ca^{2+} ions on this particular face, a solution mediated restructuring requires the loosening of many electrostatic Ca^{2+} - polymer bonds. The surface effects may well overbalance the gain in lattice energy for the transformation into calcite. Thus, a polymer can form a protection layer around a thermodynamically metastable crystal and protect it from transformation even if it is only selectively adsorbed on some faces [92]. This is called "soft epitaxy" and is in part analogous to the nucleation of aragonite in nacre [1, 8].
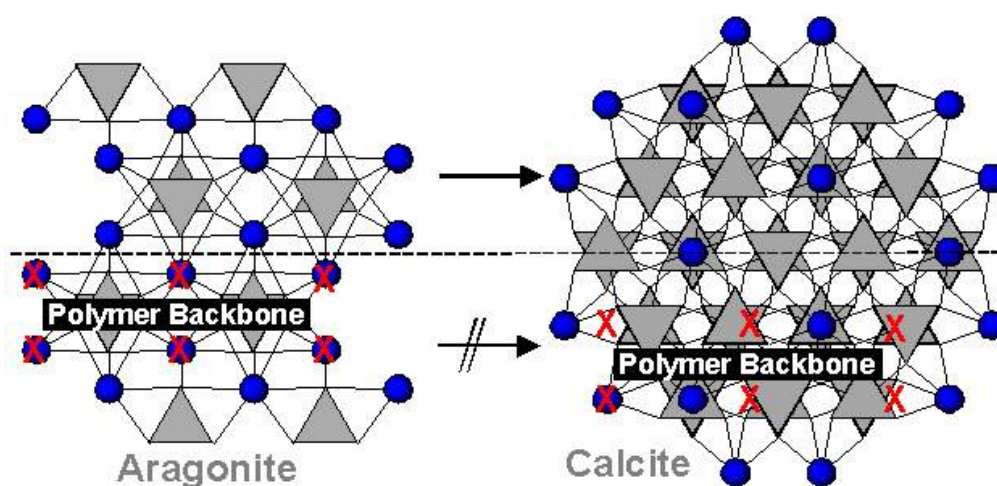

Figure 5.1-3: Transformation of metastable aragonite into calcite (upper half) and after adsorption of a polymer X^- = COO^-. The crystal lattices are drawn to scale, the polymer not. The 001 base faces are shown [92].

The above requirements seem to be fulfilled for all polymers with a peptide block with n > 6 namely:

1.   The interaction between the crystal surface and the adsorbed polymer has to be sufficient to overbalance the lattice energy gain for the formation of the thermodynamically favoured modification.

2.   Soft epitaxy between the polymer (matrix) and the crystal surface has to exist to stabilise the ionic surface pattern on the crystal.

Table 5.1-1 summarizes the structural characterization of all $CaCO_3$ particles by listing their size, shape and crystal modification as obtained from WAXS measurements.

Table 5.1-1: Summary of the experimental results of the crystallization of $CaCO_3$.

Name of polymer	Nr of polymer	Modification of crystals	Size of single crystal	Shape
PEG(110)-*b*-pAsp(10)	**18a**	vaterite	19.8 nm	spheres
PEG(110)-*b*-pAsp(16)	**18b**	vaterite	19.2 nm	spheres
PEG(110)-*b*-pGlu(6)	**18c**	calcite	17.8 nm	irregular
PEG(110)-*b*-pGlu(10)	**18d**	vaterite	15.6 nm	spheres
PEG(110)-*b*-pGlu(16)	**18e**	vaterite	15.2 nm	spheres
PEG(110)-*b*-pGlu(20)	**18f**	vaterite	15.1 nm	spheres
PEG(110)-*b*-pGlu(25)	**18g**	vaterite	15.8 nm	spheres

5.1.2 Time dependence of superstructure formation

In order to get information about the formation mechanism of the vaterite spheres; it was tried to follow the morphological development of the vaterite spheres at different times. Figures 5.1-4 and 5.2-5 show dark field light microscopy pictures of the samples prepared at various early stages from the solution that yielded the spheres. This special light microscopy technique detects the particles via their light scattering and can thus overcome the optical limitation of light microscopy to particles

> 500 nm. In case of this experiment the *Double-Jet* technique was used. After 8 minutes in case of glutamic acid or 10 minutes in case of aspartic acid, respectively, the solution is still clear or slightly opaque, but not turbid. One cannot see anything in light microscopy; therefore dark field microscopy was used, which has a higher resolution and one can see nanoparticles in a range of few nanometers (10 - 100 nm). For the first 14 minutes or 18 minutes, respectively, SEM was not suited to characterise the structures, thus TEM samples were prepared by dropping a drop of the solution on carbon-coated copper grids, waiting for one minute and removing the mother solution by using filter paper. As shown in Figure 5.1-6 few aggregates of evidently amorphous 50 nm nanoparticles (evidenced by the corresponding electron diffraction were found). These aggregates were apparently formed by the sample preparation as in solution (Figure 5.1-4a and 5.1-4a) one can see only individual particles. It is remarkable that the amorphous particles have a rather defined size, which is larger than that of the crystalline vaterite in the superstructures formed later. This implies either multiple nucleation of vaterite in a single amorphous precursor particle or dissolution-recrystallization process.

The actual high supersaturation at early stages is lowered by the formation of a block copolymer-stabilised amorphous intermediate rather than of $CaCO_3$ nanocrystals.

After 14 minutes (PEG-*b*-pGlu (**18d**)) or 18 minutes (PEG-*b*-pAsp (**18a**)), respectively, turbidity was observed in the solution and large micron-sized particles were generated and already observed in the light microscopy. Then they were characterised by SEM. In Figures 5.1-4b and 5.1-5b one can see that already at the early stages quite large spherical particles with size of ~ 2 μm are formed. After 60 minutes (Figures 5.1-4c and 5.1-5c), the turbidity had considerably increased; this is caused by the increase of the total number of the particles produced but their size remained constant (~ 2 μm).

a)
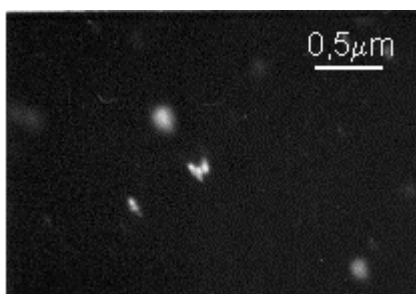
b)
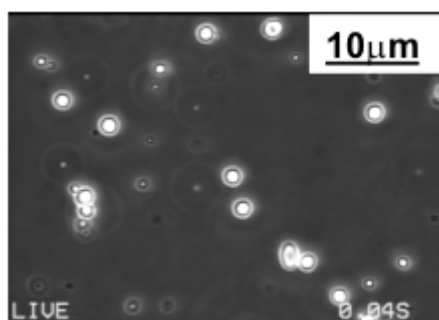
c)
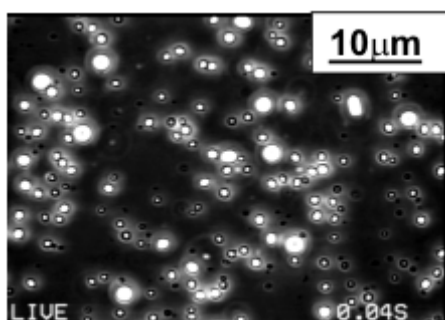
Figure 5.1-4: Picture of CaCO$_3$ in light microscopy crystallised in presence of PEG-*b*-pGlu (**18d**, n = 10) after **a**) 8 min **b)** 14 min **c)** 60 min.

a)
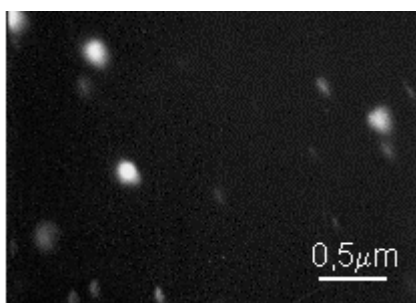
b)
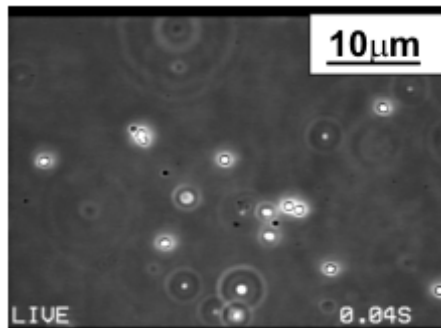
c)
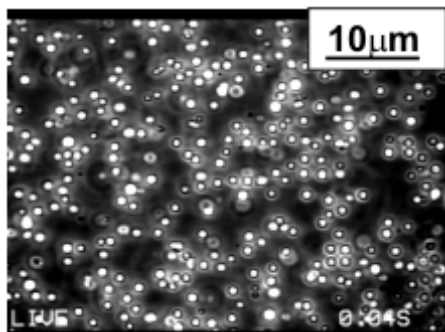
Figure 5.1-5: Picture of CaCO$_3$ in light microscopy crystallised in presence of PEG-*b*-pAsp (**18a**, n = 10) after **a**) 10 min **b)** 18 min **c)** 60 min.

a)   b)
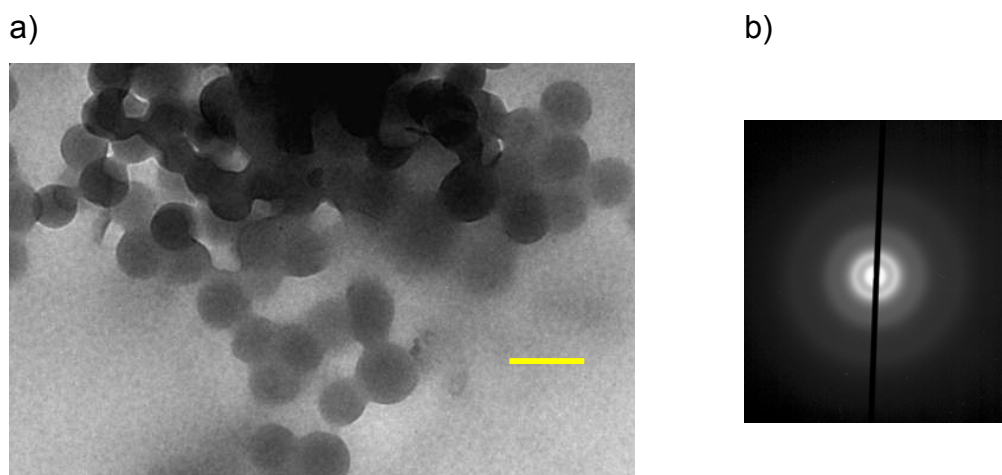
Figure 5.1-6: a) TEM picture of CaCO$_3$ crystallised in presence of PEG-*b*-pGlu (**18d**, n = 10) after 8 min, scale bar = 100 nm, **b)** electron diffraction of this sample.

According to WAXS measurement (Figure 5.1-7) the obtained spheres are superstructures of vaterite nanocrystals (size 15 - 20 nm, Table 5.1-1).
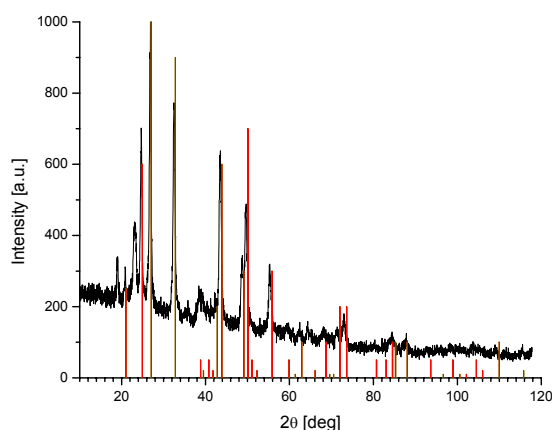
Figure 5.1-7: —— WAXS of CaCO$_3$ in presence of PEG-*b*-pGlu (**18d**, n = 10) and —— vaterite.

There are two possibilities how the observed spherical particle superstructures can be formed. The first is simple aggregation of similar-sized nanoparticles and the second is aggregation of the nanoparticles with subsequent nanoparticle growth in the superstructures (Figure 5.1-8). In case of the vaterite spheres obtained in this work the first case is valid, based on the results from dark field microscopy. Small individual nanoparticles were seen in a range of a few nanometers (~ 20 nm), corresponding to the WAXS measurement of the nanoparticles in the final superstructures. Thus the transformation of amorphous precursor particles (50 nm) to

vaterite nanocrystals (20 nm) is followed by a quite rapid nanocrystal aggregation to spherical superstructure (see Figures 5.1-4 and 5.1-5) under size preservation of the vaterite nanocrystals. This mechanism is quite different to that found by Qi et al [18], where first, the amorphous nanoparticles aggregate to string like structures, which then form spherical superstructures via dumbbell shaped precursors.
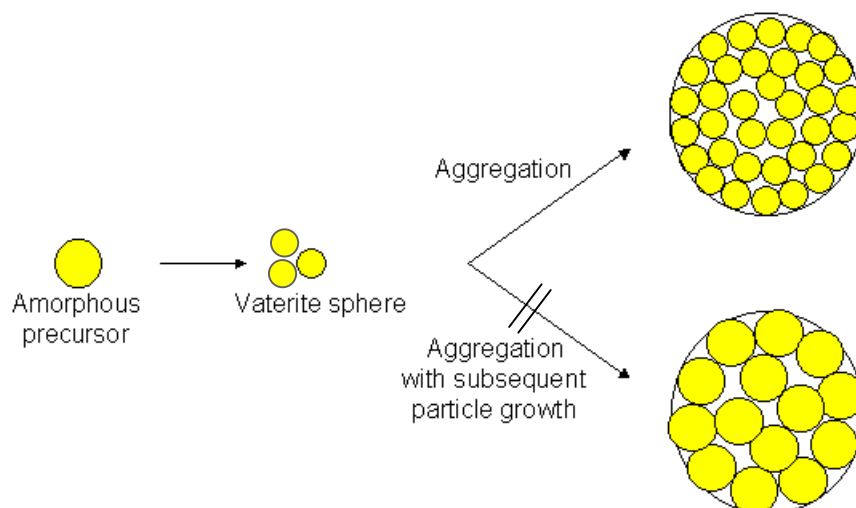
Figure 5.1-8: Model of vaterite spheres formation.

5.1.3 Influence of the crystallization speed

As it is described in chapter 3.8 there are differences between the *Kitano* and *Double-Jet* methods. Both methods were applied for different polymer concentrations (PEG-*b*-pAsp (**18a**, **b**) and PEG-*b*-pGlu (**18c** - **g**)). The resulting crystals are characterised first by light microscopy to see the shapes of the crystals in a solution of the polymer and then by scanning electron microscopy (SEM) (dry samples). It is important to prove that the crystals seen in SEM pictures are the same as in a solution, to prove the absence of drying artefacts during the SEM sample preparation.

Comparison of crystallization methods:

Figures 5.1-9a and 5.1-10a show pictures of crystals grown by the *Kitano* method in presence of PEG-*b*-PAsp (**18a**) and PEG-*b*-Pglu (**18e**) block copolymer. Those particles are spherical and approximately 10 μm in size. On the other hand particles showed in Figures 5.1-9b and 5.1-10b, which are formed by the *Double-Jet* method in presence of the same block copolymer as in case of the *Kitano* method, are as well spheres but only 2 - 3 μm in size.

a)   b)
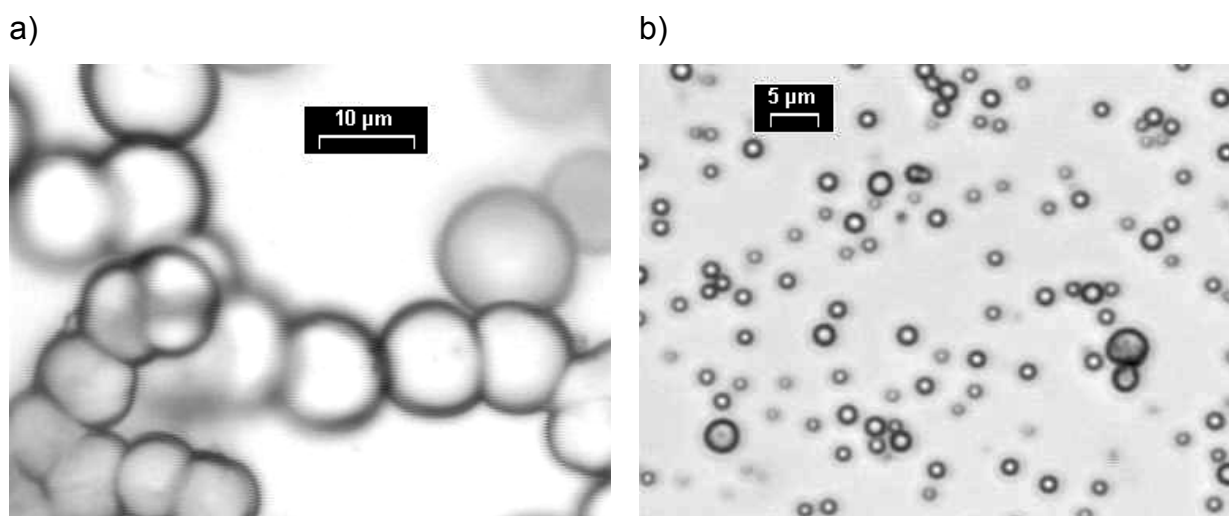
Figure 5.1-9: Pictures of CaCO$_3$ crystals in light microscopy in presence of PEG-*b*-pGlu (**18e**, n=16), a) *Kitano* method, b) *Double-Jet* method.

a)   b)
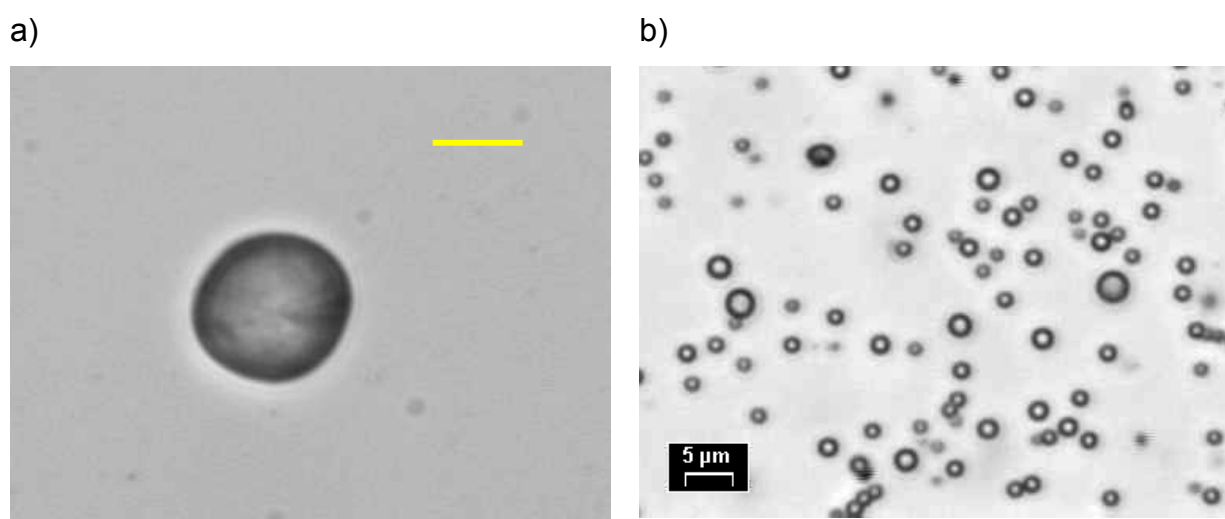
Figure 5.1-10: Pictures of CaCO$_3$ crystals in light microscopy in presence of PEG-*b*-pAsp (**18a**, n=10), **a)** *Kitano* method, scale bar: 10 μm, **b)** *Double-Jet* method.

According to the wide angle X-ray scattering (WAXS) measurement all those spheres are aggregates of small vaterite crystals of size 15 - 20 nm (Table 5.1-1). All samples (crystals in polymer solution) were kept for a whole year in closed vessels and then WAXS was measured again. The results were unchanged proving the vaterite modification. A reason for the stabilisation is explained previously in chapter 5.1.1. The *Double-Jet* technique produced smaller particles because it is a faster method than the *Kitano* method meaning that more nuclei are produced at a unit time leading to a fast aggregation into comparatively smaller superstructures. On the other hand both methods yielded the same shape due to the polymer influence upon the superstructure morphology. Apparently in the *Kitano* method, a higher amount of precursor seems to be stabilized and this higher concentration leads to larger particles as compared to the Double-Jet method.

Polymer concentration dependence:

The polymer concentration in a solution is important for the mineralization process. A whole range of solutions with different polymer concentration was prepared (0.001 g/l - 1 g/l), and $CaCO_3$ was crystallised by the *Kitano* procedure.

At a polymer concentration of 0.001 g/l, the block copolymers loose their ability to control the $CaCO_3$ morphology and modification, see Figure 5.1-11a and Figure 5.1-12a. The particles several of micrometers in size exhibit the typical rhombohedral symmetry of calcite. With increasing polymer concentration the shape of particles changed and at the polymer concentration c = 1 g/l spheres were produced (Figure 5.1-11d and 5.1-12d), consisting of vaterite nanocrystals (15 - 20 nm, WAXS, Table 5.1-1). The observations from this experiment lead to the conclusion that at the polymer concentration lower than 0.05 g/l the double hydrophilic block copolymers cannot control and stabilize the $CaCO_3$ morphology and modification anymore.

a)

b)

c)

d)
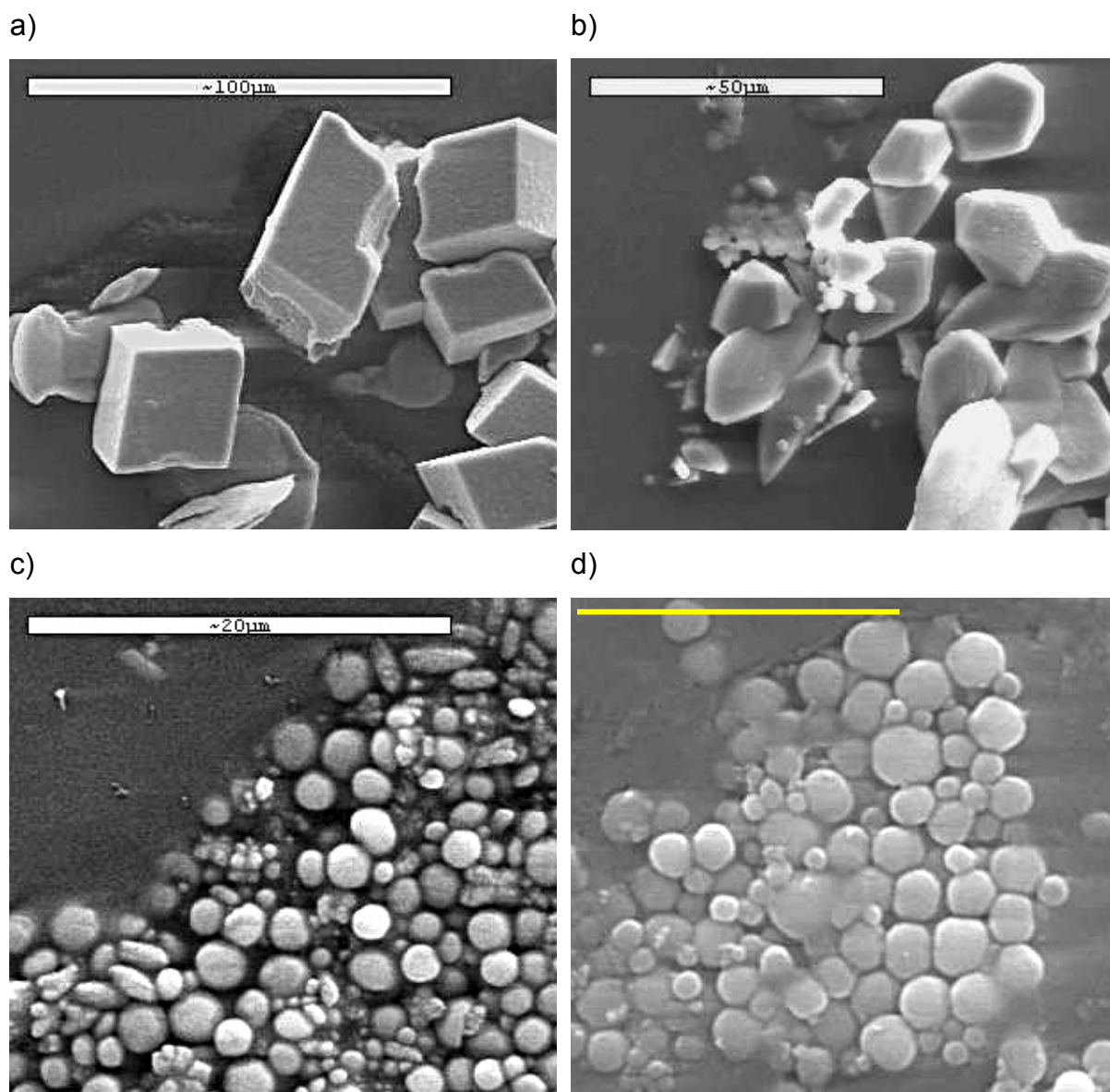
Figure 5.1-11: SEM picture of CaCO$_3$ crystallised in presence of PEG-*b*-pAsp (**18a**, n = 10) concentration of polymer **a)** c = 0.001 g/l; **b)** c = 0.008 g/l; **c)** c = 0.05 g/l; **d)** c = 1 g/l, scale bar 10 μm.

a)

b)

c)

d)
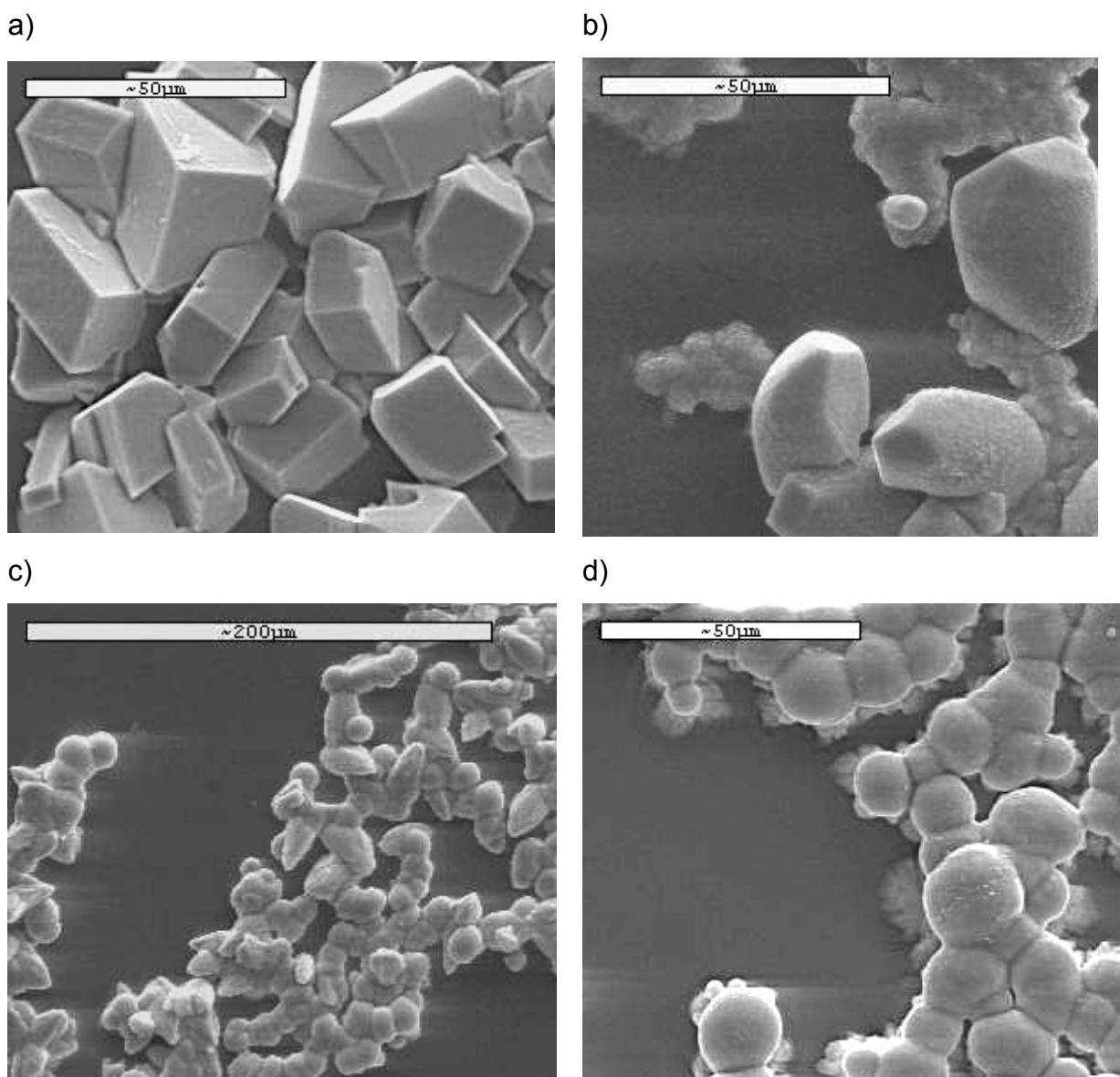
Figure 5.1-12: SEM picture of CaCO$_3$ crystallised in presence of PEG-*b*-pGlu (**18d**, n = 10) concentration of polymer **a)** c = 0.001 g/l; **b)** c = 0.008 g/l; **c)** c = 0.05 g/l; **d)** c = 1 g/l.

5.1.4 Influence of different functional groups

As it was described previously, PEG-*b*-pGlu (**18c** - **g**) and PEG-*b*-pAsp (**18a**, **b**) block copolymers have free active COOH groups in their side chains, which can interact with Ca^{2+} ions. Except PEG-*b*-pGlu (**18c**, n = 6), which does not have an influence on modification and morphology of crystals, all other block copolymers do.

All of them interact with minerals and spherical superstructures composed of vaterite nanocrystals are formed.

The block copolymer PEG-*b*-p(PSer) (**20**) has free active PO_3H_2 groups in the side chains, which can as well interact with the mineral and control morphology and modification of $CaCO_3$ crystals.

a)   b)
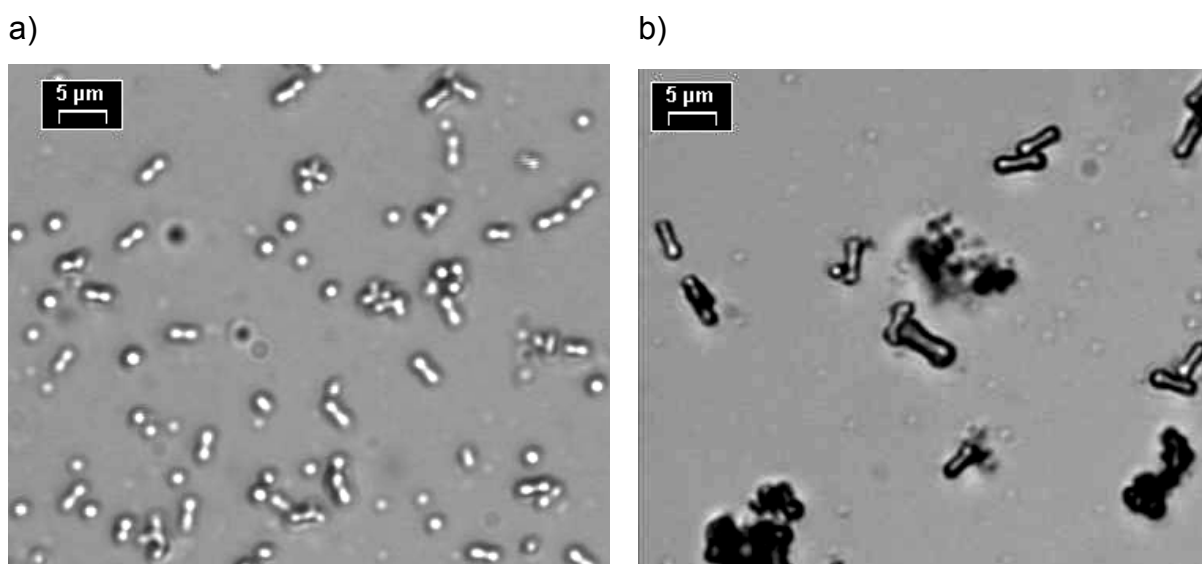
Figure 5.1-13: Light microscopy picture of $CaCO_3$ crystallised in presence of PEG-*b*-p(PSer) (**20**, n = 14) with polymer concentration 10 mg / 10 ml and different speed of adding Na_2CO_3 and $CaCl_2$, **a)** v = 333 μl/h that is formation of 2.78 μmol of $CaCO_3$ / min and **b)** v = 55 μl/h that is formation of 0.458 μmol of $CaCO_3$ / min.

Figure 5.1-13a shows light microscopy pictures of crystals of $CaCO_3$ mineralised in presence of a phosphoserine block copolymer by the *Double Jet* method. The concentration of the polymer in solution is 1 g/l (10 ml of a solution) the speed of adding Na_2CO_3 and $CaCl_2$ solutions is 333 μl/h (formation of 2.78 μmol of $CaCO_3$ / min). These conditions were as well used in previous *Double-Jet* experiments. The produced particles are 2 - 3 μm in size having dumbbell-like morphology. Figure 5.1-13b shows a picture of the particles obtained with a lower $CaCO_3$ addition rate. Here the particles are more elongated, dumbbell-like and bigger (about 5 μm in size). This experiment is done under the same conditions, and the only difference is the addition speed of both solutions (Na_2CO_3 and $CaCl_2$). It is 55 μl/hr (formation of 0.458 μmol $CaCO_3$ / min). With higher $CaCO_3$ addition rate, smaller dumbbell-like particles are produced due to faster nucleation and aggregation

rate. On the other hand, with lower $CaCO_3$ addition rate a higher amount of precursor seems to be stabilized and this higher concentration leads to larger and more rod-like particles with only outgrown ends as compared to the higher $CaCO_3$ addition rate.

The WAXS measurement reveals that both particles are composed of pure calcite (17.5 nm, Table 5.1-2). Both samples were kept in solution in closed vessels for more than half a year and then checked again by light microscopy, observing the same dumbbell-like particles and no further growth. There are some examples in literature, where the dumbbells are observed but with subsequent growth [93, 94]. For example, formation of fluoroapatite in presence of a gelatine matrix is reported by Busch & Kniep [93, 94]. They observed crystal growth from a rod via fractal growth at the ends of the rod leading to dumbbell-like particles with their ends growing further together and resulting in a final spherical particle. They investigated the slow crystallization of apatite crystals with a primary crystal of already approximately 15 μm length and final spherical particles of about 70 μm in diameter, which are easily accessible by microscopic techniques. But the particles produced in this work are smaller. Final particles < 5 μm with primary crystals ~ 10 - 20 nm hindered the direct observation of the structure formation. Thus, only final dumbbell-like particles are observed.

Table 5.1-2: Summary of the experimental results of the crystallization of $CaCO_3$.

Name of polymer	Nr of polymer	Modification of crystals	Size of single crystal	Shape
PEG(110)-*b*-p(PSer)(14)	**20**	calcite	17.5 nm	dumbbells

There are differences in modification and morphology of $CaCO_3$ particles produced in presence of PEG-*b*-pGlu (**18c** - **g**) and PEG-*b*-pAsp (**18a**, **b**) block copolymers and those in presence of PEG-*b*-p(PSer) (**20**). In case of PEG-*b*-pGlu (**18d** - **g**) and PEG-*b*-pAsp (**18a**, **b**) block copolymers, vaterite spheres were predominantly obtained. On the other hand, the block copolymer PEG-*b*-p(PSer) (**20**) yielded dumbbell-like particles containing calcite. Obviously, vaterite tends to form spherical superstructure, whereas calcite leads to dumbbell morphologies [18]. Here, the prepared block copolymers seem to lead to a totally different aggregation mechanism. An electric dipole field with different degrees of electric shielding of a

quadrupole could explain this differences in mechanism, as it was described by Cölfen [92]. It is known that the interaction between a phospho- functional group and $CaCO_3$ crystal is strong, thus the shielding of the electric field lines is as well strong and that leads to the dumbbell formation. On the other hand the interaction between carboxylic acid and mineral are weaker, meaning lower shielding of the electric field lines and consequently spheres formation.

5.2 $BaSO_4$ mineralization

The fast *Double-Jet* and the slow *"Precipitation"* methods were also used for the preparation of $BaSO_4$ particles. The advantages of $BaSO_4$ are pH independence and only one crystal modification. All polymers mentioned in Table 5-1 were used to modify the morphology and the modification of $BaSO_4$ crystals, depending on the experimental conditions, for example different technique of precipitation, concentration of polymer, pH, different functional groups of the active peptide chain or influence of the polymer secondary structure were investigated. Spherical particle were predominantly obtained by the *Double-Jet* method, corresponding to literature results [19, 20]. Where similar polymers were used for the $BaSO_4$ mineralization and spheres were as well observed. In case of different secondary structure of PEG-*b*-pGlu (**18e**) dumbbell-like particles were obtained. The resulting $BaSO_4$ particles were characterized by light microscopy in solution and by scanning electron microscopy (SEM), thus allowing the precise characterization of size and shape. In almost every case, the crystal sizes and shapes observed with optical microscopy (crystals in solution) correspond to those which were observed using SEM. Thus, drying artefacts during sample preparation can be excluded, unless explicitly stated.

5.2.1 Influence of the crystallization speed

For the mineralization process of $BaSO_4$ the fast *Double-Jet* method as in case of $CaCO_3$ as well as a slow "precipitation" technique were applied (for more details see chapter 9.3). Both methods were used for different polymer

concentrations. The resulting BaSO$_4$ precipitates were then characterised by light microscopy and scanning electron microscopy (SEM).

Comparison of crystallization methods:

Figure 5.2-1 shows two completely different pictures of BaSO$_4$ particles produced at same conditions (polymer concentration, pH, temperature), the only difference is the technique of precipitation. By the precipitation method (Figure 5.2-1a) the particles had irregular shape, mostly plate-like and formed star-like aggregates. On the other hand particles from *Double-Jet* method had egg-like shapes. This experiment was done in presence of PEG-*b*-pGlu (**18c** - **g**) and PEG-*b*-pAsp (**18a**, **b**) block copolymers and at the standard conditions meaning concentration of 1 g/l, 25 °C and pH = 4 and 8, because of the different secondary structure of glutamic and aspartic acid.

a)

b)
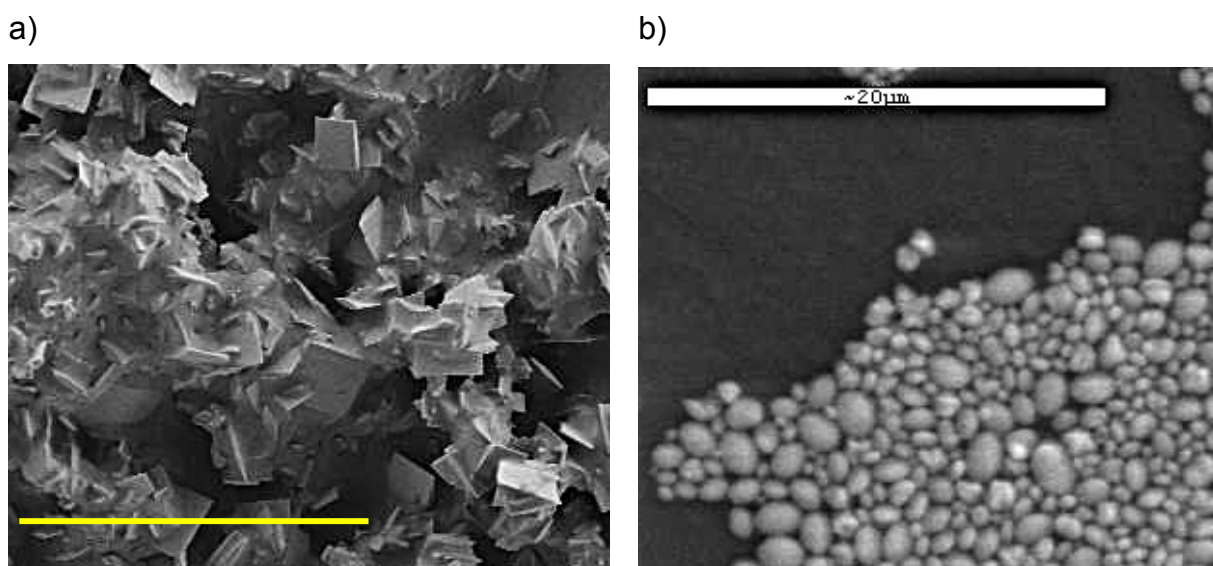
Figure 5.2-1: SEM pictures of BaSO4 crystals in presence of PEG-*b*-pGlu (**18d**, n = 10) at pH = 4, prepared by **a)** "precipitation" method, scale bar = 20 μm, **b)** Double-Jet method.

The plate-like particle and their aggregates mean no influence of the polymer. This corresponds to results published by Qi [20]. We worked below the pK$_a$ of poly(glutamic acid) and poly(aspartic) acid, which should be around pH = 4,5 that means the polymer is fully protonated turning the pGlu block less hydrophobic.

Nevertheless, the fast *Double-Jet* method leads to a stabilization of nanoparticles, which aggregate to superstructures whereas a slow "precipitation" technique yields single $BaSO_4$ crystals. Obviously, the speed of precipitation is very important. Fast crystallization leads to nanoparticles. They may be stabilized as the IEP of $BaSO_4$ is ~ 3,9 [92] thus the $BaSO_4$ particles exhibit no net charge and may be stabilized by the hydrophobic pGlu block. However, these results show that this is only a kinetic effect as slow crystallization yields big $BaSO_4$ platelets, which are most likely single crystals. The pH = 4 was chosen by purpose, because of a different secondary structure of PEG-*b*-pGlu (**18c** - **g** and PEG-*b*-pAsp (**18a**, **b**) block copolymers. More details on the influence of the secondary structure will be described in chapter 5.2.2.

A similar example of different morphologies for the same mineral precipitated at the same conditions by a different crystallization technique has been recently published [95]. Here, $CaCO_3$ was precipitated by the fast *Double-Jet* method in presence of phosphorylated poly(ethylene glycol)-block-poly[2-(2-hydroxy ethyl)-ethylene] (PEG-*b*-PHEE) and spheres were obtained. On the other hand, when $CaCO_3$ was precipitated at the same condition but by the slow *Kitano* method, complex cone-like or flower-like superstructures were formed. However, here we observed plates, which are most likely single crystalline.

Influence of the polymer concentration and pH

The first series of polymer solutions (PEG-*b*-pGlu (**18c** - **g**) and PEG-*b*-pAsp (**18a**, **b**)) with the polymer concentrations c = 0.5 g/l; 1 g/l; 2 g/l and 5 g/l was adjusted to pH = 4. The second one with the same polymer concentrations c= 0.5 g/l; 1 g/l and 5 g/l was adjusted to pH = 8 and both crystallization techniques were applied. Both block copolymers are similar and thus similar results should be expected.

Figures 5.2-3 and 5.2-4 show pictures of $BaSO_4$ particles in presence of PEG-*b*-pGlu (**18d**) block copolymer produced by the *Double-Jet* technique at pH = 4 and 8. In both cases the pH had no influence and egg-like particles were obtained.

These results are different to the literature findings [20]. There, the others observed, that the $BaSO_4$ particles crystallized in presence of a block copolymer poly(ethylene glycol)-*b*-poly(methacrylic acid) (PEG-*b*-PMAA) (with similar block

length as in case of this work n ~ 7) at different pH had different shapes. With decreasing pH from 11 to 5, the particle morphology essentially changed from ellipsoidal particles or oval (pH = 11) to peanuts (pH = 9), a mixture of peanuts and single-notched spheres, i.e., peaches (pH = 7), and spheres (pH = 5) and the particle size gradually increased from around 0.65 to 2 μm. These differences could be explained by different polymer structure. The polypeptide are presumably less efficient because, the distance of carboxyl groups in PEG-*b*-PMAA block copolymer is found smaller (~ 2.5 Å) than in the polypeptides PEG-*b*-pGlu (**18c** - **g**) and PEG-*b*-pAsp (**18a**, **b**) (~ 6 - 7 Å) according to the calculation of the molecular conformation in vacuum with Cerius^2 software (Accelrys) (see Figure 5.2-2).

a)
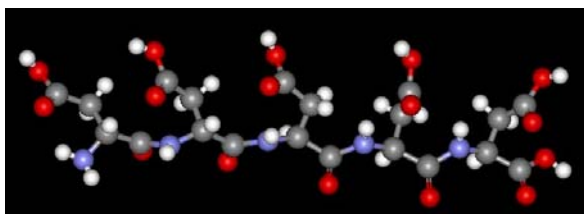
b)
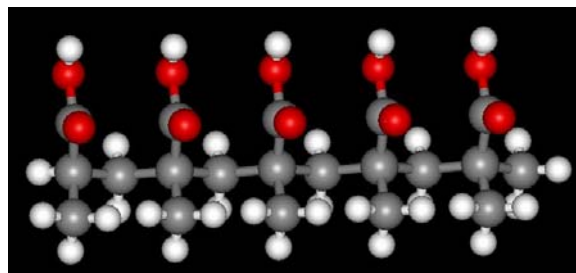
c)
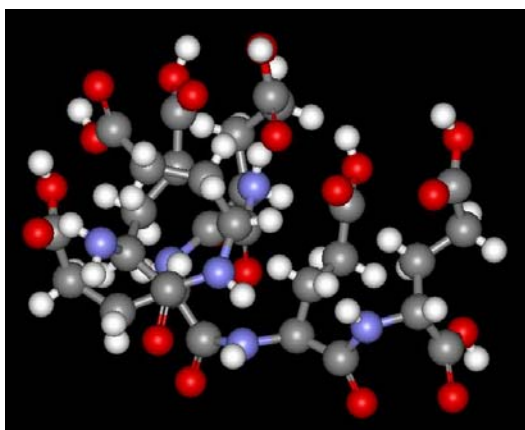
Figure 5.2-2: The molecular conformation in vacuum calculated with Cerius^2 software (Accelrys) **a)** pAsp block (n = 5), **b)** pMAA block (n = 5), **c)** pGlu block (n = 5).

a)

b)

c)

d)
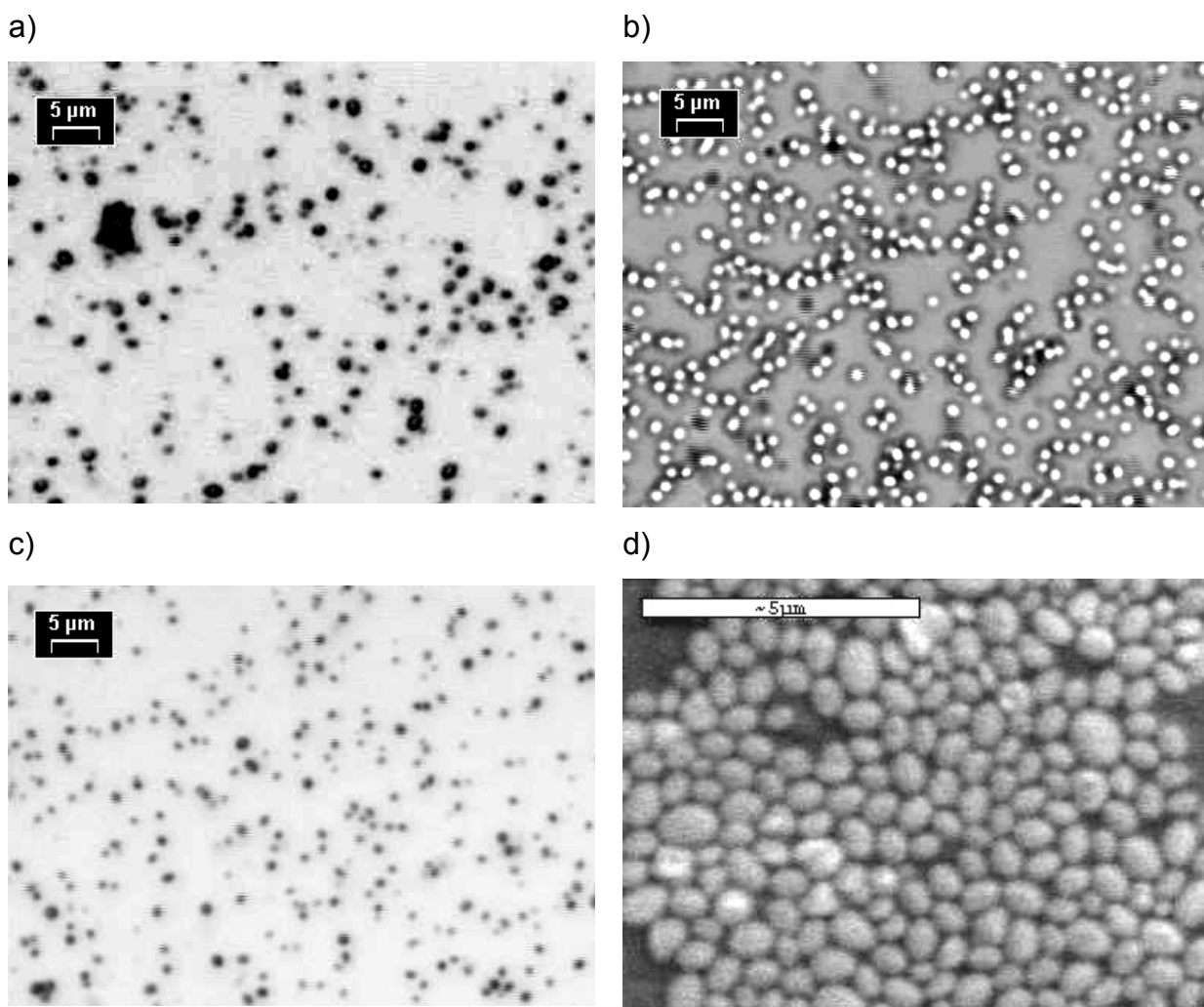
Figure 5.2-3: Picture of BaSO$_4$ in light microscopy (*DJ method* 0,5M Ba(OAc)$_2$ solution and 0.5M (NH$_4$)$_2$SO$_4$ solution) in presence of PEG-*b*-pGlu (**18d**, n = 10) and pH = 8 and polymer concentration **a)** c = 0.5 g/l, **b)** c = 1 g/l, **c)** c = 5 g/l, **d)** SEM picture of sample with polymer concentration c = 1 g/l.

a)

b)
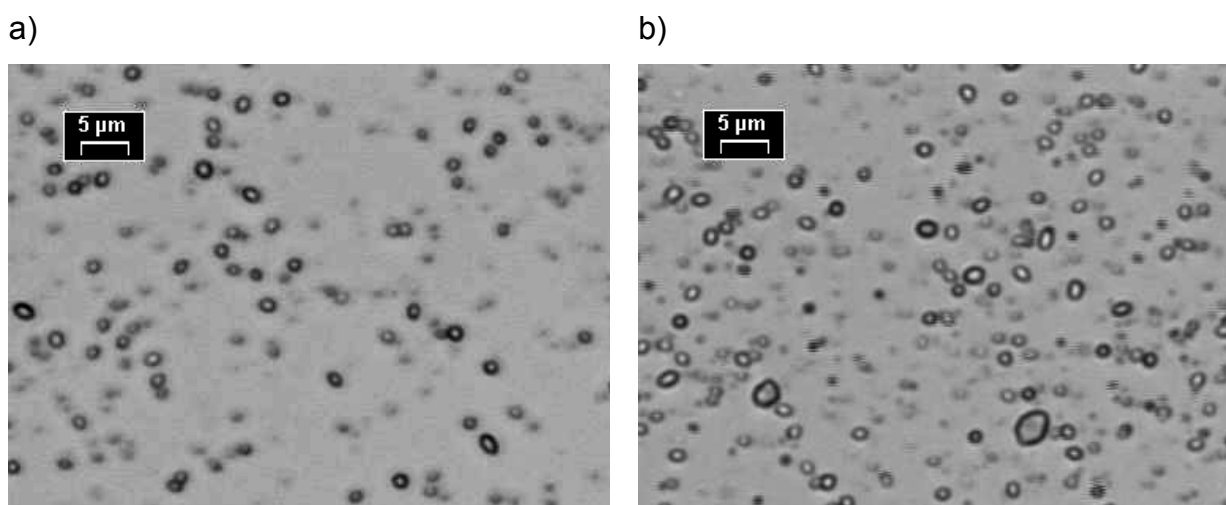
Figure 5.2-4 continued on the next page.

c)   d)
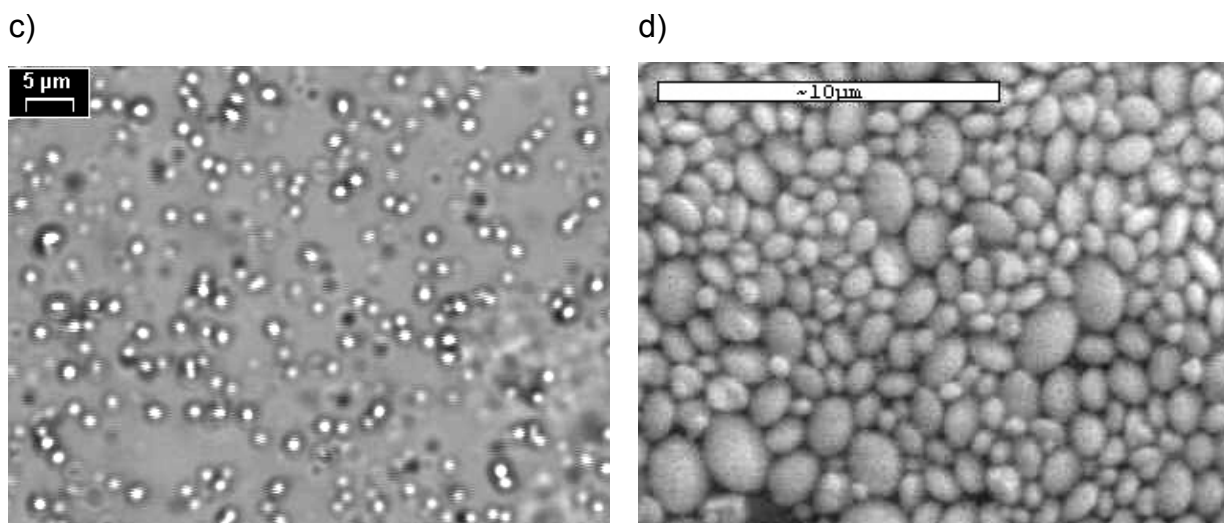
Figure 5.2-4: Picture of BaSO$_4$ in light microscopy (*DJ method* 0.5M Ba(OAc)$_2$ solution and 0.5M (NH$_4$)$_2$SO$_4$ solution) in presence of PEG-*b*-pGlu (**18d**, n = 10) and pH = 4 and polymer concentration, **a)** c = 0.5 g/l, **b)** c = 1 g/l, **c)** c = 5 g/l, **d)** SEM picture of sample with polymer concentration c = 1 g/l.

Figures 5.2-5 and 5.2-6 show pictures of BaSO$_4$ crystallised in presence of PEG-*b*-pGlu (**18d**) block copolymer at pH = 4 and 8 by the slow "precipitation" method. Particles at pH = 4 had an irregular shape, on the other hand, particles at pH = 8 had an egg-like shape. This is a similar effect as already observed in Figure 5.2-1. But here one can see that even at slow crystallization, the polymers stabilize nanoparticles at higher pH, and larger, probably single crystalline, structures evolve at lower pH where the electrostatic polymer-crystal interaction is significantly decreased. This effect seems to be independent of the polymer concentration in the range of 0.5 – 5 g/l.

a)
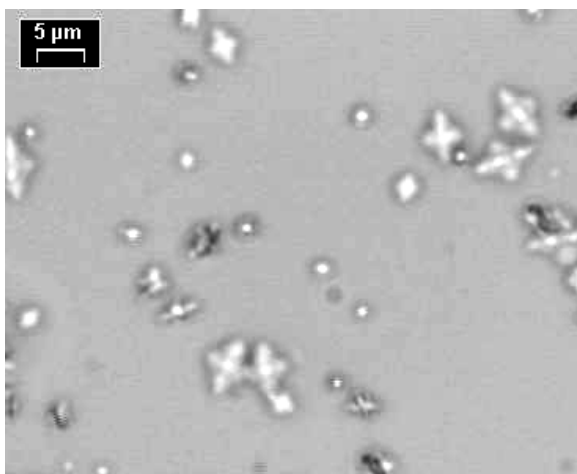
b)
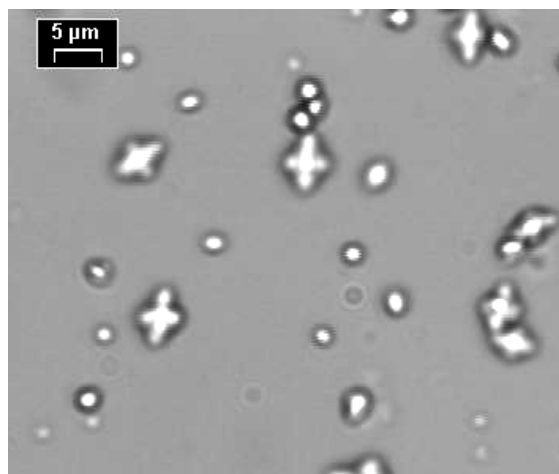
c)
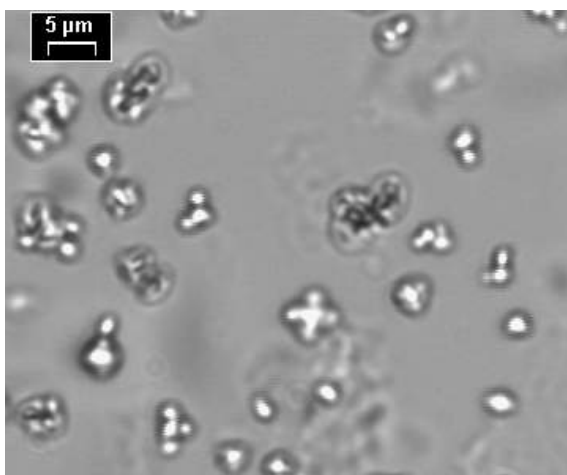
Figure 5.2-5: Light microscopy pictures of BaSO$_4$ in presence of PEG-*b*-pGlu (**18d**, n = 10) and at pH $\approx$ 4 prepared by "precipitation" method, concentration of polymer **a)** c = 0.5 g/l, **b)** c = 1 g/l **c)** c = 5 g/l.

a)

b)

c)   d)

Figure 5.2-6: Light microscopy pictures of BaSO$_4$ in presence of PEG-*b*-pGlu (**18d**, n = 10) and at pH ≈ 8 by "precipitation" method, **a)** concentration of polymer c = 0.5 g/l, **b)** concentration of polymer c = 1 g/l, **c)** concentration of polymer c = 5 g/l, **d)** SEM picture of BaSO$_4$ concentration of polymer c = 1 g/l.

a)   b)
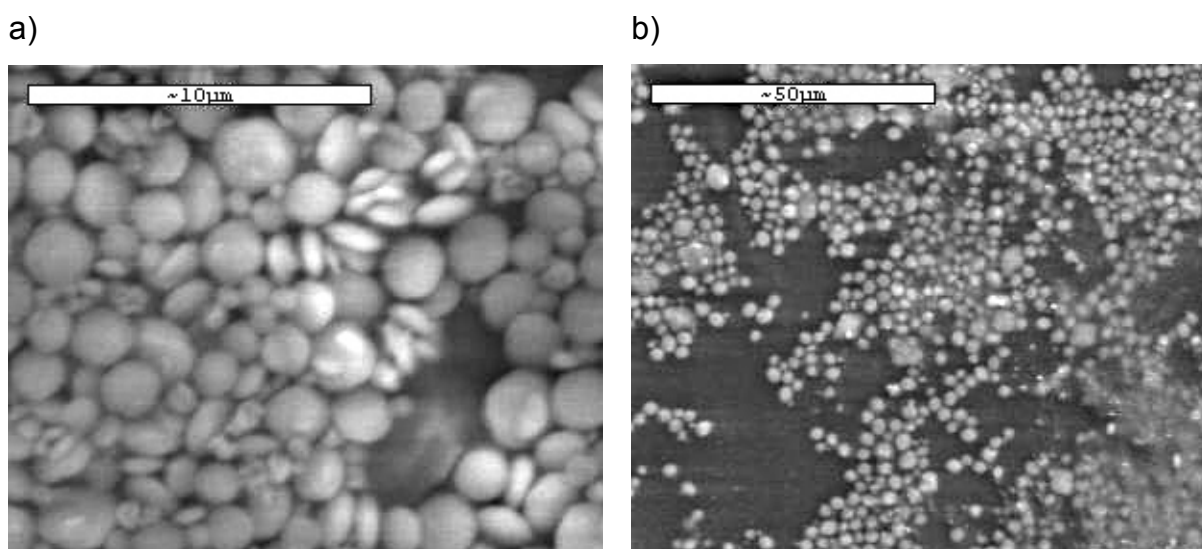
Figure 5.2-7: SEM pictures of BaSO$_4$ in presence of PEG-*b*-pAsp (**18a**, n = 10) by "Precipitation" method, **a)** concentration of polymer c = 1 g/l and pH = 8; **b)** concentration of polymer c = 1 g/l and pH = 4.

Figure 5.2-7 shows pictures of BaSO$_4$ crystallised in presence of PEG-*b*-pAsp (**18a**) block copolymer at pH = 4 and 8 by the slow "precipitation" method. Particles at pH = 4 had the similar shape as particles at pH = 8 meaning egg-like shape or lentil-like shape, respectively. There are differences in the results for poly(aspartic acid) and poly(glutamic acid) block copolymers at pH = 4. This could be explained by a different polymer secondary structure, which is discussed in following chapter.

5.2.2 Influence of the polymer secondary structure

In chapter 4.5, the secondary structures of PEG-*b*-pGlu (**18c** - **g**) and PEG-*b*-pAsp (**18a**, **b**) are described. The block copolymers PEG-*b*-pGlu (**18d** - **g**) formed an α-helix (95% and 5% random coil, due to the polymer polydispersity, calculated according to the literature [98]) at pH = 4 and normal room temperature. When the temperature was increased to 60°C, the CD spectrum changed and the polymer seems to refold into the β-sheet structure (95% and 5% random coil, calculated according to the literature [98]). Consequently, mineralization at different temperature was done to explore the effect of the polymer secondary structure onto the outcome mineralization. Reference samples without any additives were also performed to prove that the changes are not due to different conditions but just due to different secondary structure of block copolymer, in every case rectangular platelet were obtained.

Figure 5.2-8 shows two pictures of $BaSO_4$ crystallised in presence of PEG-*b*-pGlu (**18d**) at pH = 4 by *Double-Jet* method. The first light microscopy picture was the experiment at normal room temperature. Particles posses an egg-like shape, as it was already shown above. The second light microscopy picture shows $BaSO_4$ particles crystallised at 60°C, where the polymer adopts a β-sheet structure (95% and 5% random coil, calculated according to the literature [98]). A change in the particle morphology to the dumbbell-like shape was observed. To get a better idea about the shape of particles, SEM was performed. SEM confirmed dumbbell-like particles around 2 μm in size. The sample was kept in solution in a closed vessel for more than half a year and then checked again by light microscopy, observing the same dumbbell-like particles and no further growth. In Figure 4.4-4 in chapter 4.4, the differences between both secondary structures can be observed. The block copolymer PEG-*b*-pGlu (**18d** - **g**) formed an α-helix (90 – 95% and 5 – 10% random coil, calculated according to the literature [98]) at pH = 4 and room temperature, which has a turn every 3.6 monomer units meaning that a carboxyl group is found at the same orientation on the helix only every 18 monomer units. This means that for pGlu block with n = 10, only one interacting carboxyl group can be discussed leading to a weak interaction with the crystal. On the other hand, the block copolymer PEG-*b*-pGlu (**18e**) at pH = 4 and at higher temperature 60 °C adopts a β-sheet (95% and 5%

random coil, calculated according to the literature [98]) according to the CD spectra (7 Å between two carboxyl groups which show the same orientation. This means that for pGlu block with n = 10, 5 interacting carboxyl groups need to be discussed leading to a much stronger polymer-crystal interaction compared to an α-helix. According to the electric field controlled superstructure formation suggested by Cölfen [92], one would predict spherical morphologies for the block copolymer with an α-helix conformation (95%) and dumbbell-like morphologies for that with the β-sheet conformation (95%). This corresponds to the experimental findings (Figure 5.2-8) and shows that polymer conformations also have to be discussed as variables for additive controlled crystal morphologenesis.

The literature [20] reports dumbbell-like $BaSO_4$ particles but in presence of PEG-*b*-PMAA at pH = 9 and at room temperature.

a)

b)

c)
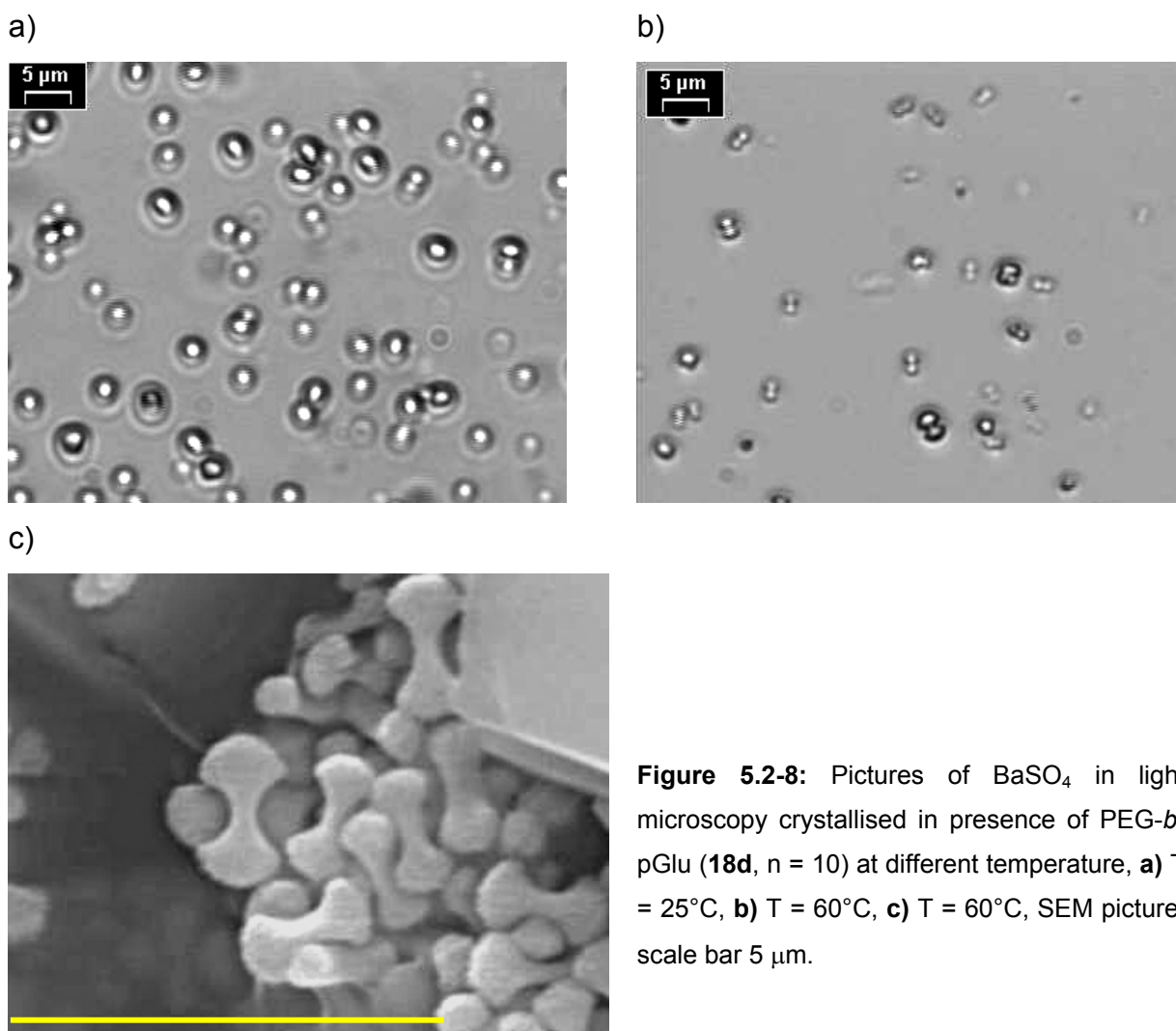
Figure 5.2-8: Pictures of $BaSO_4$ in light microscopy crystallised in presence of PEG-*b*-pGlu (**18d**, n = 10) at different temperature, **a)** T = 25°C, **b)** T = 60°C, **c)** T = 60°C, SEM picture, scale bar 5 μm.

5.2.3 Influence of different polymer functional group

As it was presented above, PEG-*b*-pGlu (**18c** - **g**) and PEG-*b*-pAsp (**18a**, **b**) block copolymers have free active COOH groups in their side chains, which interact with Ba^{2+} ions. All of them interact with minerals, and spheres, egg-like particles or star-like particles were formed. In presence of PEG-*b*-pGlu (**18e**) block copolymers dumbbell-like particles were formed at 60°C and pH = 4.

The block copolymer PEG-*b*-p(PSer) (**20**) possesses free active PO_3H_2 groups in its side chains, which can as well interact with the mineral and control morphology of $BaSO_4$ crystals. The phosphate is more acidic than COOH. Another important difference is that it has two pK_a's (pK_{a1} at pH 2 and pK_{a2} at pH 7,3) in contrast to glutamic and aspartic acid with their pK_a around pH 4,5.

a)

b)

c)
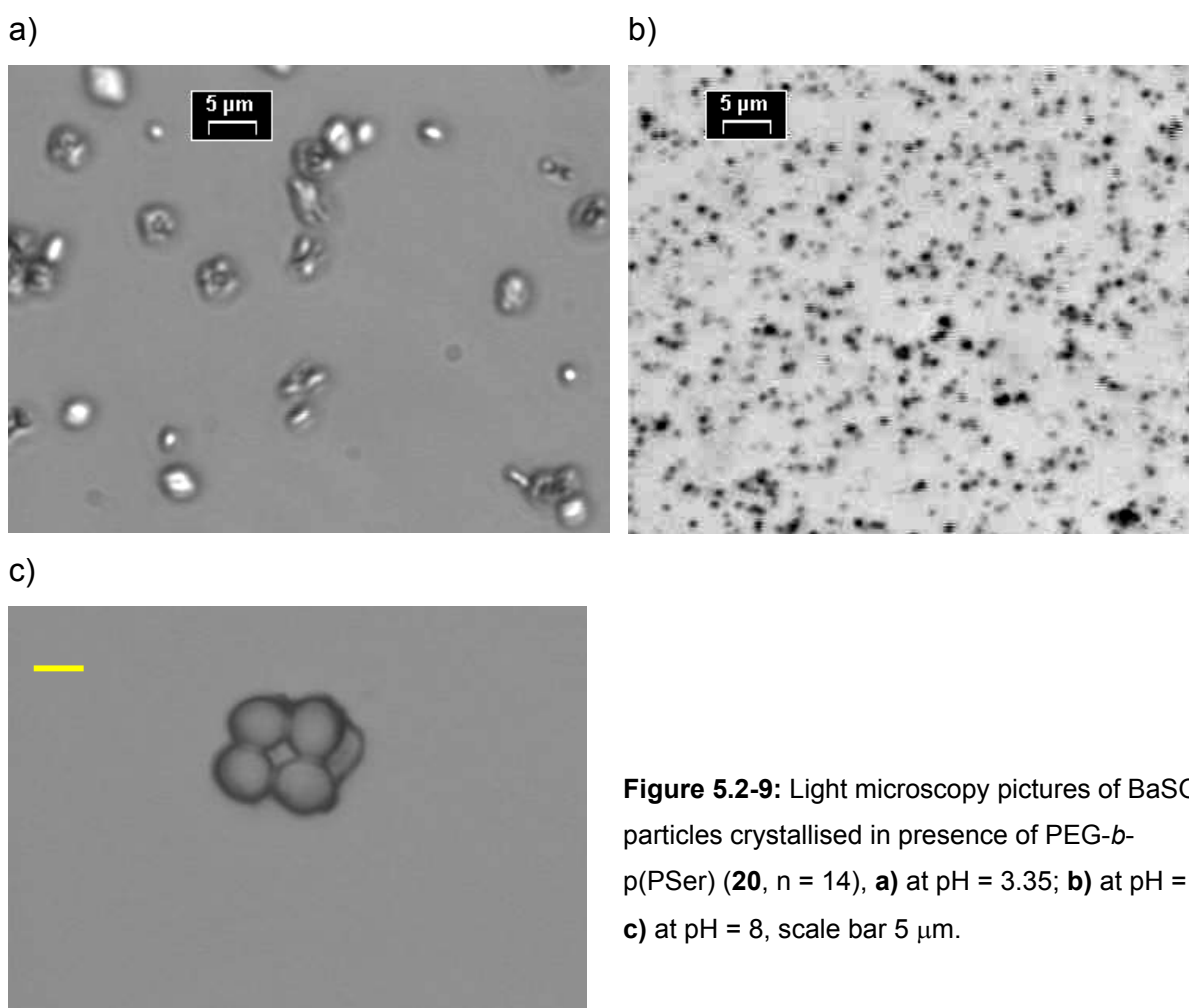
Figure 5.2-9: Light microscopy pictures of BaSO4 particles crystallised in presence of PEG-*b*-p(PSer) (**20**, n = 14), **a)** at pH = 3.35; **b)** at pH = 5; **c)** at pH = 8, scale bar 5 μm.

Figure 5.2-9 shows pictures of $BaSO_4$ particles mineralised in presence of the PEG-*b*-p(PSer) (**20**) block copolymer. The polymer was 1 g / l (10 ml solution was used) and the speed of adding Na_2SO_4 and $BaCl_2$ solutions was 55 μl/h, meaning 0.458 μmol $BaSO_4$ / min (slower speed than in previous cases). The experiments were done at 25°C.

Figure 5.2-9a shows light microscopy pictures of $BaSO_4$ particles at pH = 3.35 (pH was not adjusted, it is the pH of the polymer solution itself) with irregular shape. This corresponds to the literature [20], were the others observed a mixture of $BaSO_4$ rectangular tablets and branches in presence of PEG-*b*-PMAA block copolymer at pH = 3. At pH = 3 the phosphoserine block was close to a neutral chain (fully protonated, the pK_{a1} is at pH 2 and pK_{a2} at pH 7,3), resulting in a weak interaction between the phosphoserine block and the growing $BaSO_4$ and thus little effect on the $BaSO_4$ crystallization was found (IEP of $BaSO_4$ is at pH 3,9).

Figure 5.2-9b shows $BaSO_4$ particles in light microscopy obtained at pH = 5. The picture shows spherical particles. The same results were observed for $BaSO_4$ particles mineralised at pH = 8 (Figure 5.2-9c). The interaction between the phosphoserine block and the growing $BaSO_4$ is stronger and thus a better effect on the $BaSO_4$ crystallization was found (IEP of $BaSO_4$ is at pH 3,9).

In the literature [20] researchers observed different $BaSO_4$ particle shapes at different pH and in presence of PEG-*b*-PMAA. In case of this work at pH above 5 only spherical particles were obtained. These differences could be explained by different polymer structure. The distance of carboxyl groups in PEG-*b*-PMAA block copolymer is smaller (~ 2.5 Å) than in the polypeptide PEG-*b*-p(PSer) (**20**) (~ 4 - 9 Å) according to the calculation of the molecular conformation in vacuum with Cerius^2 software (Accelrys) (see Figure 5.2-10), and a tight pattern seems to be necessary.

a)   b)
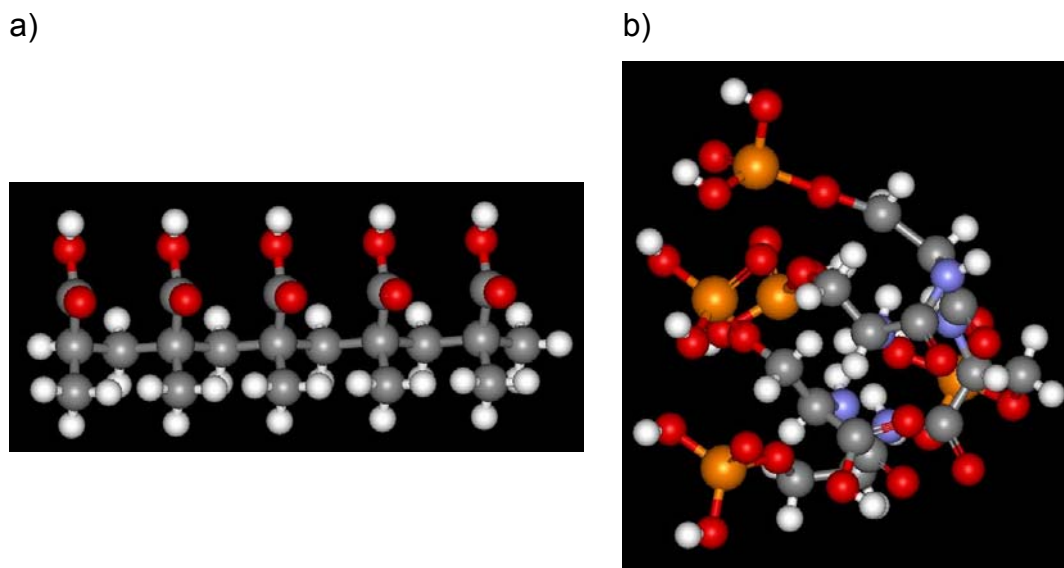
Figure 5.2-10: The molecular conformation in vacuum calculated with Cerius[2] software (Accelrys) a) pMAA block (n = 5), b) p(PSer) (n = 5).

There are differences in the morphology of $BaSO_4$ particles produced in presence of PEG-*b*-pGlu (**18c** - **g**), PEG-*b*-pAsp (**18a**, **b**) and PEG-*b*-p(PSer) (**20**) block copolymers. In case of PEG-*b*-pGlu (**18d** - **g**) at pH = 4 and at room temperature irregular shape, mostly plate-like, are obtained meaning weak polymer-crystal interaction. At the same condition, except higher temperature (T = 60 °C), the block copolymer yielded dumbbell-like particles. At pH = 8 and room temperature egg-like particles were produced due to the changes in the polymer conformation and varied strength of polymer-crystal interaction. On the other hand, in case of PEG-*b*-pAsp (**18a**, **b**) block copolymers only egg-like particles at both pHs were produced, because of the different polymer secondary structure. Thus a better effect on the mineralization due to weak binding to the crystal as compared to pGlu block under the same conditions. The block copolymer PEG-*b*-p(PSer) (**20**) yielded spherical particle at pH > 5. At pH around 3 irregular particles were produced. Here, the prepared block copolymers seem to lead to a totally different aggregation mechanism. An electric dipole field with different degrees of electric shielding of a quadrupole could explain the observed differences in the mechanism, as it was described by Cölfen [92]. In case of PEG-*b*-pGlu (**18d** - **g**) at pH = 4 and at room temperature, an α-helix (90 - 95% and 5 - 10% random coil, due to the polymer polydispersity, calculated according to the literature [98]) is formed. The carboxyl groups with identical orientation are too far from each other and cannot interact with

the mineral resulting in spherical shape. On the other hand at higher temperature where the polymer adopts a β-sheet structure (95% and 5% random coil, calculated according to the literature [98]) the carboxyl functional groups with the same orientation are close to each other (7 Å), and the polymer-crystal interaction is increased, meaning a shift of the morphology from spherical to dumbbell. The particles in presence of pAsp (**18a**, **b**) have egg-like shapes at both pH = 4 and 8, because the polymers form a mixture of random coil (80%) and an α-helix (20%, calculated according to the literature [98]), thus the polymer-crystal interaction is high enough to control the morphology of $BaSO_4$, but too weak to generate a dumbbell-like superstructure.

6   Conclusions

Proteins and peptides play a significant role in biomineralization processes, however their role is often still unexplored. On the other hand biomimetic mineralization with synthetic additives offers the unique chance of not only studying the role of the polymeric additives by model polymers but furthermore allow the possibility to create new materials in a simple waterborne process at room temperature.

The task of this work was therefore to synthesise double hydrophilic model block copolymers with peptide functional blocks namely PEG-*b*-poly(*L*-aspartic acid) (**18a**, **b**) and PEG-*b*-poly(*L*-glutamic acid) (**18c** - **g**) with different block lengths and PEG-*b*-poly(*O*-phospho-*L*-serine) (**20**) and defined polymer structure by a living polymerisation process and then to use them in a biomimetic mineralization process. A phosphoserine block is especially promising because it is known that phosphoserine is a strong inhibitor for $CaCO_3$ nucleation [81].

This work has two main parts. The first one concerns the synthesis of double hydrophilic block copolymers and their analysis. The second one is about biomimetic mineralization of $CaCO_3$ and $BaSO_4$ in presence of these block copolymers at different pH (different secondary structure of block copolymers), concentration, temperature and crystallization speed. All of these parameters were identified to be important in the mineralization process so that the role of these experimental parameters was a matter of systematic study in this work.

Polymer synthesis:

Double hydrophilic block copolymers consist of a hydrophilic block that does not interact with minerals and another hydrophilic polyelectrolyte block, which strongly interacts with mineral surfaces. These polymers were synthesised via ring opening polymerisation of *N*-carboxyanhydride (NCA), and as an initiator first hydrophilic block α-methoxy-ω-amino[poly(ethylene glycol)] PEG-NH$_2$ (**14**) (primary amine, good nucleophile) was used.

In the case of PEG-*b*-poly(*L*-aspartic acid) (**18a**, **b**) and PEG-*b*-poly(*L*-glutamic acid) (**18c** - **g**) the side functional groups were protected during polymer preparation with a benzyl ester group. The synthesis worked without any problems. The

deprotection reaction was performed by hydrogenation on Pd (on active carbon 10%) as a catalyst. ^{1}H NMR analysis showed complete success of this reaction.

In case of PEG-*b*-poly(*L*-serine) (**19**) and PEG-*b*-poly(*O*-phospho-*L*-serine) (**20**), the syntheses were done via the same route, but with difficulties. First of all there were problems with NCA syntheses and with the choice of the right protecting group. The synthesis without any protecting group gives only about 15 - 20 % yield and the solvent selection is an important consideration. The benzyl group, connected via an ether bond was identified as a possible protecting group. The reactions (NCA and polymerisation) with *O*-benzyl-*L*-serine were performed without any problems; only subsequent deprotection needed harder conditions than in the case of the aspartic and the glutamic acid analogues. An autoclave had to be used combined with a higher pressure of H_2 (30 bar) and higher temperature (55°C) resulting in 100% deprotection. Another synthetic possibility towards PEG-*b*-poly(*O*-phospho-*L*-serine) was also explored. First phosphoserine was prepared with subsequent NCA synthesis and its polymerisation. The preparation of *O*-diphenylphospho-*L*-serine hydrochloride (**17**) (starting compound for NCA syntheses) was accomplished via a four-step synthetic procedure (using phosphorylation, protection and deprotection reactions). Phosphorylation was possible with a very high yield of 98% according to ^{31}P NMR analyses. The NCA preparation and the polymerisation did not need any special conditions. The last step, deprotection, was also done by a hydrogenation reaction, and occurred with PtO_2 as a catalyst and a 100% yield was achieved.

All block copolymers were analysed by gel-permeation chromatography (GPC), IR spectroscopy and ^{1}H NMR spectroscopy. The results from ^{1}H NMR spectroscopy correspond to the macroinitiator / monomer ratio and they were used for the calculation of the peptide block molar mass. There are differences in the molar masses measured by ^{1}H NMR and GPC due to the sample column interactions resulting in a too low molar mass in GPC measurements. The GPC method was used to detect the shift in elution volumes between the macroinitiator and block copolymers and to check for other impurities (as homopolymers). All prepared polymers had quite higher polydispersity (1.1 – 1.5; from GPC), partly because of the already polydisperse macroinitiator PEG-NH$_2$ (**14**).

PEG-*b*-poly(*L*-aspartic acid) (**18a**, **b**) and PEG-*b*-poly(*L*-glutamic acid) (**18c** - **g**) in water solutions at different pH's have different secondary structures. As it was proved by CD spectroscopy PEG-*b*-poly(*L*-glutamic acid) (**18c** - **g**) at pH = 4 and at

room temperature formed an α-helix structure (90 - 95% of an α-helix and 5 - 10% of random coil, due to the polydispersity of block copolymer, calculated according to the literature [98]). With increasing pH, it transformed into a random coil (actually a mixture of an α-helix and a random coil) and at pH = 8, the block copolymer had 100% random coil structure. Another measurement was done with PEG-*b*-poly(*L*-glutamic acid) (**18e**) at pH = 4 and at T = 60 °C, its secondary structure formed instead of an α-helix (95% and 5% of random coil) a mixture of a β-sheet (95%) and a random coil structure (5%). PEG-*b*-poly(*L*-aspartic acid) (**18a**, **b**) at the same condition was identified to be a mixture of a random coil structure (80%) and an α-helix structure (20%).

Biomimetic mineralization of CaCO$_3$ and BaSO$_4$ in presence of double hydrophilic block copolymers:

The double hydrophilic block copolymer PEG-*b*-pAsp (**18 a**, **b**), PEG-*b*-pGlu (**18 c** - **g**) and PEG-*b*-p(PSer) (**20**) consisting of the binding blocks and solvating blocks were used as effective crystal growth modifiers to control the crystallisation of CaCO$_3$ and BaSO$_4$ minerals.

For CaCO$_3$ mineralization, the relative block length of the polyelectrolyte block is an important issue for the design of selectively adsorbing block copolymers. A short block of glutamic acid in case of PEG-*b*-pGlu (**18c**) did have only a weak influence on mineralization. A mixture of different particle shapes being a superstructure of calcite and vaterite nanoparticles were produced, which transformed into calcite after a short time standing in their mother solution. The block copolymers with a longer peptide chain (**18a**, **b**, **c** - **g**) showed better control of the CaCO$_3$ crystal modification and stabilised vaterite spherical nanocrystalline superstructures for more than one year. The obtained vaterite spheres were superstructures of 15 - 20 nm nanoparticles. Time dependent experiments elucidated that vaterite superstructures were formed by simple aggregation of the nanoparticles without subsequent growth within the superstructures. The amorphous precursor particles have a rather defined size, which is larger than that of the crystalline vaterite in the superstructures formed later. This implies a significant size decrease from about 50 nm to ~ 20 nm upon crystallization as a result of the higher order in crystalline structures.

The size of the final nanoparticle superstructures depended on the mineralization technique. Fast crystallisation by the *Double-Jet* technique yielded spheres 2 - 3 μm in size. On the other hand slow crystallisation by the *Kitano* method yielded spheres as well but these were about 10 μm in size as a result of the higher amount of precursor particles due to the slower precipitation. On the other hand the immediate particle nucleation at the jets in the *Double-Jet* procedure and thus the favoured kinetic control in this fast process.

Another parameter important for the mineralization process is the polymer concentration in solution. At very low concentration (0.001 g / l), only rhombohedral calcite particles were obtained indicating no polymer control of the crystallization process. With increasing concentration up to 1 g / l the block copolymer ability to control the $CaCO_3$ morphology and modification was achieved. The observation from this experiment led to the conclusion that at the polymer concentration lower than 0.05 g / l double hydrophilic block copolymers cannot properly control and stabilise the $CaCO_3$ morphology and modification anymore.

It is well known that polyphosphate-type additives have a very high potential to control mineral morphology. Therefore PEG-*b*-p(Pser) (**20**) was prepared and used in the $CaCO_3$ mineralization process. Fast crystallisation by the *Double-Jet* technique yielded dumbbell-like particles 2 - 5 mm in size. The obtained dumbbell-like particles were composed of pure 17.5 nm calcite nanoparticles and the morphology was stabilised for more than half a year, no further growth was observed.

The prepared block copolymers seem to lead to a totally different aggregation mechanism. An electric dipole field with different degrees of electric shielding of a quadrupole could explain this differences in mechanism, as it was described by Cölfen [92]. It is known that the interaction between a phospho- functional group and $CaCO_3$ crystal is strong, thus the shielding of the electric field lines is strong as well and that leads to the dumbbell formation. On the other hand the interaction between carboxylic acid and mineral are weaker, meaning lower shielding of the electric field lines and consequently sphere formation.

For $BaSO_4$ mineralization, the fast *Double-Jet* and a slow *"Precipitation"* method were also used for the preparation of $BaSO_4$ particles. The advantages of $BaSO_4$ are pH independence (does not change the pH) and only one crystal modification. The speed of precipitation was very important. To compare both

methods the $BaSO_4$ mineralization in presence of PEG-*b*-pGlu (**18d**) at pH 4 was examined. By the fast *Double-Jet* technique egg-like particles were obtained. On the other hand, the "precipitation" method yielded irregular plate-like particles.

Other important parameters are pH (different polymer secondary structure) and temperature, which is related to the polymer secondary structure. The block copolymer PEG-*b*-pGlu (**18d** - **g**) formed an α-helix (95%) at pH = 4 and room temperature, which has a turn every 3.6 monomer units meaning that a carboxyl group is found at the same orientation on the helix only every 18 monomer units. This means that for a pGlu block with n = 10, only one interacting carboxyl group is present leading to a weak interaction with the crystal resulting in spherical particles. On the other hand, the block copolymer PEG-*b*-pGlu (**18e**) at pH = 4 and at a higher temperature (60 °C) adopts a β-sheet (95%) according to the CD spectra (7 Å between two carboxyl groups which show the same orientation). This means that for the pGlu block with n = 10, 5 interacting carboxyl groups need to be considered leading to a much stronger polymer-crystal interaction compared to the α-helix. Dumbbell-like particles 2 - 3 μm in size were observed. At pH = 8 and room temperature egg-like particles were produced due to the changes in the polymer conformation and varied strength of polymer-crystal interaction. The particles in presence of pAsp (**18a**, **b**) have egg-like shapes at both pH = 4 and 8, because the polymers forms a mixture of random coil (80%) and an α-helix (20%), thus the polymer-crystal interaction is high enough to control the morphology of $BaSO_4$ but too weak to generate a dumbbell-like superstructure.

The PEG-*b*-p(PSer) block copolymer was used as well for the $BaSO_4$ mineralization process, but no different morphologies were obtained. At pH = 3.35 (pH was not adjusted, it is the pH of the polymer solution itself), irregular particles were obtained. At pH = 3 the phosphoserine block was close to a neutral chain (fully protonated, the pK_{a1} is at pH 2 and pK_{a2} at pH 7,3), resulting in a weak interaction between the phosphoserine block and the growing $BaSO_4$ and thus little effect on the $BaSO_4$ crystallization was found (IEP of $BaSO_4$ is at pH 3,9). At pH = 5 the particles have spherical shape. The same spherical shape was observed for $BaSO_4$ particles mineralised at pH = 8. The interaction between the phosphoserine block and the growing $BaSO_4$ is stronger here and thus a stronger influence on the $BaSO_4$ crystallization was found.

In this work, it could be shown that it is possible to prepare well-defined double hydrophilic block copolymers with adjustable block lengths via ring opening polymerisation. Different polymer secondary structures could be induced by pH and temperature changes. The polymer secondary structure and the different functional groups are important for mineralization processes resulting in different $BaSO_4$ morphologies (spheres and dumbbells) and two different growth mechanisms for $CaCO_3$ particles (vaterite spheres or calcite dumbbells) respectively. In the case of $CaCO_3$ the crystallization speed determines the particle size, all particles are superstructures of nanoparticles and vaterite spheres and they are stable for at least a year.

7   Acknowledgments

Many thanks go to the numerous people who contributed to this work.

8   Supplements

8.1   Abbreviations and symbols

Asp	Aspartic acid
Bzl	Benzyl-
CD	Circular dichroismus
cmc	critical micelle concentration
DMA	*N,N*-Dimethylacetamid
DMF	*N,N*-Dimethylformamid
Glu	glutamic acid
EM	Electron microscopy
GPC	Gel Permeation Chromatography
IR	Infrared spectroscopy
MALDI-TOF	Matrix Assisted Laser Desorption Time of Flight Mass Spectroscopy
m.p.	Melting point
NCA	*N*-Carboxyanhydride
NMR	Nuclear Magnetic Resonance
PEG	Poly(ethylene glycol)
Ph	Phenyl
ppm	*parts per million*
r.t.	Room Temperature
SAXS	Small Angle X-Ray Scattering
SEC	Size exclision chromatography
SEM	Scanning Electron Microscopy
Ser	Serine
TEM	Transmission Electron Microscopy
TFA	Trifluoroacetate
WAXS	Wide Angle X-Ray Scattering

8.2   Synthesis description

8.2.1 Synthesis of PEG-b-poly(aspartic acid) / poly(glutamic acid)

N-carboxyanhydride of aspartic acid 4-benzyl ester (**2a**)

A solution of bis(trichloromethyl) carbonate (2.2g; 7.2 mmol) in 60 ml THF and added to the suspension of aspartic acid 4-benzyl ester (3.5 g; 18 mmol) in 40 ml THF. The reaction mixture was stirred for 2 hours at 50 °C under argon atmosphere (the suspension became a transparent solution). Then the solvent was evaporated under reduced pressure and the obtained white oil was recrystallized three times from a mixture of THF / petrol ether and dried at room temperature in vacuum (Yield 3.38 g; 84.80 %) m. p. 126 - 127 °C (according to the literature [30 - 35]).
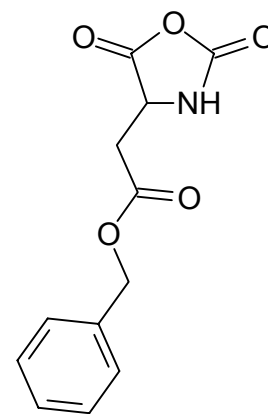
IR: 1860 cm^{-1} and 1790 cm^{-1} (C=O, cyclic anhydride)

Elemental analysis C$_{12}$H$_{11}$NO$_5$ (249.22 g/mol): Calc. 57.83% C; 4.45% H; 5.62% N; 32.10% O. Found 57.41% C; 4.33% H; 5.51% N; 32.75% O.

N-carboxyanhydride of glutamic acid 5-benzyl ester (**2b**)

A solution of bis(trichloromethyl) carbonate (2.25 g; 7.6 mmol) in 60 ml THF was added to the suspension of glutamic acid 5-benzyl ester (4.5 g; 19 mmol) in 40 ml THF. The reaction mixture was stirred for 2 hours at 50 °C under argon atmosphere (the suspension became a transparent solution). Then the solvent was evaporated under reduced pressure and the obtained white oil was recrystallized three times from a mixture of THF / petrol ether and dried at room temperature in vacuum (Yield 4.28 g; 85.88 %) m. p. 92 - 93 °C (according to the literature [30 - 35]).
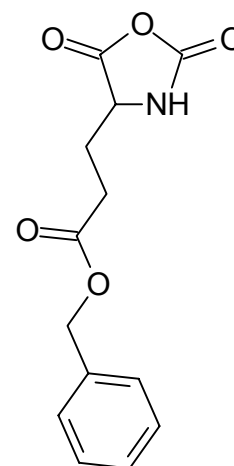
IR: 1845 cm^{-1} and 1780 cm^{-1} (C=O, cyclic anhydride)

Elemental analysis C$_{13}$H$_{13}$NO$_5$ (263.25 g/mol): Calc. 59.31% C; 4.98% H; 5.32% N; 30.39% O. Found 60.00% C; 4.46% H; 5.47% N; 30.07% O.

Poly(ethylene glycol)-*b*-poly(aspartic acid 4-benzyl ester) (**15a**)

A solution of the *N*-carboxyanhydride of aspartic acid 4-benzyl ester (2.65 g; 12 mmol) in DMF (60 ml) was added to a solution of α–methoxy-ω-amino[poly(ethylene glycol)] (5 g; 1 mmol; M$_w$ = 5000 g/mol) in DMF (80 ml). The reaction mixture was stirred over 3 days at 40 °C under a dry argon atmosphere. Then the solvent was evaporated under reduced pressure and the resulting product was dissolved in 10 – 20 ml DMF and precipitated into petrol ether (300 ml) (Yield 6,7 g).
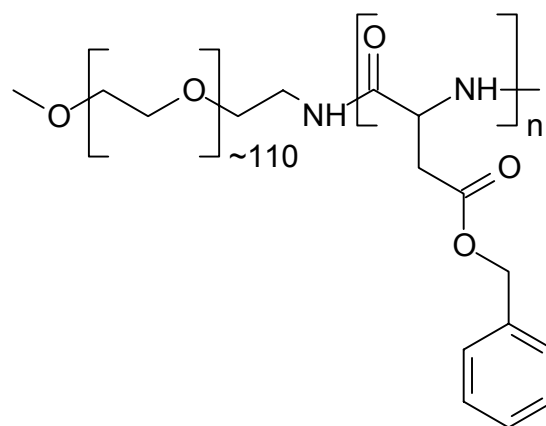
IR: 1667 cm^{-1} (Amide I, C=O) and 1542 cm^{-1} (Amide II, N–H and C-N).

^{1}H NMR (400 MHz, in DMSO-d$_8$): δ = 3.51 (s, PEG), δ = 5.08 (m, C̲H̲$_2$-Ph), δ = 7.32 (m, H-arom.).

^{13}C NMR (100 MHz, in DMSO-d$_8$): δ = 40.01 (C̲H̲$_2$-Ph), δ = 70.64 (PEG), δ = 128.00 (C-arom.).

GPC (Eluting agent DMA, PEG-calibration): Analyses of block length and polydispersity (see table 4.2-1).

Poly(ethylene glycol)-*b*-poly(aspartic acid) (**18a**)

To a solution of poly(ethylene glycol)-*b*-poly(aspartic acid 4-benzyl ester) (6.5g) in THF / methanol (1:1; 200 ml) a catalyst palladium on activated charcoal (0.7 g; 10 % Pd / C) was added. The reaction mixture was charged with hydrogen and stirred for 24 h at r.t.. Then the catalyst was removed by
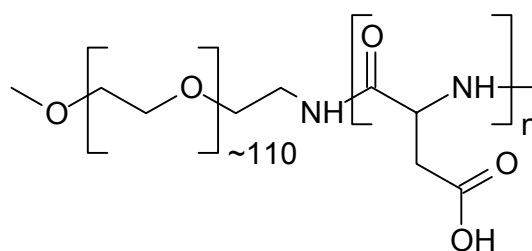
filtration and the solvent was evaporated under reduced pressure. The resulting product was dissolved in water, exhaustively dialyzed (MWCO 1000 g/mol) and subsequently freeze-dried (4.58 g).

IR: 1672 cm^{-1} (Amide I, C=O) and 1550 cm^{-1} (Amide II, N–H and C-N).

^{1}H NMR (400 MHz; D$_2$O): δ = 3.51 (s, PEG), no spinals of the benzyl group could be detected indicative of a complete removal of the protecting group.

GPC (Eluting agent acetate buffer pH = 7, PEG-calibration): Analyses of block length and polydispersity (see table 4.3-2).

Poly(ethylene glycol)-*b*-poly(glutamic acid 5-benzyl ester) (**18d**)

A solution of the *N*-carboxyanhydride of glutamic acid 5-benzyl ester (3.3 g; 12.5 mmol) in DMF (60 ml) was added to a solution of α-methoxy-ω-amino[poly(ethylene glycol)] (5 g; 1 mmol; M$_w$ = 5000 g/mol) in DMF (80 ml). The reaction mixture was stirred over 3 days at 40 °C under a dry argon atmosphere. Then the solvent was evaporated under reduced pressure and the resulting product was dissolved in 10 - 20 ml DMF and precipitated in petrol ether (300 ml) (Yield 7 g).

IR: 1655 cm^{-1} (Amide I, C=O) and 1533 cm^{-1} (Amide II, N–H and C-N).

^{1}H NMR (400 MHz, in DMSO-d$_8$): δ = 3.50 (s, PEG), δ = 5.03 (m, α-CH), δ = 7.28 (m, H-arom.).

^{13}C NMR (100 MHz, in DMSO-d$_8$): δ = 39.82 (α-CH), δ = 69.68 (PEG), δ = 127.98 (C-arom.).

GPC (Eluting agent DMA, PEG-calibration): Analyses of block length and polydispersity (see table 4.2-1).

Poly(ethylene glycol)-*b*-poly(glutamic acid) (**18d**)

To a solution of poly(ethylene oxide)-*b*-poly(glutamic acid 5-benzyl ester) (7 g) in THF / methanol (1:1; 200 ml) a catalyst palladium on activated charcoal (0.7 g; 10 % Pd / C) was added. The reaction mixture was charged with hydrogen and stirred for 24 h at r.t.. Then the catalyst was removed by filtration and the solvent was evaporated under reduced pressure. The resulting product was dissolved in water, dialyzed and subsequently freeze-dried (5.77 g).
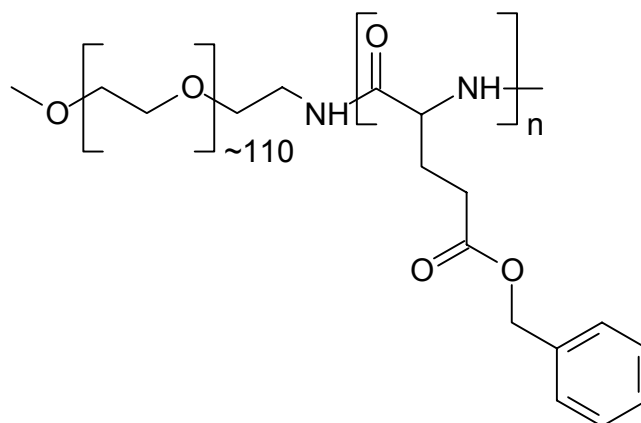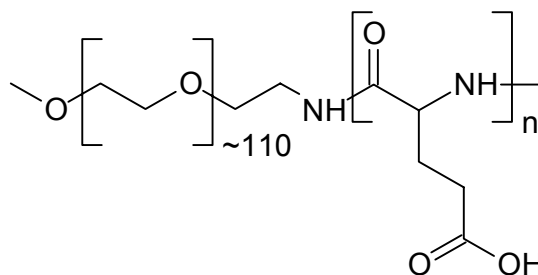
IR: 1659 cm^{-1} (Amide I, C=O) and 1541 cm^{-1} (Amide II, N–H and C-N).

^{1}H NMR (400 MHz; D$_2$O): δ = 3.51 (s, PEG), no signals of benzyl group could be detected indicative of a complete removal of the protecting group.

GPC (Eluting agent acetate buffer pH = 7, PEG-calibration): Analyses of block length and polydispersity (see table 4.3-1).

8.2.2 Syntheses of phosphoserine

$N^α$-*tert*-butoxycarbonyl-$_L$-serine 4-nitrobenzyl ester (**9**)

4-nitrobenzyl bromide (45.4 g; 210 mmol) was added to a solution of *N-tert*-butoxycarbonyl-$_L$-serine (25 g; 122 mmol) and triethylamine (29.8 ml; 214 mmol) in ethyl acetate (200 ml). The mixture was stirred over night at 90 °C. Then triethylamine hydrochloride was filtered off and the solution washed successively with 1 M HCl (2 × 100 ml), H$_2$O (100 ml), 5 % NaHCO$_3$ (2 × 100 ml) and H$_2$O (100 ml). The organic layer was dried with Na$_2$SO$_4$ and the solvent was removed under reduced pressure. An orange solid was recrystallized from ethyl acetate / pentane (Yield 38.6 g; 93 %) m. p. 102 - 103 °C (according to the literature [61]).
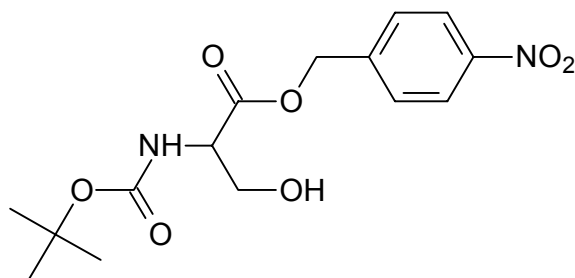
IR: 3416, 3377, 2986, 1763, 1671, 1608, 1511, 1333 cm^{-1}.

UV-VIS (in CH$_2$Cl$_2$): λ_{max} = 270 nm.

Elemental Anal. C$_{15}$H$_{20}$N$_2$O$_7$ (340.33 g/mol): Calc. 52.94 % C; 5.92 % H; 8.23 % N; 32.9 % O. Found 52.96 % C; 6.38 % H; 8.26 % N; 32.4 % O.

^{1}H NMR (400 MHz, DMSO-d$_8$): δ = 1.39 (s, 9H, 3CH$_3$), δ = 3.70 (m, 2H, CH$_2$-OH), δ = 4.18 (m, H, α-CH), δ = 4.95 (m, H, OH), δ = 5.30 (m, 2H, C̲H̲$_2$-Ph), δ = 7.02 (d, H, NH), δ = 7.64 (d, 2H, 2 Ar-H), δ = 8.21 (d, 2H, 3 Ar-H).

^{13}C NMR (100 MHz, DMSO-d$_8$): δ = 28.07 ((C̲H̲$_3$)C), δ = 56.40 (α-CH), δ = 61.24 (α-CH-C̲H̲$_2$), δ = 64.57 (C̲H̲$_2$-Ph), δ = 78.42 ((CH$_3$)C̲), δ = 123.39 (C$_{2,6}$-arom.), δ = 128.11 (C$_{3,5}$-arom.), δ = 143.88 (C$_1$-arom.), δ = 147.02 (C$_4$-arom.), δ = 155.35 (C=O-amid), δ = 170.82 (C=O-ester).

N^{α}-*tert*-Butoxycarbonyl-*O*-diphenylphospho-*L*-serine 4-nitrobenzyl ester (**10**)

A solution of diphenyl chlorophosphate (43.8 g; 163 mmol) in dry THF (150 ml) was added to a solution of N^{α}-*tert*-butoxycarbonyl-*L*-serine 4-nitrobenzyl ester (37 g; 109 mmol) in dry pyridine (100 ml) at 20 °C. The reaction mixture was stirred for 4 h at 20 °C. After that, ethyl acetate (300 ml) and 1 M HCl (100 ml) were added and the solution was stirred for a further 10 min at 20 °C. Subsequently the solution was washed with 1 M HCl (30 × 50 ml) and 5 % NaHCO$_3$ (2 × 50 ml). Then the organic phase was dried with Na$_2$SO$_4$, filtered and the solvent was evaporated under reduced pressure. White solid was crystallized from ethyl acetate / petroleum ether (Yield 57,8 g; 93 %), m. p. 115 - 116 °C (according to the literature [60]).

IR: 3280, 2982, 1748, 1700, 1521, 1485, 1341, 1280, 1199, 1166, 1062, 1035; 1014, 970, 943, 777, 691 cm^{-1}.

UV-VIS (in CH$_3$OH): λ_{max} = 263 nm.
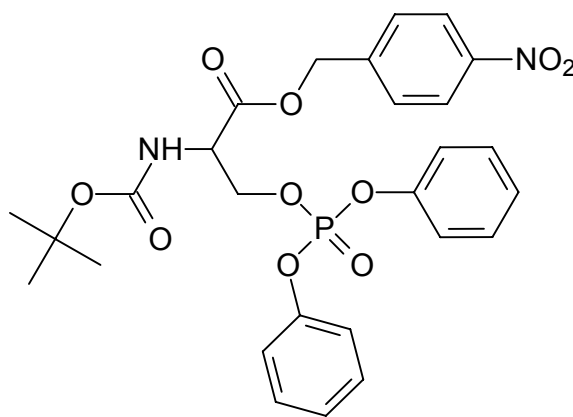
Elemental anal. $C_{27}H_{29}N_2O_{10}P$ (572.51 g/mol): Cal. C 56.64 %; H 5.11 %; N 4.89 %; O 27.95 %; P 5.41 %. Found C 56.59 %; H 5.21 %; N 4.86 %; O 27.85 %; P 5.49 %.

^{1}H NMR (400 MHz, DMSO-d$_8$): δ = 1.36 (s, 9H, 3CH$_3$), δ = 4.54 (m, 3H, α-CH + <u>CH$_2$</u>-O-P), δ = 5.28 (m, 2H, <u>CH$_2$</u>-Ph), δ = 7.23 – 7.40 (m, 10H, (O<u>Ph</u>)$_2$-PO), δ = 7.62 (d, 2H, 2 Ar-H), δ = 8.17 (d, 2H, 3 Ar-H).

^{13}C NMR (100 MHz, DMSO-d$_8$): δ = 27.99 ((<u>CH$_3$</u>)C), δ = 54.62 (α-CH), δ = 61.24 (α-CH-<u>CH$_2$</u>), δ = 67.23 (<u>CH$_2$</u>-Ph), δ = 78.80 ((CH$_3$)<u>C</u>), δ = 119.85 (C$_{2,6}$-arom., Ph-O), δ = 123.37 (C$_{3,5}$-arom., Ph-NO$_2$), δ = 125.58 (C$_4$-arom., Ph-O), δ = 128.34 (C$_{2,6}$-arom., Ph-NO$_2$), δ = 130.00 (C$_{3,5}$-arom., Ph-O), δ = 135.47 (C$_4$-arom., Ph-NO$_2$), δ = 143.33 (C$_1$-arom., Ph-NO$_2$), δ = 149.91 (C$_1$-arom., Ph-O), δ = 155.28 (C=O-amid), δ = 168.70 (C=O-ester).

^{31}P NMR (DMSO-d$_8$): δ = - 11.04.

N^α-*tert*-Butoxycarbonyl-*O*-diphenylphospho-*L*-serine (**11**)

A solution of N^α-*tert*-butoxycarbonyl-*O*-diphenylphospho-*L*-serine 4-nitrobenzyl ester (40 g; 70 mmol) in 5 % acetic acid / ethyl acetate (500 ml) containing a catalyst 10 % palladium on active charcoal (2.4 g) was charged with hydrogen and stirred over night at r.t.. Then the catalyst was removed by filtration and the solvent was evaporated under reduced pressure. The yellow oil was dissolved in diethyl ether (300 ml) and washed with 1 M HCl (2 × 50 ml) and 5 % NaHCO$_3$ (3 × 50 ml). The combined base phases were washed with diethyl ether (2 × 50 ml) acidified to pH 2 (2 M HCl) and then extracted with dichloromethane (3 × 40 ml). The combined organic phases were dried with Na$_2$SO$_4$, filtered and the solvent was evaporated under reduced pressure. White solid was crystallized from diethyl ether (Yield 18 g; 59 %), m. p. 69 - 72 °C (according to the literature [60]).
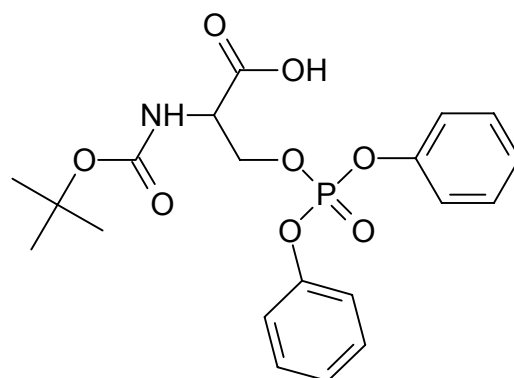
IR: 3313, 2977, 1758, 1684, 1594, 1538, 1487, 1267, 1189, 1164, 1064, 1034, 960, 785, 775, 750, 690 cm^{-1}.

UV-VIS (in CH₃OH): λ_{max} = 255 nm, 261 nm, 266 nm.

Elemental anal. C₂₀H₂₄NO₈P (437.39 g/mol): Calc. C 54.92 %; H 5.53 %; N 3.20 %; O 29.26 %; P 7.09 %. Found C 54.78 %; H 5.61 %; N 3.34 %; O 29.80 %; P 6.47 %.

¹H NMR (400 MHz, DMSO-d₈): δ = 1.36 (s, 9H, 3CH₃), δ = 4.36 – 4.45 (m, 3H, α-CH + CH₂-O-P), δ = 7.24 – 7.42 (m, 10H, (OPh)₂-PO), δ = 13.08 (s, H, COOH).

¹³C NMR (100 MHz, DMSO-d₈): δ = 28.07 ((CH₃)C), δ = 53.56 (α-CH), δ = 67.74 (α-CH-CH₂), δ = 78.48 ((CH₃)C), δ = 119.93 (C₂,₆-arom., Ph-O), δ = 125.60 (C₄-arom., Ph-O), δ = 130.04 (C₃,₅-arom., Ph-O), δ = 149.94 (C₁-arom., Ph-O), δ = 170.45 (COOH).

³¹P NMR (DMSO): δ = - 11.01.

O-diphenylphospho-ʟ-serine hydrochloride (**12**)

To a solution of N^α-*tert*-butoxycarbonyl-O-diphenylphospho-ʟ-serine (19 g; 43.4 mmol) in dry 1,4-dioxan (100 ml), a added solution of a 4 N hydrogen chloride in 1,4-dioxan (113 ml; 450 mmol) was added and stirred for 1 h at r.t.. After that the solvent was evaporated under reduced pressure. The cream-orange oil was crystallized from ethanol / diethyl ether (Yield 13.4 g; 91.4 %), m. p. 142 - 144 °C (according to the literature [60]).
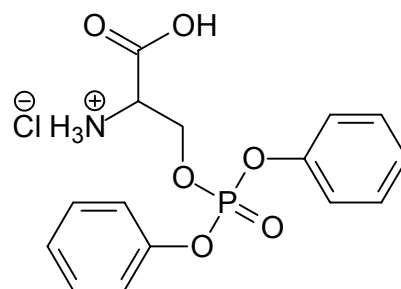
IR: 3420, 3000, 1733, 1584, 1531, 1482, 1280, 1217, 1179, 1160, 1092, 1039, 947, 943, 870, 793, 760, 687 cm⁻¹.

UV-VIS (in CH₃OH): λ_{max} = 255 nm, 260 nm, 266 nm.

Elemental anal. C₁₅H₁₆NO₆PCl (373.73 g7mol): Calc. C 48.21 %; H 4.58 %; N 3.75 %; O 25.69 %; P 8.29 %. Found C 48.00 %; H 4.42 %; N 3.68 %; O 25.63 %; P 8.20 %.

¹H NMR (400 MHz, DMSO-d₈): δ = 4.40 (m, H, α-CH), δ = 4.69 (m, 2H, CH₂-O-P), δ = 7.23 – 7.40 (m, 10H, (OPh)₂-PO), δ = 8.89 (s, 3H, COOH + NH₂).

¹³C NMR (100 MHz, DMSO-d₈): δ = 52.12 (α-CH), δ = 66.58 (α-CH-CH₂), δ = 120.01 (C₂,₆-arom.), δ = 125.75 (C₄-arom.), δ = 130.11 (C₃,₅-arom.), δ = 149.79 (C₁-arom.), δ = 168.75 (COOH).

³¹P NMR (DMSO-d₈): δ = -10.23.

8.2.3 Synthesis of PEG-b-poly(L-serine) / poly(O-phospho-L-serine)

N-carboxyanhydride of L-serine (**3**)

A solution of bis(trichloromethyl) carbonate (3 g; 28 mmol) in ethyl acetate (40 ml) was added to a suspension of L-serine (3.4 g; 12 mmol) in ethyl acetate (150 ml). The reaction mixture was stirred for 3 - 4 hours at the solvent reflux temperature under argon atmosphere. Subsequently the suspension was filtered, the solvent was evaporated under reduced pressure and the obtained white oil was recrystallized three times from ethyl acetate / petrol ether and dried at room temperature in vacuum (Yield 1.49 g; 39 %) m. p. 110 - 115 °C (according to the literature [57]).
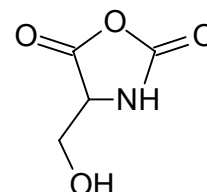
IR: 1859 cm^{-1} and 1792 cm^{-1} (C=O, cyclic anhydride)

Elemental analyses C$_{11}$H$_{11}$NO$_4$ (131.09 g/mol): Calc. 36.65 % C; 3.84 % H; 10.68 % N; 48.82 % O. Found 37.70 % C; 4.87 % H; 12.59 % N; 29.08 % O.

N-carboxyanhydride of O-benzyl-L-serine (**7**)

A solution of bis(trichloromethyl) carbonate (3 g; 10 mmol) THF (40 ml) was added to a suspension of O-benzyl-L-serine (4 g; 20 mmol) in THF (60 ml). The reaction mixture was stirred for 2 hours at 50 °C (the suspension became a transparent solution). The solvent was evaporated under reduced pressure and the obtained white oil was dissolved in dry ethyl acetate and cooled down. The chilled solution [96] was then washed with de-ionised water (20ml) chilled to 0 °C, subsequently washed with 1 % NaHCO$_3$ (20ml) chilled to 0 °C. The ethyl acetate phase was dried with Na$_2$SO$_4$, filtered and the solvent was evaporated under reduced pressure. The resulting white oil was

recrystallized three times from THF / petroleum ether and dried at room temperature in vacuum (Yield 4 g; 88.3 %) m. p. 72 - 73 °C (according to the literature [58]).
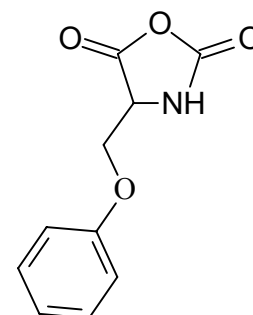
IR: 1860 cm^{-1} and 1789 cm^{-1} (C=O, cyclic anhydride)

Elemental analyses C$_{11}$H$_{11}$NO$_4$ (221.21 g/mol): Calc. 59.73 % C; 5.01 % H; 6.33 % N; 28.93 % O. Found 59.62 % C; 4.97 % H; 6.33 % N; 29.08 % O.

N-carboxyanhydride *O*-diphenylphospho-*L*-serine (**13**)

A solution of bis(trichloromethyl)carbonate (2.2 g; 7.5 mmol) in 1,4-dioxan (40 ml) was added to a suspension of *O*-diphenylphospho-*L*-serine hydrochloride (5 g; 15 mmol) in dry 1,4-dioxan (80 ml). The mixture was stirred for 2 h at 50 °C. Then the solvent was evaporated under reduced pressure. The crude product was dissolved in dry ethyl acetate (50 ml) and cooled down. The chilled solution [96] was then washed with de-lionized water (20ml) chilled to 0 °C, subsequently washed with 1 % NaHCO$_3$ (20ml) chilled to 0 °C. The ethyl acetate phase was dried with Na$_2$SO$_4$, filtered and the solvent was evaporated under reduced pressure. The resulting cream oil was crystallized from ethyl acetate / petroleum ether (Yield 4.2 g; 77.1 %), m. p. 68 - 69 °C (according to the literature [59]).
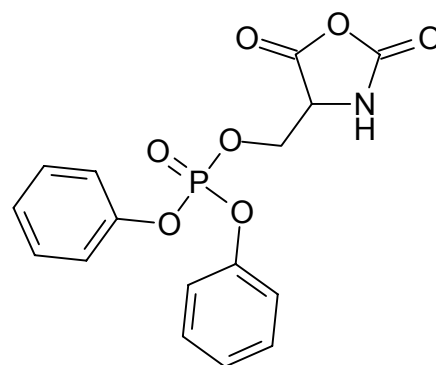
IR: 1864 cm^{-1} and 1773 cm^{-1} (C=O, cyclic anhydride).

Elemental anal. C$_{16}$H$_{14}$NO$_7$P (363.26 g/mol): Calc. C 52.90 %; H 3.88 %; N 3.86 %; O 30.83 %; P 8.53 %. Found C 52.11 %; H 3.80 %; N 3.70 %; O 30.75 %; P 8.94 %.

Poly(ethylene glycol)-*b*-poly(*L*-serine) (**19**)

A solution of *N*-carboxyanhydride of *L*-serine (0.79 g; 6 mmol) in DMF (40 ml) was added to a solution of α-methoxy-ω-amino[poly(ethylene glycol)] (3 g; 0.6 mmol;
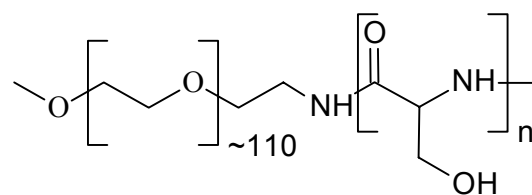
M_w = 5000 g/mol) in DMF (60 ml). The Reaction mixture was stirred over 3 days at 40 °C under a dry argon atmosphere. Then the solvent was evaporated under reduced pressure and the resulting product was dissolved in water and dialyzed (MWCO 1000 g/mol) and finally freeze-dried (1 g).

IR: 1667 cm^{-1} (Amide I, C=O) and 1542 cm^{-1} (Amide II, N–H and C-N)

^{1}H NMR (400 MHz, DMSO-d$_8$): δ = 3.51 (s, PEG), δ = 3.68 (m, CH$_2$-OH), δ = 4.19 (m, α-CH).

^{13}C NMR (100 MHz, DMSO-d$_8$): δ = 54.77 (α-CH), δ = 70.56 (PEG), 177.79 (C=O).

Poly(ethylene glycol)-*b*-poly(*O*-benzyl-*L*-serine) (**16**)

A solution of *N*-carboxyanhydride of *O*-benzyl-*L*-serine (2.89 g; 13 mmol) in DMF (40 ml) was added to a solution of α-methoxy-ω-amino[poly(ethylene glycol)] (4.36 g; 0.87 mmol; M_w = 5000 g/mol) in DMF (40 ml). The reaction mixture was stirred for 2 weeks at 40 °C under a dry argon atmosphere. Then the solvent was evaporated under reduced pressure and the resulting product was crystallized from ethyl ether (5 g).

IR: 1632 cm^{-1} (Amide I, C=O) and 1530 cm^{-1} (Amide II, N–H and C-N).

^{1}H NMR (400 MHz; DMSO-d$_8$): δ = 3.50 (s, PEG), δ = 4.4 (m, CH$_2$-Ph), δ = 7.25 (m, H-arom.)

^{13}C NMR (100 MHz, DMSO-d$_8$): δ = 54.74 (α-CH), δ = 70.64 (PEG), δ = 128.54 (C-arom.).

GPC (Eluting agent DMA, PEG-calibration): Analyses of block length and polydispersity (see table 4.2-2).

Poly(ethylene glycol)-*b*-poly(L-serine) (**19**)

To a solution of poly(ethylene glycol)-*b*-poly(*O*-benzyl-L-serine) (4.9g) in THF / methanol (1:1; 140 ml) a catalyst palladium on activated charcoal (0.5g; 10% Pd / C) was added. The reaction mixture was charged with hydrogen and stirred for 24 h in an autoclave (45 °C; 30 Bar). Then the catalyst was removed by filtration and the solvent was evaporated under reduced pressure. The resulting product was dissolved in water, filtered and freeze-dry (1.5 g).

IR: 1636 cm^{-1} (Amide I, C=O) and 1530 cm^{-1} (Amide II, N–H and C-N).

^{1}H NMR (400 MHz; DMSO-d$_8$): δ = 3.51 (s, PEG), no signal of phenyl group could be detected indicative of a complete removal of the protecting group.

GPC (Eluting agent acetate buffer pH = 7, PEG-calibration): Analyses of block length and polydispersity (see table 4.3-2).

Poly(ethylene glycol)-*b*-poly(*O*-diphenylphospho-L-serine) (**17**)

A solution of the *O*-diphenylphospho-L-serine *N*-carboxyanhydride (0.6g; 1.65 mmol) in dry 1,4-dioxan (40 ml) was added to the solution of α-methoxy-ω-amino[poly(ethylene glycol)] (0.55 g; 0.11 mmol; M$_w$ = 5000 g/mol) in 1,4-dioxan (40 ml). The mixture was stirred over two weeks at 40 °C under a dry argon atmosphere. Subsequently, the solvent was evaporated under reduced pressure. The resulting product was recrystallized from ethanol / petrol ether (Yield 0.6 g; 88%).
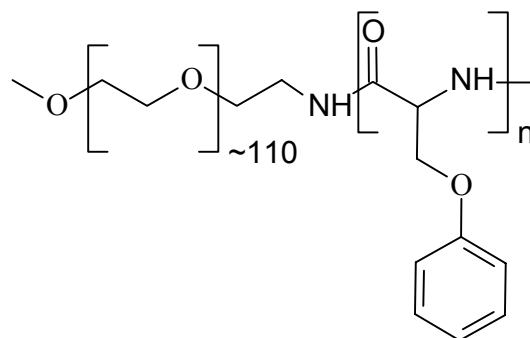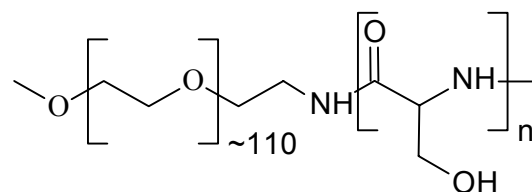
IR: 1667 cm^{-1} (Amide I, C=O) and 1542 cm^{-1} (Amide II, N–H and C-N).

^{1}H NMR (400 MHz, DMSO-d$_8$): δ = 3.51 (s, PEG), δ = 7.04 – 7.33 (m, (OPh)$_2$-PO).

^{13}C NMR (100 MHz, DMSO-d$_8$): δ = 52.12 (α-CH), δ = 66.58 (β-CH$_2$), δ = 70.68

(PEG), δ = 120.74 (C$_{2,6}$-arom.), δ = 123.60 (C$_4$-arom.), δ = 130.97 (C$_{3,5}$-arom.), δ = 153.74 (C$_1$-arom.), δ = 162.89 (C=O amid).

GPC (Eluting agent DMA, PEG-calibration): Analyses of block length and polydispersity (see table 4.2-2).

Poly(ethylene glycol)-*b*-poly(*O*-phospho-*L*-serine) (**20**)

To a solution of poly(ethylene glycol)-*b*-poly(*O*-diphenylphospho-*L*-serine) in trifluoroacetate / acetic acid (1:1; 20 ml) was added a catalyst PtO$_2$ (0.2g). The reaction mixture was charged with hydrogen and stirred for 24 h at r.t. Then the catalyst was
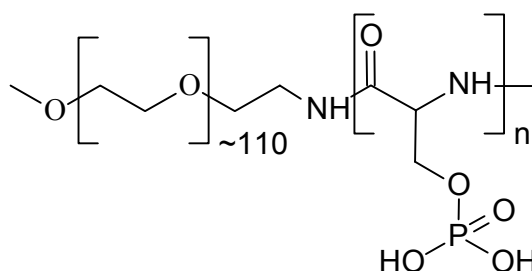
removed by filtration and the solvent was evaporated under reduced pressure. The yellow oil was dissolved in water, filtered and freeze-dried (0,32 mg).
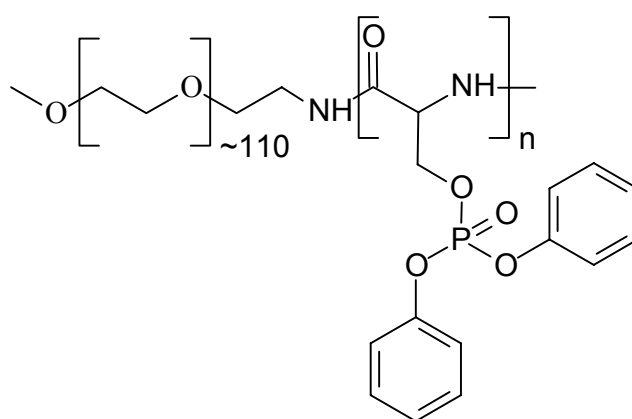
IR: 1653 cm^{-1} (Amide I, C=O) and 1535 cm^{-1} (Amide II, N–H and C-N).

^{1}H NMR (100 MHz, DMSO-d$_8$): δ = 3.51 (s, PEG), no signals of phenyl group could be detected indicative of a complete removal of the protecting group.

GPC (Eluting agent acetate buffer pH = 7, PEG-calibration): Analyses of block length and polydispersity (see table 4.3-2).

8.3   Instrumental details

Circular dichroism

Circular dichroism measurements were carried out with JASCO CD spectrometer (Model J-715) using a cylindrical quartz cell (0.1mL). Spectra were recorded at room temperature from 180-300 nm with a scanning speed of 20 nm/min A polymer solution in water was prepared with concentrations of 0.5 mg / ml or 1 mg / ml. pH was adjusted with 0.01 M NaOH and 0.01 M HCl. Peptide solutions were stirred during 24 or 72 hours, filtered through a filter 5 μm (pore size) before use and measured at 25 °C or 60 °C.

Double-Jet method

$CaCO_3$

For *Double-Jet* method is used 50 mg of polymer in 50 ml of water and the speed of adding Na_2CO_3 and $CaCl_2$ is 1,6 ml/hr, that is 1,33 10^{-2} mmol/min of $CaCO_3$ formation. A whole system is thermostated at the 25°C. And the time of adding is at least 30 min, respectively when the solution became obviously turbid or macroscopic crystal formation could be observed, than the adding is stopped (normally it takes 60 minutes). The precipitates are then left to stand in their mother solution for at least 24 hr to ensure equilibration.

$BaSO_4$

For *Double-Jet* method is used 50 mg of polymer in 50 ml of water and the speed of adding 0,5M $BaCl_2$ and 0,5M Na_2SO_4 solutions or 0,5M $Ba(OAc)_2$ and 0,5m $(NH_4)_2SO_4$ solutions is adding of 333μl/hr. A whole system is thermostated at the 25°C. The reaction is stopped when the solution became turbid or crystal formation could be observed (at least 30 minutes, normally it takes around 45-60 minutes). The precipitates were left to stand in their mother solution for at least 24 hours to ensure equilibration.

Gel permeation chromatography (GPC)

Gel permeation chromatography measurements were carried out using a Thermo Separation Products (TSP) setup with RI- (Shodex RI-71) and UV-Detector (TSP UV 1000).

1) **Eluent dimethylacetamide (DMA):** + 0.5 % w. LiBr, 70 °C, columns 4 × PSS-GRAM (300 × 8 mm; 5 μm): 30, 30, 100, 3000 Å pore size.

2) **Eluent Acetate buffer:** pH = 7; 25°C, columns 4 × HEMA-BIO (300 × 8 mm; 5 μm): 40, 100, 100, 3000 Å pore size.

Calibration: PEG and PB-Standards (PSS GmbH, Mainz).

IR-Spectroscopy

Infrared spectroscopy measurements were performed on a Nicolet, Model Impact 400 spectrophotometer. Samples were prepared as KBr pellets and measured in the 400 to 4000 cm^{-1} range.

Kitano method

$CaCO_3$

Kitano method is slow process of crystallisation of $CaCO_3$. This method takes normally 1 or 2 days until the first crystals are obtained. A supersaturated solution of $CaCO_3$ is prepared by bubbling CO_2 gas through slurry of 5 g of $CaCO_3$ in 4 l of pure water for 60 min. The $CaCO_3$ is subsequently filtered off and CO_2 is then bubbled through for another 30 min in order to dissolve the remaining $CaCO_3$ particles.

$BaSO_4$

The *"precipitation"* method is used instead of *Kitano* method. First of all, the solution of 10 mg polymer in 10 ml water is prepared and left at 25°C for some minutes. Then simultaneously 0,2 ml of 0,05M Na_2SO_4 and 0,2 ml of 0,05M $BaCl_2$ solutions are added, the solution is stirred for 1 minute and then left to stand for one day.

Light microscopy

Light microscopy was carried out using a Microscope Olympus (model BX50). Images were taken on a digital camera directly connected to the microscope.

MALDI-TOF-Mass spectroscopy

MALDI-TOF-Mass spectroscopy measurements were carried out using Kratos Compact MALDI 3 (company Shimadzu) with N_2-laser (λ=337nm). Insulin was used as a standard for detector calibration.

Samples were dissolved in water and mixed with dihydrixybenzoic acid (DHB) as Matrix and NaCl salt in ratio sample : matrix : salt 1:700:70.

NMR-Spectroscopy

All ^{1}H NMR spectra measurements were carried out at 25°C or 80°C at 400 MHz, ^{13}C at 25°C at 100 MHz and ^{31}P at 25°C at 162 MHz using a NMR-Spectrometer Bruker DPX-400. $CDCl_3$, DMSO-d$_6$ and D_2O were used as solvents. The chemical shifts of ^{1}H and ^{13}C were reported in δ relative to internal tetramethylsilame and the chemical shifts of the ^{31}P spectra were reported in δ relative to external 85% H_3PO_4.

Scanning electron microscopy (SEM)

Scanning electron microscopy measurements were carried out using Zeiss, model DSM 940A. About 1 ml of a suspension (crystals + solvent) was dropped on a sample holder, after 1-2 minutes the solvent was soaked off by filter paper and the rest was allowed to dry at room temperature.

Transmission electron microscopy (TEM)

Transmission electron microscopy imaging and electron diffraction (ED) was performed with a Zeiss, microscope model EM 912 Omega operating at 100 kV. For TEM analysis, a drop of the sample solution was placed on TEM copper grids (400 mashc) coated with thin amorphous carbon, after 1-2 minutes the solvent was soaked off by filter paper and the rest was allowed to dry at room temperature.

X-Ray diffraction; wide angle x-ray scattering (WAXS)

Powder X-ray difractograms of $CaCO_3$ samples were obtained using a Bruker wide-angle powder diffractometer model D8 operating in the Bragg configuration using Cu-K_a radiation (λ = 1.542 Å). As additional components at the primary side a 6-cm long "Göbel Mirror" with the monochromator angle of 1.28° 2θ was used as well as a "Soller slot" or "Soller diaphragm" between the sample and detector in the path of the X-rays. The intensity of X-ray reflections depending on the angle was measured by means of a scintillation counter.

9   References

1   Bruce, D.W.; O'Hare, D. *Inorganic Materials,* John Wiley &Son Ltd, Chichester, West Sussex (England).

2   Mann, S.; Weeb, J.; Williams, R.J.P. *Biomineralization: Chemical and biochemical perspectives*, VCH New York, NY (USA) 1989.

3   Mann, S.; *Chemistry & Industry*, **1995**, 93 - 96.

4   Mann,S.; *Angewante Chemie-International Edition*, **2000**, *39 (19)* 3393 - 3406.

5   Mann, S. *Nature* **1991**, *349*, 285 - 286.

6   Bianconi, P.A.; Lin, J.; Strzelecki, A.R. *Nature* **1991**, *349*, 315 - 317.

7   Mann, S. *Nature* **1988**, *332 (10)*, 119 - 124.

8   Mann, S.; *Biomimetic Materials chemistry*, VCH, Cambridge, UK, 1996.

9   Towe, K.M.; *Science*, **1973**, *179*, 1007 - 1009.

10   Lowenstam, H.A.; Abbott, D.P.; *Science*, **1975**, *188*, 363 - 365.

11   Setoguchi, H.; Okazaki, M.; Suga, S.; *Origin, Evolution and Modern Aspects of Biomineralisation in Plants and Animals*, R E Crick, Plenum Press, New York, 1989.

12   Berman, A.; Addadi, L.; Weiner, S; *Nature*, **1988**, *331*, 546 - 548.

13   Weiner, S.; *CRC Crit. Rev. Biochem.,* **1986**, *20*, 365 - 408.

14   Weiner, S.; Traub, W.; *Proc. R. Soc. London B*, **1984**, *304*, 425 - 434.

15   Mann, S.; Didymus, J.M.; Sanderson, N.P.; Aso-Samper, E.J.; Heywood, B.R.; *J. Chem. Soc. Faraday Trans.,* **1990**, *86*, 1873 -1881.

16   Walsh, D.; Mann, S.; *Nature*, **1995**, *377*, 320 - 323; Walsh, D.; Mann, S.; *Adv. Mater.*, **1997**, *9*, 658 - 662.

17   Cölfen, H.; Antonietti, M.; *Langmuir*, **1998**, *14*, 582 - 589.

18   Cölfen, H.; Qi, L.; *Chem. Eur. J.*, **2001**, *7 (1)*, 106 - 116.

19   Qi, L.; Cölfen, H.; Antonietti, M.; *Angew. Chem. Int. Ed.*, **2000**, *39 (3)*, 604 - 607.

20   Qi, L.; Cölfen, H.; Antonietti, M.; *Chem. Mater.,* **2000**, *12*, 2392 - 2403.

21   Riess, G.; Bahadur, P.; *Block Copolymers* in M.F. Mark, N.M. Bikales, C.G. Overberger, G. Menges (Eds.) *Encyclopedia of Polymer Science and Engineering*, John Wiley, New York, 1988, *vol.2*.

22   Förster, S.; Antonietti, M.; *Adv. Mater.,* **1998**, *10*, 195 - 217.

23   Cölfen, H.; *Macromol. Rapid Commun.,* **2001**, *22*, 219 - 252.

24   Kamachi, M.; Kurihara, J.K.; Stille, J.K.; *Macromolecules*, **1972**, *5*, 161 - 167.

25   a) Kricheldorf, H.R.; α-*aminoacid-N-Carboxyanhydrides and Related Heterocycles*, Springer, New York, 1987. b) Penczek, S.; *Models of biopolymers by Ring-opening Polymerization*, CRC Press, Boca Raton, Florida, 1990.

26   Leuchs, H., *Ber. Dtsch. Chem. Ges.* **1906**, *39*, 857 - 861.

27   Leuchs, H.; Manasse, W.; *Ber.Dtsch. Chem. Ges.,* **1907**, *40*, 3235 - 3249.

28   Leuchs, H.; Geiger, W.; *Ber.Dtsch. Chem. Ges.,* **1908**, *41*, 1721 - 1727.

29   Fuchs, F.; *Chem. Ber.,* **1922**, *55*, 189 - 190.

30   Brown, C.J.; Coleman, D.; Farthing, A.C.; *Nature*, **1949**, *163*, 834 - 835.

31   Farthing, A.C.; Reynolds, R.J.W.; *Nature*, **1950**, *165*, 647 - 648.

32   Farthing, A.C.; *J. Chem. Soc.*, **1950**, 3213 - 3219.

33   Coleman, D.; Farthing, A.C.; *J. Chem. Soc.*, **1951**, 3218 - 3222.

34   Coleman, D.; *J. Chem. Soc.*, **1950**, 3222 - 3229.

35   Levy, A.L.; *Nature*, **1950**, *165*, 152 - 153.

36   Dvonch, W.; Alburn, H.E.; *J. Org. chem.,* **1964**, *29*, 3719 - 3721.

37   Daly, W.H.; Poché, D.; *Tetrahedron Letters*, **1988**, *29 (46)*, 5859 - 5862.

38   Eckert, H.; Forster, B.; *Angew. Chem. Int. Ed. Eng.,* **1987**, *26*, 894 - 895.

39   Deming, T.J.; *Advanced Materials*, **1997**, *9 (4)*, 299 - 311.

40   Pasch, H.; Trathnigg, B.; *HPLC of Polymers*, Springer- Verlag, Berlin, 1998.

41   Mori, S.; Barth, H.G.; *Size Exclusion Chromatography*, Springer-Verlag, Berlin, 1999.

42   Hillenkamp, F.; Karas, M.; Beavis, R.C.; Chait, B.T.; *Anal. Chem.* **1991**, *63*, 1193 - 1201.

43   Karas, M.; Bachmann, D.; Bahr, U.; Hillenkamp, F.; *Int. J. Mass Spectrom. Ion Processes* **1987**, *78*, 53 - 68.

44   Vastola, F.J.; Pirone, A.J.; *Adv. Mass Spectrom.* **1968**, *4*, 107 - 111.

45   Koenig, J.L.; *Spectroscopy of Polymers*, Elsevier Science, New York, USA, 1999.

46   Räder, H.J.; Schrepp, W.; *Acta Polymer*, **1998** ,*49*, 272 - 293.

47   Nakanishi, K.; Berova, N.; Woody, R.W.; *Circular Dichroism: Principles and Applications*, VCH New York, USA, 1994.

9   References

48   Allen, G.; et al; *Comprehensive Polymer Science: The Synthesis, Characterization, Reactions & Applications of Polymers*; Vol.1, Pergamon Press, Oxford, England 1989.

49   Vainshtein, B.K.; et al; *Modern Crystallography 1: Fundamentals of Crystals, symmetry and methods of structural crystallography*, Springer-Verlag, Berlin, Germany, 1994.

50   Reimer, L.; *Scanning Electron Microscopy: Physics of image formation and microanalysis*, Springer-Verlag, Berlin, Germany, 1985.

51   Kitano, Y.; Park, K.; Hood, D.W.; *Journal of Geophysical Research*, **1962**, *67 (12)*, 4873 - 4877.

52   Matijevic, E.; *Current Option in Colloid Interface Science*, **1996**, *1*, 176 - 183.

53   Sedlák, M; Antonietti, M.; Cölfen, H.; *Macromol. Chem. Phys.*, **1998**, *199*, 247 - 254.

54   LaMer, V.K.; Dinegar, R.H.; *J. Am. Chem. Soc.*, **1950**, *72*, 4847 - 4853.

55   Yang, J.Z.; Antoun, S.; Ottenbrite, R.M. *J. Of Bioactive and Compatible polymers*, **1996**, *11*, 219 - 235.

56   Bohak, Z; Katchalski, E. *Biochemistry*; **1963**, *2(2)*, 228 - 237.

57   Fasman, G.D.; Blout, E.R. *J. Am. Chem. Soc*, **1960**, *82*, 2262 - 2267.

58   Lapidot, H.W.; Katchalski, E.; *Israel Journal of Chemistry*, **1968**, *6*, 147 - 150.

59   Ohkawa, K.; Saitoh, A., Yamamoto, H., *Macromol. Rapid Commun.,* **1999**, *20*, 619 - 621.

60   Alewood, P.F.; Perich, J.W.; Johns, R.B. *Synthetic Communication*; **1982**, *12(10)*, 821 - 828.

61   Perich, J.W.; Alewood, P.F.; Johns, R.B., *Aust. J. Chem.,* **1991**, *44*, 233 - 252.

62   Yokoyama, M., Inoue, S.,Kataoka, K., Yui, N. and Sakurai, Y. *Macromol. Chem. Rapid. Commun.* **1987**, *8*, 431 - 435.

63   Yokoayma, M., Miyauchi, M., Yamada, N., Okano, T., Sakurai, Y., Kataoka, K. and Inoue, S. *Canc. Res.* **1990**, *50*, 1693 - 1699.

64   Yokoyama, M., Anazawa, H., Takahashi, S., Inoue, S., Kataoka, K., Yui, N. and Sakurai, Y. *Macromol. Chem.*, **1990**, *191*, 301 - 311.

65   Yokoyama, M, Inoue, S., Kataoka, K., Yui, N., Okano, T. and Sakurai, Y. *Macromol. Chem.* **1989**, *190*, 2041 - 2055.

66   Cho, C. S., Kim, S. W. and Komoto, T. *Macromol. Chem.* **1990**, *191*, 981 - 991.

9 References

67   Cho, C. S. and Kim, S. W. *Cotrl. Release* **1988**, *7,*283 - 286.

68   Kugo, K., Ohji, A., Uno, J. And Nishino, J. *Polymer. J.* **1987**, *19*, 375 - 381.

69   Harada, A.; Kataoka, K.; *Macromolecules*, **1995**, *28*, 5295 - 5299.

70   Hruska, Z.; Riess, G.; Goddart, P.; *Polymers*, **1993**, *34 (6)*, 1333 - 1335.

71   Nah, J.-W.; Jeong, Y.-I.; Cho, Ch.-S.; *Bull. Korean. Chem. Soc.*, **1998**, *19 (9)*, 962 - 967.

72   Cammas, S.; Kataoka, K.; *Macromol. Chem. Phys.*, **1995**, *196*, 1899 - 1905.

73   Yuan, M.; Deng, X.; *European Polymer Journal*, **2001**, *37*, 1907 - 1912.

74   Bückmann, A.F.; Morr, M.; *Macromol. Chem.,* **1981**, *182*, 1379 - 1384.

75   Sedlák, M.; Cölfen, H.; *Macromol. Chem. Phys.,* **2001**, *202*, 587 - 597.

76   Yang, J.-Z.; Wang, M.; Ottenbrite, R.M.; *Journal of Bioactive and Compatible Polymers*, **1996**, *11*, 236 - 247.

77   Yokoyama, M.; Inoue, S.; *Macromol. Chem.*, **1989**, *190*, 2041 - 2054.

78   John, G.; Morita, M.; *Macromolecules*, **1999**, *32*, 1853 - 1858.

79   Rudoloff, J.; *Ph-D Thesis*; University of Potsdam, 2001.

80   Rudoloff, J.;*Diploma thesis*, Free University of Berlin, 1998.

81   Sikes, C.S.; Wheeler, A.P.; In *Surface Rective Peptides and Polymers: Discavery and Commercialization,* ACS books, Washington DC, 1991.

82   Bertnand, M.; Brack, A.; *Chem. Eur. J.,* **2000**, *6 (18)*, 3452 - 3455.

83   Higashi, N.; Nishikawa, R.; Koga, T.; Niwa, M.; *Journal of Colloid and Inteface Science*, **1999**, *220*, 362 - 366.

84   Higashi, N.; Shimizu, K.; Niwa, M.; *J. Colloid and Interface science*, **1997**, *185*, 44 - 48.

85   Harada, A.; Cammas, S.; Kataoka, K.; *Macromolecules*, **1996**, *29*, 6183 - 6188.

86   Bertrand, M.; Brack, A.; *Origins of Life and Evolution of the Biosphere*, **1997**, *27*, 585 - 595.

87   Marentette, J.M.; Norwig, J.; Stockelmann, E.; Meyer, W.H.; Wegner, G.; *Adv. Mater.,* **1997**, *9*, 647 - 651.

88   Öner, M.; Norwig, J.; Meyer, W.H.; Wegner, G.; *Chem. Mater.*, **1998**, *10 (2)*, 460 - 463.

89   Qi, L.; Ma, J.; Cheng, H.; Zhao, Z.; *J. Phys. Chem. B*, **1997**, *101*, 3460 - 3463.

90   Mastai, Y.; Rudloff, J.; Cölfen, H.; Antonietti, M.; *Chem. Phys. Chem*, **2002**, *3 (1)*, 119 - 123.

91   Mastai, Y.; Sedlák, M.; Cölfen, H.; Antonietti, M.; *Chemistry- A European Journal,* in press.

92   Cölfen, H.; *Habilitation thesis*, Potsdam University, 2001.

93   Kniep, R.; Busch, S.; *Angew. Chem. Int. Edit.,* **1996**, *35 (22)*, 2624 - 2626.

94   Busch, S.; Dolhaine, H.; DuChesne, A.; Heinz, S.; Hochrein, O.; Laeri, F.; Podebrad, O.; Vietze, U.; Weiland, T.; Kniep, R.; *Eur. J. Inorg. Chem.,* **1999**, 1643 - 1646.

95   Rudloff, J.; Antonietti, M.; Cölfen, H.; Pretula, J.; Kaluzynski, K.; Penczek, S.; *Macromol. Chem. Phys.,* **2002**, *203*, 627 - 635.

96   Poché, D.S., Moore, M.J., Bowles, J.L., *Synthetic communications,* **1999**, *29(5)*, 843 - 854.

97   Richter, A.; Petzold, D.; Hofmann, H.; Ullrich, B.; *Chem. Tech.,* **1996**, *48*, 271 - 274.

98   Greenfield, N.; Fasman, G.D.; *Biochemistry*, **1969**, *8 (10)*, 4108 – 4116.